Simulation of surface and material damage during fast ion penetration

Thesis by

John Walter Hartman

In Partial Fulfillment of the Requirements

for the Degree of

Doctor of Philosophy

California Institute of Technology

Pasadena, California

1997

(Submitted April 21, 1997)

Acknowledgements

I would like to thank those who have collaborated with me on the work within this thesis. Much of it would not have been possible without the experimental data generously shared with me by Jory Yarmoff's group at the University of California at Riverside, and Yvon Le Beyec's group at the Institut de Physique Nucleaire in Orsay.

I also cannot thank enough Mark Shapiro, who introduced me to the art of simulation, Tom Tombrello, who provided me with solid guidance and free reign, and Michelle Vine, who made the office a good place to be.

The time I have spent in Pasadena has been made memorable by the many friends I have met. I have never found a place with more people that I enjoyed so much.

I wish to thank my family for their long-distance interest in both my progress and well-being. But most of all I want to thank my wife, Amy, for making me believe that things always turn out right.

Abstract

Simulation can be a powerful tool to investigate the interaction of materials with energetic ions. In this dissertation I describe the two most common methods used to simulate ion penetration and the subsequent induced damage: the Molecular Dynamics and Binary Collision techniques. After a discussion of their limitations and realms of applicability, they are applied to a collection of interesting physical systems. The topics of investigation were chosen because simulation could provide insights into their workings which neither theoretical nor experimental methods could provide; in such cases, simulations often suggest both promising new interpretations of experimental data and better experiments that would yield a deeper understanding of the processes involved. The topics were chosen to provide a variety of examples that demonstrate the utility of such simulations. Latter chapters of this dissertation are based on articles published and projects completed during my graduate career. Abstracts of these articles are as follows:

In Chapter 3, we match the predictions of molecular-dynamics simulations of 1.2 keV and 2.0 keV $^{7}Li^{+}$ scattered from Al(100) to observed total Li atom spectra measured by time-of-flight spectroscopy. In doing so, the relevant parameters in a simple distance of closest approach model for the probability of production of single and double vacancies in the Li 1s shell during hard Li-Al collisions are determined. In the standard Fano-Lichten model of vacancy production, vacancies are produced with unit probability if the collision is hard enough to force the collision partners past some critical distance of closest approach. This assumption is insufficient to fit simulation results to experimental observations: a gradual turning-on of the vacancy production probability as the distance of closest approach decreases must be allowed. The resulting model will be useful in modeling atomic excitation effects in simulations of ion-impact processes in which inelastic losses to deep electronic orbitals are an important effect.

In Chapter 4, we present the results of simulations of cluster formation during $Ar^+ \rightarrow$ In-Ga (liquid) sputtering events. This target has a natural segregation of atomic species: the surface is almost all indium while, just a few atomic layers down, the bulk is mostly gallium. The indium concentration in small k-atom clusters (k $\leq$ 4) is found to reflect the concentration in the target at the depth from which the clusters were sputtered. We find a strong correlation between the production of clusters and the size of the events responsible for their production. A simple model for the recombination of uncorrelated emissions into small clusters is developed and found to predict accurately the production of small k-clusters during events of size N: $Y_k(N) \sim N^k$. However, this uncorrelated recombination model does not predict the proper energy spectra for clusters nor does it predict the oft experimentally observed power law decay of the yield of clusters. The means by which a model for the recombination of *correlated* emissions may more readily explain these features is discussed.

In Chapter 5, we describe a new algorithm for simulating the penetration of crystalline or amorphous matter by fast atomic clusters which can integrate intra-cluster forces properly without resorting to a full Molecular Dynamics calculation. A simple numerical model is developed which describes the desorption of hydrogen from target surfaces as fast ions or clusters penetrate the surface. Experimental observations suggest that that ions of large charge q have a desorption yield proportional to $q^{2.7}$ (although the law fails for small q), and that clusters of n ions have a desorption yield proportional to $n^{2.7}$ when the cluster is tightly correlated and proportional to n when the cluster is weakly correlated. The model describes the transition from correlated to uncorrelated desorption yields during cluster penetration and suggests the origin of both the failure of the $q^{2.7}$ law at small ion charge and the lack of charge dependence in the cluster desorption yields. Simulations of the penetration of 0.42 and 1.0 MeV/C clusters of C_{10} through thin carbon foils allow us to determine the range of the mechanism responsible for H^+ desorption. We find that the range of the mechanism responsible for H^+ desorption from a charged ion must scale as $r_{desorption} \simeq 0.5\text{Å}q^{2.7/2}$ with a lower limit on the desorption range set by the radius of the ion.

List of Publications

"The formation of clusters during large sputtering events," John W. Hartman, Mark H. Shapiro, and T.A. Tombrello, Accepted for publication in Nuclear Instruments and Methods **B** (1997).

"Dependence of inner-shell vacancy production upon distance in hard Li-Al collisions," John W. Hartman, Mark H. Shapiro, T.A. Tombrello, and J.A. Yarmoff, Physical Review **B 55**, 4811 (1997).

Contents

List of Figures

Chapter 1 Introduction

When a fast ion strikes and penetrates the surface of a material, collision processes begin the transfer of kinetic energy from the ion to the target's atoms and electrons. Intuitively, as the kinetic energy of the impacting ion increases, so does the energy transferred to the target particles. However, if the ion velocity is too large, the interaction time during a collision is too short for an effective transfer of kinetic energy.

Nuclear stopping of the ion may be understood by considering ion-target atom collisions in the Binary Collision Approximation. Neglecting all atoms in the lattice other than the nearest collision partner, one can describe the ion-atom interaction in terms of a dressed nuclear potential $V(r) = \frac{Z_1 Z_2 e^2}{r}\chi(r)$ where $\chi(r)$ describes the sheilding of the nuclear charge provided by bound electrons. The invariants of a binary collision are the center-of-mass energy ϵ and angular momentum $b\sqrt{2\mu\epsilon} = \mu r^2\dot{\theta}$, where b is the impact parameter, r the internuclear separation, θ the angle between the present and initial separatricies, and μ the reduced mass, (see figure 1.1).

From the invariants one can derive a dimensionless equation of motion:

$$1 = (\frac{b}{r^2}\frac{dr}{d\theta})^2 + (\frac{b}{r})^2 + \frac{V(r)}{\epsilon}. \tag{1.1}$$

A significant transfer of kinetic energy from the ion to its collision partner can occur only if the interaction term $V(r)/\epsilon$ becomes large at some point along the collision trajectory. Thus the effective interaction range of a fast ion can be defined by setting $V(r) \simeq \epsilon$ (see figure 1.2; in this introduction all figures have been determined assuming a ZBL potential between two silicon atoms, see reference [1]). A collision is deemed 'hard' if $V(b)/\epsilon \gg 1$ where $E = \frac{m_{ion}}{\mu}\epsilon$ is the incident energy of the ion. If this interaction range is much less than the separation of atoms in the lattice, $r \ll a \simeq n^{-1/3}$, then the BCA ansatz is validated. For typical ion-target combinations,

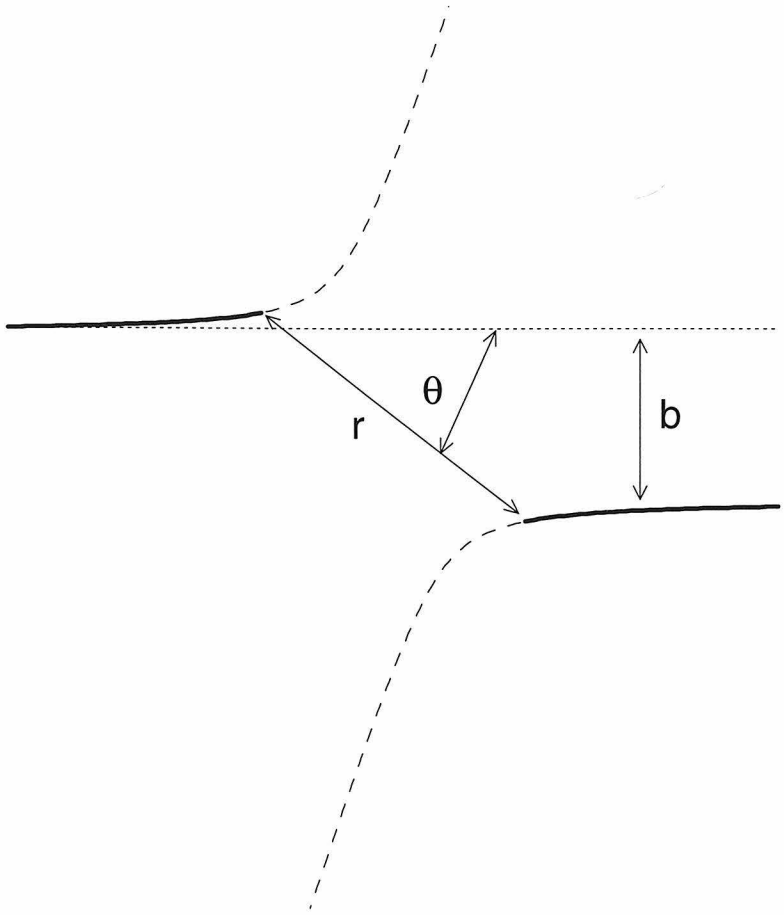

Figure 1.1: Definition of center-of-mass binary collision parameters: impact parameter b, separation r, and separatrix angle θ.

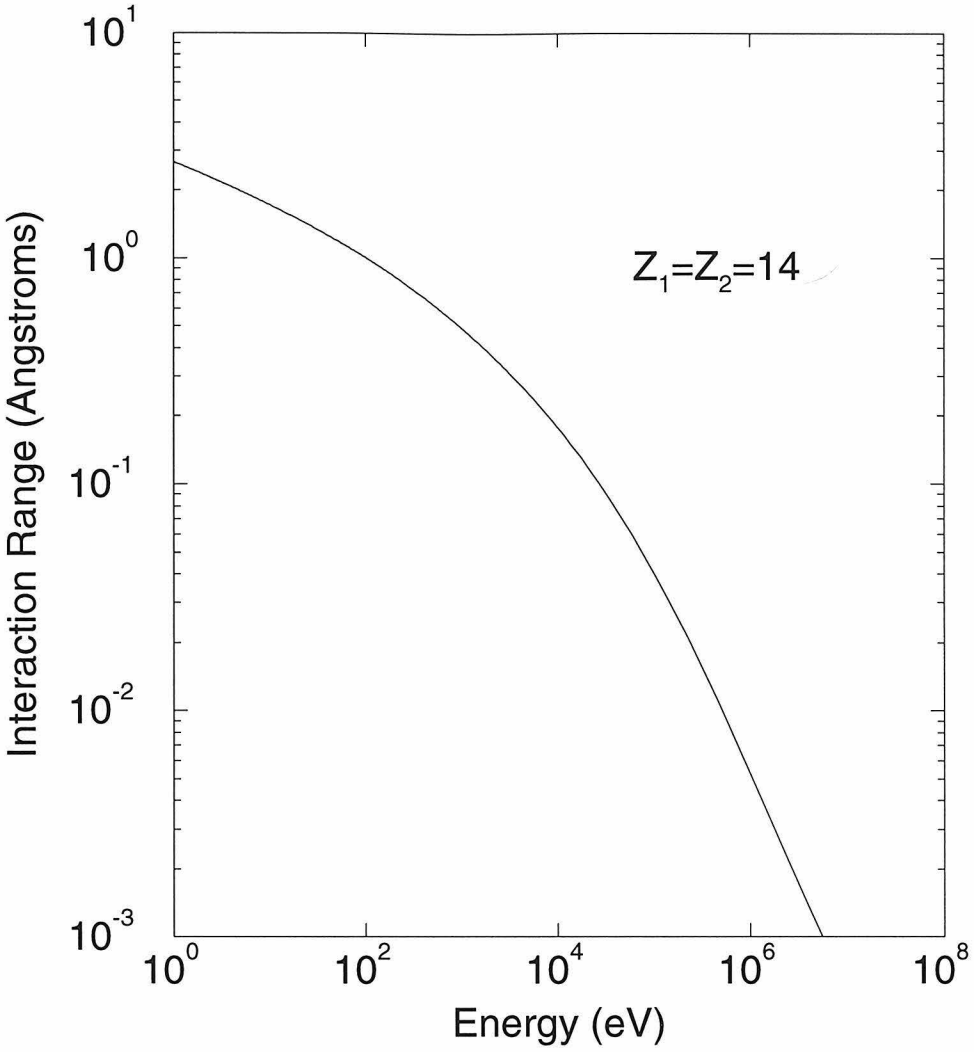

Figure 1.2: Interaction range defined by $V(r)/\epsilon \simeq 1$ for a binary Silicon-Silicon collision. For a collision between a moving ion and a stationary arom, the incident energy is related to the center-of-mass energy by $E = 2\epsilon$. For energies of less than several hundred eV, the interaction range is of order 1Å, and the ion interacts with more than one target atom at a time.

the BCA is valid for ion energies above several hundred electron Volts. Given the interaction range and density of target atoms, the penetration depth, l, of the ion into the target can be determined from $n\pi r^2 l \simeq 1$. Finally, one can estimate nuclear stopping by $\frac{dE}{dx} \sim E/l$. For typical ion-target pairs, the best transfer of kinetic energy from the ion to the target nuclei occurs for ion energies of order a few tens of keV (see figure 1.3).

The electronic stopping of fast ions in matter is still an active area of investigation; for an attempt at a unified description, see reference [1] and references therein. A brief summary of the description in reference [1] is as follows: In a conducting material, ions with velocities much less than the Bohr velocity v_0 ~22Å/fs move slowly enough that tightly bound electrons evolve more or less adiabatically about the ion-atom positions; electronic stopping is caused by the excitation of plasmons in the conduction electrons. At greater ion velocities, electrons bound to the ion may be stripped away by collisions with electrons in the bulk when the ion velocity exceeds that of the Bohr velocity of the bound orbital. Electronic stopping increases with ion velocity (and hence charge) until the velocity is of order that of its last bound K-shell electron; from the Thomas-Fermi model of electronic orbitals about a nuclear charge Z, this velocity is $v \sim Z^{2/3} v_0$ [2]. At greater velocities, the interaction time between the ion and any given target electron shrinks so that electronic stopping begins to turn off. Typically, electronic stopping reaches a maximum of $10^2 to 10^3$ eV/Å at ion velocities corresponding to several MeV.

Low energy ions (~ keV/amu) are very effective in depositing a great deal of energy in a relatively small area about their impact site. This leads to cratering of the surface and the sputtering of atoms and atomic clusters from the target. High energy ions (~ MeV/amu) penetrate deep into the material before stopping, allowing easy modification of the stoichiometry of the target while causing only minor erosion of the surface because of their relatively weak nuclear stopping. The control of these processes is a powerful tool for surface analysis and material modification [3], and fundamental knowledge of them is useful in understanding and predicting the damage suffered by surfaces and materials when placed in energetic ion environments. Because

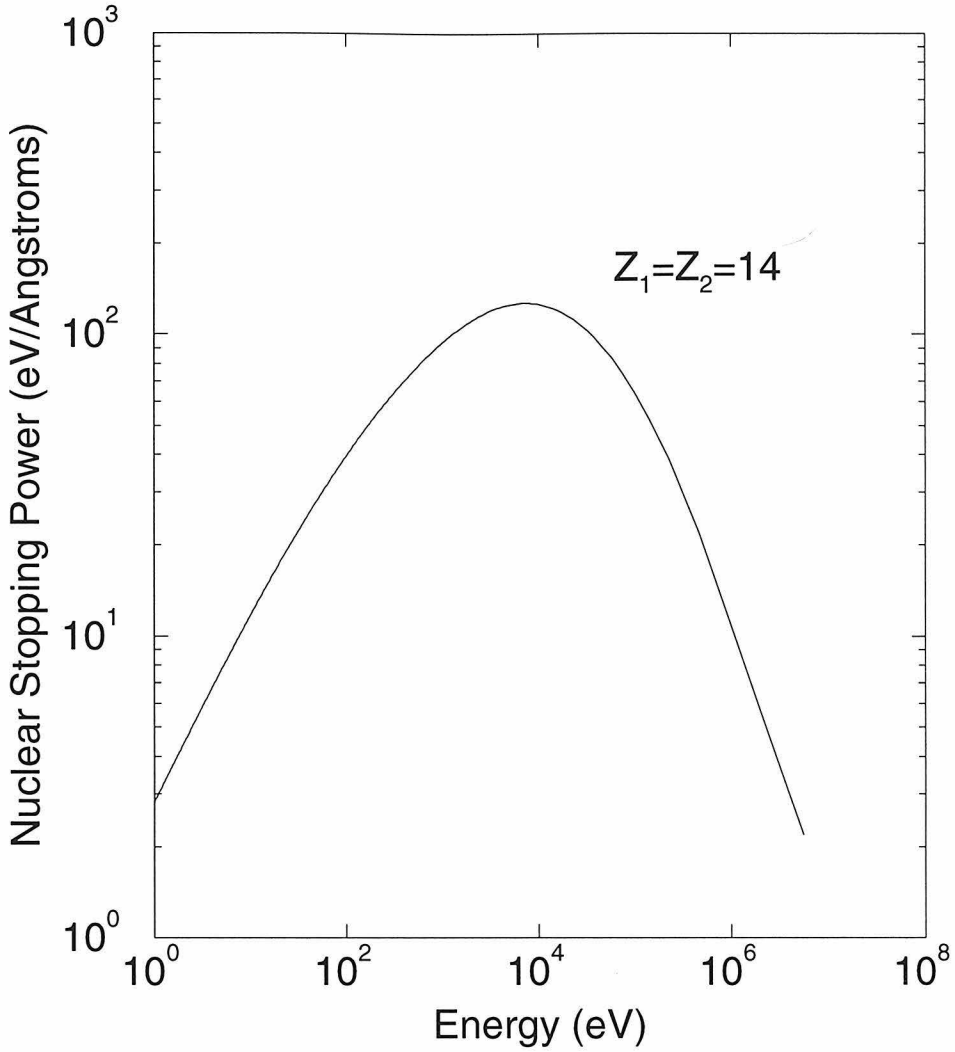

Figure 1.3: Nuclear stopping power for Silicon moving through a Silicon target estimated from $\frac{dE}{dx} \simeq En\pi r^2$, where n is the density of atoms in the target, E is the incident energy, and r is the interaction range set by $V(r) \simeq \epsilon$ (see text).

of the discrete nature of ion-atom collisions, a microscopic understanding of energy deposition and the possible ensuing target-atom collision cascade is very useful when seeking to optimize this control.

Investigation of these processes through experimental laboratory techniques is, of course, limited only by the imagination of the investigator. However, such investigations most easily measure quantities averaged over an ensemble of similar impact events; actually looking at the result of a particular impact or attempting to see the microscopic processes occurring in the targets which are ultimately responsible for the ensemble results can require extreme cleverness. On the other hand, simulations can provide easy access to the complex workings of the multiple and collective interactions occurring during any given ion impact. Further, because simulations may be interrupted and studied at any given time during their integration, taking 'measurements' requires little or no cleverness or imagination on the part of the investigator!

This dissertation presents a variety of microscopic ion-impact related effects whose investigation would not be presently possible without the use of simulation. In Chapter 2, I describe two common approaches used to simulate ion impact damage and the approximations which they implicitly assume. It is important to note that neither method attempts to integrate electronic degrees of freedom; both assume that nuclear trajectories are sufficient to characterize target damage and that electron-ion interactions are important only because they provide a continuous drag on the nuclear motion. Chapter 3 presents a mechanism for which electronic states are more important. Hard binary collisions occurring in the target may create vacancies in the inner-shells of the collision partners; while the filling of these vacancies is responsible for the Auger electron spectrum, their creation changes the effective internuclear potentials which leads to large, discrete inelastic losses which occur at the site of the collision. Models of such vacancy production generally assume the collision is truly binary, *i.e.*, that no other atoms are nearby. Because of the Fermi sea of target electrons surrounding *in situ* hard binary collisions, one expects the vacancy production mechanism to be modified. By comparison of carefully crafted experiments to simulations which include discrete inelastic losses at hard collisions, one can investigate

these vacancy producing collisions. In Chapter 4, the ejection of atomic clusters during surface sputtering is studied. While there is a plethora of proposed microscopic mechanisms describing cluster production, none successfully describe the gross features of experimentally observed cluster-emission spectra. Evaluation of simulations of individual cluster producing sputtering events can suggest refinements of these microscopic models and 'observe' new effects which have important consequences on our understanding of cluster production. In Chapter 5, a new algorithm able to simulate efficiently the penetration of fast clusters through relatively thick foil targets is developed. This algorithm is then used to predict intra-cluster spatial correlations as clusters traverse and exit the foil. Such correlations have important implications for both damage track production and surface desorption processes. Prediction of these correlations would not be possible without the use of simulation.

Chapter 2 Simulation of the ion-target impact

An assumption which greatly simplifies the simulation of the ion-target impact is that calculation of the electronic structure during the simulation is unnecessary. This assumption reduces the number of degrees of freedom in the simulation by a factor of Z_{atom} and reduces the dynamics from quantum mechanical to classical. It is justified by two facts. First, a collision between a stationary electron and moving ion can sap a maximal fractional momentum $\Delta p_{transfer}/p_{ion} = 2m_{elec}/M_{ion} \sim 1/(1836 Z_{ion})$ from the ion. Thus changes in ion trajectory by individual electron collisions are negligible; the net result of ion-electron collisions is a drag on the ion motion. Second, for ions moving slower than the Fermi velocity of the electrons in the material, electronic response to the nuclear configuration is rapid and adiabatic. This leads to an effective interaction potential which depends on only the relative positions of the atomic and ionic nuclei. Thus, the gross evolution of the target during the impact event can be predicted by integrating the motion of the nuclei under such a potential. However, because the potential is conservative, if electronic losses are important they must be included *ad hoc*; various schemes for including the electronic losses are discussed in the next chapter.

2.1 Interatomic Potentials and Electronic Degrees of Freedom

Conceptually, it is useful to imagine that one could calculate the interatomic potential through a complete Hartree-Fock calculation of the target's electronic orbitals performed in the Born-Oppenheimer approximation [4]. That is, a calculation of

self-consistent electronic orbitals and energies under the assumption of fixed atomic nuclei. Then, for a system of N nuclei and N_e electrons, the many-body potential is of the form

$$V(R_1, \ldots, R_N) = \sum_{(i,j)} \frac{Z_i Z_j}{|R_i - R_j|} + \sum_{n=1}^{N_e} \epsilon_n(R_1, \ldots, R_N). \tag{2.1}$$

The first term is the Coulomb repulsion of the nuclei; the second term is a sum of self-consistent electron energies which contain electron-nuclei attraction, electron-electron repulsion, and electron exchange. The orbitals can be separated roughly into two categories. Deep orbitals with large (and negative) $\epsilon_n(R_1, \ldots, R_N)$ are bound tightly to individual nuclei, resemble the deep orbits found in isolated atoms, and tend to shield the nuclear charge. They do not depend on nuclear position unless the relative nuclear separation is on the order of the orbital radii. Shallow orbits are greatly dependent on the relative positions of the shielded nuclei; when the solid is in equilibrium, it is the spatial structure of these orbitals that is responsible for the many-body potentials which shape all non-closepacked atomic lattices. During motion of the nuclei, so long as the electrons are fast enough to keep up with the evolution of their orbitals, the nuclear motion is conservative and governed by the equation of motion

$$M_i \frac{d^2 R_i}{dt^2} = -\nabla_{R_i} V(R_1, \ldots, R_N). \tag{2.2}$$

Electronic losses can be understood by considering non-adiabatic evolution of the orbital occupancy. If an electron is unable to follow the evolution of its orbital, then as it changes occupancy, its contribution to the interatomic potential, $\epsilon_n(R_1, \ldots, R_N)$, changes to a different function, $\epsilon_{n'}(R_1, \ldots, R_N)$. Thus the potential $V(R_1, \ldots, R_N)$ changes mid-evolution and the nuclear motion appears non-conservative. Shallow, valence-like orbitals containing relatively 'slow' electrons tend to be roughly degenerate with each other so that occupancy transfers between these orbitals can be fairly frequent. Such small, frequent losses will result in a continuous drag on the motion of the nuclei. The contribution of deep orbitals to electronic losses is more subtle. During a hard collision between two nuclei, level repulsion between deep orbitals can adiabatically push some of them up in energy until they are roughly degenerate with

more shallow orbitals. Then an occupancy transfer from a previously deep orbital to a shallow orbital is possible. If the orbital remains unfilled while the collision relaxes, then the force pushing the collision partners apart differs from that which they compressed against by $\sim \frac{d\epsilon_n}{dr}(r) < 0$. Thus, a large discrete inelastic loss of nuclear kinetic energy on the order of $\epsilon_n(r_o) - \epsilon_n(r_\infty)$ will be suffered. Here, r_o is the separation at which the occupancy transfer occurred and $\epsilon_n(r_\infty)$ is the unperturbed energy level. It is important to note that for rapidly evolving nuclear trajectories, the electrons will not be in a ground state configuration. The occupancy of electronic orbitals will change continuously and likely will exhibit a dependence on nuclear velocity and a strong hysteresis on nuclear configuration. At best, one can hope to define an average interatomic potential based on the average occupancy of the self-consistent orbitals. This, however, implies conservative nuclear motion; inclusion of losses to electronic degrees of freedom must then be included *ad hoc*.

While the above HFBO prescription for calculating the N-body interatomic potential clarifies the role of electronic orbitals in the potential, in practice it is too difficult to implement and simpler models must be used to predict interatomic forces.

For atomic lattices near equilibrium, empirical potentials can be fit to measurable constants of the material. A particularly simple example is the Morse potential [2]: a two-body potential of the form

$$V_{Morse}(r) = D\exp[-2\alpha(r - r_0)] - 2D\exp[-\alpha(r - r_0)]. \tag{2.3}$$

Given this potential and the crystal structure, one can calculate physically significant quantities such as the equilibrium lattice spacing, heat of sublimation, and compressibility. The parameters D, α, and r_0 are chosen so that these quantities match those of the material to be simulated. Once determined, the Morse potential roughly describes the interaction of atoms with near equilibrium separation. If one wishes to recover the true many body nature of interatomic potentials, a variety of generalizations can be made. For some applications, for example, the formation and sputtering of small clusters, one might require a potential which describes the change of the potential

between atoms as they leave the material. (Typically atoms in a small cluster have a different equilibrium separation and energy of cohesion than do atoms in the bulk material.) Such a potential which can describe this change is the Embedded Atom potential [5], which has the form:

$$V_{EA}(R_1, \ldots, R_N) = \sum_{(i,j)} \phi_{ij} + \sum_i F_i(\sum_j \rho_j(R_i)). \tag{2.4}$$

Here, ϕ_{ij} is a two-body potential between nuclei i and j, $\sum_j \rho_j(R_i)$ is the total density of electrons from all other atoms near the site of atom i, and $F_i(\rho_{total})$, the embedding function, describes the potential of atom i when placed in the density of electrons determined by its neighbors. For simplicity, the contribution of electron density from each atom is assumed to be spherically symmetric and independent of the relative nuclear positions. In the Embedded Atom potential, as the number of neighbors of an atom changes, so does the contribution of the embedding function to the potential. Finally, for the simulation of non-closepacked lattices, one might require a structured many-body potential which depends not only on the number of neighbors but also their relative positions. An example of such a potential is the Tersoff potential [6] which can be tuned to successfully predict both graphitic and diamond lattice structure. Formally, if the assumption of spherically symmetric electronic densities in the Embedded Atom potential form is relaxed, then structured potentials can also be written in the form of equation 2.4.

For very fast ions or for very hard collisions, many body potentials are unnecessary because the effective interaction length is short. If one were ambitious, advantage of this great simplification of the HFBO calculation could be taken. Typically, however, even simpler models of the two-body interaction are assumed. Two such models which lead to the well known Moliere and ZBL screened Coulomb potentials are based on the Thomas-Fermi statistical formulation of the atom [2, 1]. In the TF model, electrons and nuclei are assumed to live in a self consistent electric potential:

$$-\nabla^2\phi = 4\pi\rho_n - 4\pi e n_e. \tag{2.5}$$

The energy of an electron at a point in phase space is $\frac{p^2}{2m} - e\phi(r)$ and each unit volume $(2\pi\hbar)^3$ of phase space with energy less than some chemical potential $-e\phi_0$ is assumed to be occupied by 2 electrons. Thus n_e is a function of ϕ and equation 2.5 defines a self consistency problem for the potential. A great appeal of this model is the apparent universal scaling of its solutions. For example, the Moliere potential, a common approximate solution for the self consistent potential is of the form:

$$V_{Mol}(r) = \frac{Z_1 Z_2 e^2}{r}(0.35e^{-0.3r/a} + 0.55e^{-1.2r/a} + 0.10e^{-6.0r/a}), \tag{2.6}$$

where a is the scale of the screening function and given approximately by $a = 0.885a_0(Z_1^{1/2} + Z_2^{1/2})^{-2/3}$ [2]. The approximation which leads to the ZBL potential is even more extreme, but scales better [1]. The spatial distribution of electrons about each nuclei is assumed to be spherically symmetric and independent of the nuclear separation. As the nuclei press close together there are three separate contributions to the interaction potential: 1) a Coulomb potential from the distribution of nuclear and electronic charge; 2) a kinetic contribution to the electron energy caused by Pauli promotion in regions of strong electron overlap; and 3) a lowering of potential energy caused by the 'spin repulsion' of electron exchange. The ZBL 'universal' potential is

$$\begin{aligned} V_{ZBL}(r) = \frac{Z_1 Z_2 e^2}{r}(&0.1818e^{-3.2r/a_U} + 0.5099e^{-0.9423r/a_U} \\ &+0.2802e^{-0.4029r/a_U} + 0.02817e^{-0.2016r/a_U}) \end{aligned} \tag{2.7}$$

where the approximation $a_U = 0.8854a_0/(Z_1^{0.23} + Z_2^{0.23})$ is found by those authors to scale the potential between interatomic pairs best [1].

Often in simulations of $\sim$ keV impacts, one requires interatomic potentials which describe both hard-collision and near-equilibrium interactions. If a two-body potential is sufficient, then one typically applies an equilibrium potential such as the Morse at near equilibrium separations, a binary potential such as the Moliere at very small separations, and uses a numerical spline to create a smooth transition potential between these two regions. If many-body interactions are deemed important, then a

more complicated potential such as an Embedded Atom or structured potential (equation 2.4) should be used. In equation 2.4 the hard collision potential is described by ϕ_{ij} while the embedding function $F(\rho_{total})$ describes the equilibrium interactions.

2.2 Integration

There are two techniques commonly used to simulate the stopping of an ion in a material and the possible subsequent collision cascade of target atoms: Molecular Dynamics (MD) and Binary Collision (BC).

The MD approach attempts to simulate the motion of a relatively small region of the target containing a finite number N of atoms and fully integrates the classical N-body equations of motion. Because the full multi-particle interactions are considered, MD calculations can be a very useful probe of the collective atom effects occurring during an ion impact. However, because the full N-body integration is costly, it is practically restricted to targets of no larger than several thousand atoms. As such it is most readily applied in studies of shallow surface effects which include, but are not limited to, ion back-scattering, atomic sputtering, and cluster formation and sputtering.

The BC approach assumes that only two-body collisions between particles are important. This reduction in the number of interacting particles during any given collision greatly speeds the calculation and makes feasible the simulation of trajectories of fast ions penetrating deeply into the target. It has the added advantage of being commercially available in easily used (or misused) canned packages such as TRIM or MARLOWE [1, 7]. These Binary Collision integrators (which include inelastic effects due to electronic stopping) can be very useful in predicting the ion stopping due to nuclear collisions and the range of implantation of ions in a given material. However, because they ignore multi-particle collisions, they are only applicable for very fast ions whose effective interaction range is small compared to the atomic separation in the target material. For investigations of slower ion penetrations (in the keV range), a full MD integration of the equations of motion may be necessary.

2.2.1 Binary Collision Logic

A great advantage of the binary collision assumption is that the momentum transfer during a collision can be preintegrated as a function of center-of-mass energy, impact parameter, and interaction potential. Universally scaled interatomic potentials, such as the ZBL potential incorporated in the commonly known package TRIM, permit this to be done for all atomic pairs in one swipe.

In a two body collision, the invariants of the motion are the center-of-mass energy and the angular momentum:

$$\epsilon = \frac{\mu}{2}(\dot{r})^2 + \frac{l^2}{2\mu r^2} + V(r) \tag{2.8}$$

and

$$l = \mu r^2 \dot{\theta} = p \cdot b, \tag{2.9}$$

where μ is the reduced mass, r is the relative separation, p is initial momentum of the collision partners in the center-of-mass frame, and θ is the angle the separatrix of the partners makes with their initial separation vector. From these invariants, one can derive:

$$\frac{\theta}{2} = \int_{r_\circ}^{\infty} \frac{dr}{r} \frac{b/r}{\sqrt{1 - (b/r)^2 - V(r)/\epsilon}}, \tag{2.10}$$

where $r_\circ$ solves $1 = (b/r_\circ)^2 + V(r_\circ)/\epsilon$. The interaction potential is typically assumed to be of the screened Coulomb form:

$$V(r) = \frac{Z_1 Z_2 e^2}{r} \chi(r/a_\chi), \tag{2.11}$$

where Z_i are the charges of the collision partners and $\chi(r/a_\chi)$ is a universal screening function with characteristic length a_χ. Thus, equation 2.10 is a function of two variables: $Z_1 Z_2 e^2/\epsilon b$ and b/a. The momentum transfer during the collision is related to θ by:

$$\Delta p = 2p \sin \frac{\pi - \theta}{2}. \tag{2.12}$$

An approximate expression for this momentum transfer as a function of $Z_1 Z_2 e^2/\epsilon b$ and b/a has been developed by Biersack and Haggmark and can be found in reference [1].

In an amorphous material, integration of the ion trajectory is particularly simple. Between collisions the ion travels along the trajectory determined by its velocity. In a material with atomic density n, the ion should suffer a collision every time it travels a distance of $a \sim n^{-1/3}$. Because the material is amorphous, it is permissible to choose randomly the impact parameter for the collision from an appropriate distribution. The collision then provides the ion with a momentum perturbation which sends the ion off in a new direction toward its next collision. Because the impact parameter is determined probabilistically, this type of calculation is often referred to as a Monte Carlo simulation.

In a crystalline material, the impact parameters of successive collisions are found deterministically. From an initial starting position, the integrator looks forward along the ion's trajectory to determine which atom in the target will be the ion's next collision partner. The impact parameter is determined and the ion is moved forward to the site of the collision; then the appropriate momentum transfer is applied, changing the ion trajectory, and the integrator looks for the next collision partner.

In both, if atoms are struck with sufficient force to knock them out of their equilibrium position, their motion and subsequent scattering from the other lattice atoms can also be integrated with the same strategy used to handle the ion-atom collisions.

It should be noted, again, that the binary-collision integration strategy begins to fail when the energy of the moving particle is so small that the effective interaction range is large enough to include more than one collision partner. Because the applicability of BC codes is restricted to high energy collisions (much greater than many keV), electronic losses are often very important and must be included in the integration of the trajectory. The average electronic stopping dE/dx_{el} is a function of ion energy which must be measured or extrapolated from experimental observations. Electronic stopping is generally assumed only to slow the ion and not to deflect it. Typically, in a BC simulation, the ion's energy is reduced by $l \cdot dE/dx_{el}$ for each inter-

collision step length l. Because the loss for any step/collision is both probabilistic and dependent upon the electron overlap, the average stopping power is not used for each collision. Rather, one can correlate the loss to the distance of closest approach between the present binary collision, or simply randomly choose an electronic loss from a distribution about the average.

2.2.2 Molecular Dynamics Logic

The Molecular Dynamics approach integrates the full equations of motion for a system of N interacting particles:

$$\dot{r}_i(t) = v_i(t) \tag{2.13}$$

and

$$\dot{v}_i(t) = a_i(r_1(t), r_2(t), \ldots, r_N(t)), \tag{2.14}$$

where r is position, v velocity, and a the acceleration imposed upon the particle by forces due to the relative positions of the other N-1 particles. While there are a variety of possible integration schemes, MD simulations performed for this dissertation have used the following variation of the predictor corrector method. From the present state of the N-particle system $\{r_i(t), v_i(t)\}$, the algorithm predicts an approximate solution for the next state in the time series:

$$r_i^p = r_i(t) + dt \cdot v_i(t) \tag{2.15}$$

and

$$v_i^p = v_i(t) + dt \cdot a_i(r_1(t), \ldots, r_N(t)). \tag{2.16}$$

The acceleration on each of the N particles is not truly constant while they move from $r_i(t)$ to r_i^p, so in an attempt to correct for this the integrator also calculates a corrected state which averages the rates of change at the present and predicted states:

$$r_i^c = r_i(t) + \frac{1}{2} dt (v_i(t) + v_i^p) \tag{2.17}$$

and

$$v_i^c = v_i(t) + \frac{1}{2}dt(a_i(r_1(t), \ldots, r_N(t)) + a_i(r_1^p, \ldots, r_N^p)). \tag{2.18}$$

Then, comparison of the predicted and corrected states allows an evaluation of how much integration error has been introduced by the finite timestep, dt. If for any particle $|r_i^p - r_i^c|$ or $|v_i^p - v_i^c|$ is greater than some preset allowable integration error, then the attempted timestep is too large and must be reduced; after reduction of the timestep, a new predictor and corrector pair is calculated and the integration accuracy is tested. If the integration timestep is successful, *i.e.*, $|r_i^p - r_i^c|$ and $|v_i^p - v_i^c|$ are within allowable error limits, then the time counter is updated and the system is integrated forward in time by setting the new state equal to the corrector, $r_i(t+dt) = r_i^c$ and $v_i(t+dt) = v_i^c$. To speed integration a variable timestep is incorporated; if the last integration was successful, the timestep is increased slightly before the next integration step is attempted. The timestep will increase until a particularly difficult integration step is reached and then it will be cut by the integrator until the step can be accomplished while satisfying the error constraints. Difficult integration steps occur when the acceleration is changing rapidly and typically indicate that a particularly hard collision is taking someplace in the target. Higher order integration schemes also may be applied, but a recent comparative test of a variety of Molecular Dynamics integrators has not found significant differences in the predictions of these more time consuming algorithms [8].

As in BC calculations, losses to electronic degrees of freedom are not calculated *a priori* and must be included if important.

Evaluation of the accelerations of the particles in the target is a very costly procedure, and can take up to $O(N)$ processes per particle. To reduce this $O(N^2)$ cost for every timestep, a collection of cost saving ideas are implemented. Because the interaction potentials between particles are of finite range, it is useful to keep a list of neighbors for each particle in the target. Then, when each particle's acceleration is calculated from the potential and the relative positions of its neighbors, the evaluation cost is reduced from $O(N)$ to $O(n_i)$, where n_i is how many neighbors the particle

has. Of course, evaluation of the list of neighbors is itself an $O(N^2)$ process so one must optimize how long the list will be with how often the list must be updated. A second, and very useful, optimization trick is to keep a list of moving atoms; moving atoms are classified as those which have been displaced by some nominal amount from their equilibrium starting position. In this scheme, the integrator only calculates forces between atoms if one of the atoms in the neighborhood is classified as moving. This prevents the unnecessary calculation of accelerations in regions of the target which have been undisturbed by the collision cascade and therefore must be in equilibrium. One must be careful not to pump energy into the target with this method. Because forces are only calculated between moving particles, a 'non-moving' particle with a moving neighbor can be pushed into another non-mover without an appropriate charge to its kinetic energy. Energy conservation requirements force an upper limit on the critical displacement which defines a moving atom.

Successfully optimizing the combination of these and other techniques while retaining the integrity of the integration can be a very black art, and what works in one situation may not in another. Further, it is wise to take care not to spend more real time optimizing the interplay of these techniques than is gained in CPU time! However, if done properly, they can reduce the $O(N^2)$ computation time of an unoptimized MD calculation to a more manageable $O(N \ln N)$ without unacceptable sacrifices in integration accuracy.

Chapter 3 Dependence of inner-shell vacancy production upon distance in hard Li-Al collisions

3.1 Introduction

During particularly hard binary collisions, strongly bound inner-shell electronic orbitals which normally remain inert during less dramatic collision processes can be greatly perturbed. If the perturbation is strong enough, then at some critical internuclear separation, a previously deep level may be pushed up into degeneracy with a vacant orbital. If a transfer of occupancy occurs, and the vacancy does not refill while the nuclear collision relaxes, then an inelastic loss on the order of the unperturbed energy of the vacant deep orbital will be suffered by the nuclear motion.

The process causing the adiabatic evolution of a deep orbital toward a shallow one and the diabatic transfer of the electron occupancy can be understood by considering the Pauli repulsion of roughly degenerate orbitals. As the collision partners are forced together, electrons in deep orbitals bound separately to the respective nuclei are forced to occupy the same physical space. To avoid overcrowding phase space, roughly degenerate levels repel, sometimes strongly enough to push the more weakly bound orbital into degeneracy with a shallower, vacant orbital. Then the vacancy transfer may occur. A more thorough explanation of this mechanism, which considers the symmetry of the electron orbitals, is provided by the Fano-Lichten Electron-Promotion model [9] and subsequent developments [10, 11, 12].

Recent investigations by German *et al.* [13] and Weare *et al.* [14] of near 180° scattering of normally incident $^{7}Li^{+}$ ions from clean and alkali covered Al substrates provide a well controlled investigation of this ion-surface interaction. Sharp features

at the high end of the back-scattered ion energy spectrum result from $^7Li^+$ ions scattered after a single binary collision with a surface atom. Because of the large scattering angle employed, these single scattering features are well-resolved from the multiple scattering background.

German *et al.* [13] collected positive ion spectra resulting from $^7Li^+ \rightarrow$ Al (100) bombardment in the energy range of 0.4-5.0 keV. There are three peaks in each spectrum of scattered $^7Li^+$ ions which, in order of decreasing energy, they labeled P1, P2, and P3 (figure 3.1 contains similar data). The highest energy peak, P1, is attributed to elastic scattering of the $^7Li^+$ from the target to the detector after a single binary collision with an Al surface atom. The peaks P2 and P3 are similarly explained if one assumes that a discrete energy loss also occurs during the collision.

Through kinematic considerations alone, the binary-collision model (BCM) predicts that if a single ^{7}Li -^{27}Al collision is responsible for scattering a lithium atom of incident energy E_i through an angle ϕ, then the energy of the outgoing ^{7}Li atom is given by:

$$E_f = E_i\Big[\frac{\cos\phi + (\frac{27^2}{7^2} - \sin^2\phi)^{1/2}}{1+\frac{27}{7}}\Big]^2. \tag{3.1}$$

In a binary collision with a discrete inelastic loss, the final BCM energy is modified to:

$$E_f = E_i\Big[\frac{\cos\phi + [\frac{27^2}{7^2} - \sin^2\phi - (\frac{27^2}{7^2} + \frac{27}{7})\frac{Q}{E_i}]^{1/2}}{1+\frac{27}{7}}\Big]^2. \tag{3.2}$$

Note that the resultant kinetic energy loss is not the same as the promotion energy. Also acting on the $^7Li^+$ ion are continuous loss processes which decrease the energy of the scattered ions and broaden the peaks. Still, after accounting for the downward shift in each spectrum due to the continuous losses, the relative positions of P1, P2, and P3 suggest that ions making up peaks P2 and P3 have suffered discrete losses of Q2 $\simeq$ 60 eV and Q3 $\simeq$ 140 eV respectively during the Li-Al collision responsible for their scattering.

The mechanisms responsible for the 60 eV and 140 eV losses are most probably single and double vacancy transfers from the Al Fermi level to the Li 1s and Al 2p levels during hard Li-Al collisions [13]. A single vacancy production in the Li 1s

shell costs 59.1 eV, while a double vacancy production costs 142 eV[15, 16], both of which agree well with the losses required to explain P2 and P3 in the binary collision model. Alternatively, the $\sim$ 140 eV loss may be due to a two hole configuration in which the Li 1s and Al 2p levels each are left with a single vacancy for a total discrete loss of 133 eV [17, 18]. In the standard correlation diagram of the Li-Al collision complex [13], the Li 1s levels are pushed up into the Al valence band suggesting that at close separation the Li $1s^0$ configuration vacancy costs less than the Li $1s^1$ Al $2p^5$ configuration. However, at large Li-Al separation, the Li $1s^0$ configuration costs 142 eV compared to the smaller 133 eV cost of the Li $1s^1$ Al $2p^5$ configuration. Hence a crossing must occur during the separation phase of the collision; this makes either configuration possible. In fact, the latter configuration is probably more likely because it represents a better equi-partition of energy between the Li and Al collision partners.

We have performed molecular-dynamics (MD) simulations of the scattering of $^7Li^+$ ions from clean Al (100) surfaces. For the purpose of this investigation, we modified the MD code SPUT2 [19] to permit inelastic losses of Q2 = 59.1 eV and Q3 = 142 eV during hard Li-Al collisions. Collisions are deemed 'hard' when the distance of closest approach (DCA) of the collision partners is less than some critical separation. It is important to note that MD calculations do not track the charge state of the individual atoms. As such, they predict a spectrum which includes all scattered atoms regardless of charge state.

While there is a wealth of experimentally observed positive ion spectra [13], extraction of a positive ion spectrum from MD data requires the successful integration of several effects. The probability of vacancy production during hard collisions must first be adequately described, and then, the resonant neutralization of positive ions, and autoionization of excited neutrals leaving the surface must be taken into account. For Li^+ scattered elastically from clean Al, the fraction reaching the detector without suffering neutralization is qualitatively understood: the probability that the unexcited Li escapes without neutralization decreases exponentially with the time it spends near the surface [20] (for a more detailed model applied to alkali systems, see

reference [21]). For inelastically scattered Li the situation is less clear. Auger and autoionization processes may fill the vacancies present in the excited Li during the time the Li is leaving the surface. When the occupation of the inner-shell changes, so does the equilibrium charge state of the Li atom above the Al surface. At present we do not have a model which unambiguously convolves these processes.

We can, however, avoid the problems inherent in modeling positive ion spectra by considering total Li spectra measured by time-of-flight (TOF) spectroscopy [14]. Given the TOF spectra, as shown in figure 3.1, the only effect we must model to match simulation to experimental data is the probability of vacancy production during hard Li-Al collisions.

The typical model of atomic excitation in MD calculations calls for excitation when the DCA between collision partners is less than some critical radius. In the standard Fano-Lichten model [9], Fermi pressure ejects electrons when two roughly degenerate orbitals are forced close together. The critical collision partner separation at which this occurs is taken to be the sum of the maximal-charge radii of the two orbitals. In Li-Al collisions the Al 2p electrons, bound with 73eV, knock out the Li 1s electrons, bound with 59eV. The critical DCA is on the order of $r_{Al2p} + r_{Li1s} \simeq 0.43$Å[17].

By increasing the energy of the incident $^7Li^+$ ion, we can decrease the Li's distance of closest approach to the primary surface Al from which it is scattered. Figure 3.2 shows that (in the simulation) the distributions of DCAs are narrowly peaked. Thus the Fano-Lichten model would suggest that below a certain incident energy, no promotion would occur, while above it, all of the ions would be promoted. Since the experimental data strongly suggests that this is not the case, the model must be modified. We find that a gradual turning-on of the vacancy production probability as the distance of closest approach decreases is required to fit our simulations to experimental observations.

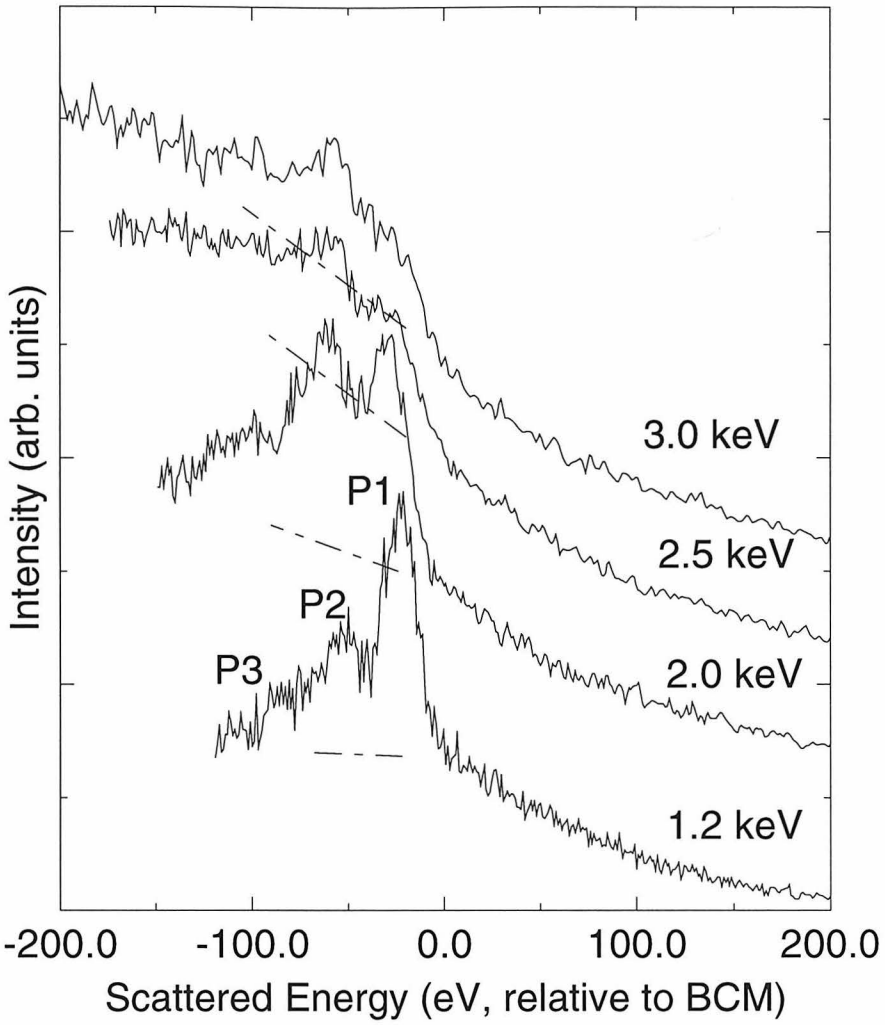

Figure 3.1: Experimental time-of-flight spectra counting the total yield of Li scattered from Al (100) and detected 12° from normal along the [110] direction. Detector size was ±2°. Also indicated are our assumptions of what contribution the background of ions scattered from deeper in the target is made to each observed spectrum.

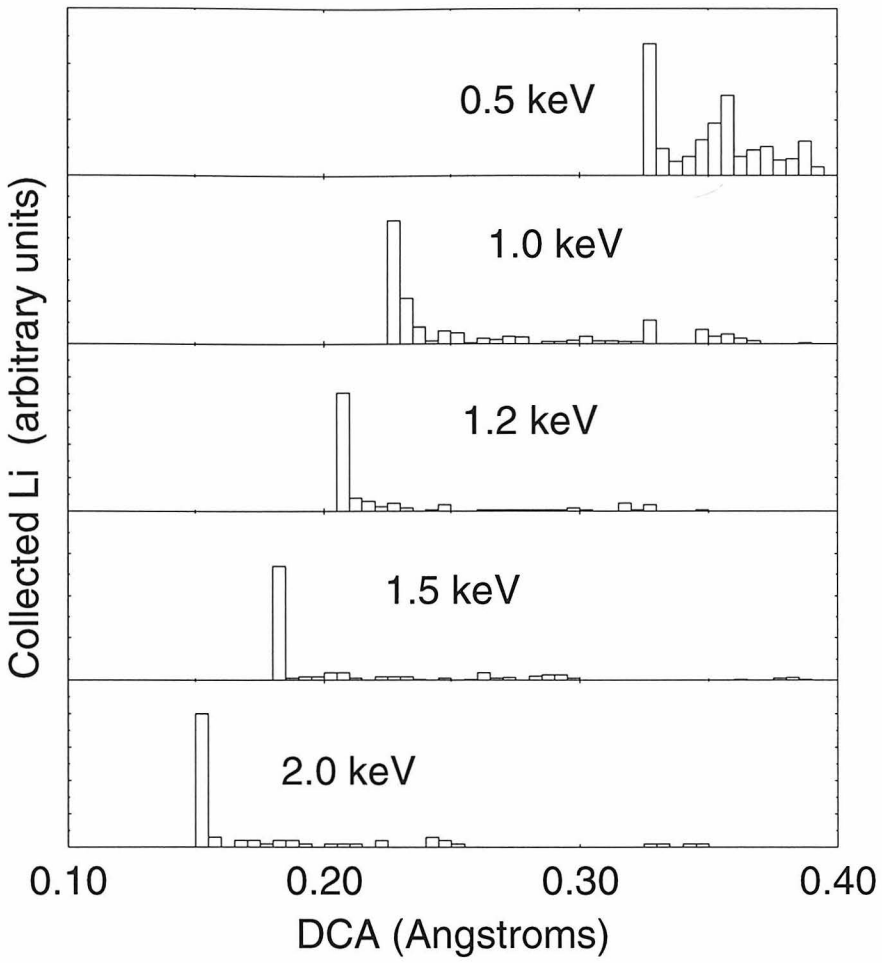

Figure 3.2: Distribution of DCAs for scattering into a $\pm 10°$ detector placed 12 deg from normal along the [110] axis of the Al (100) surface. Results of previous, unpublished simulations of 0.5, 1.0, and 1.5 keV are included with the presently discussed 1.2 and 2.0 keV simulations. Note the sharp peaking of the higher energy distributions about a single value of the DCA.

3.2 Molecular Dynamics Model and Procedure

Because the interesting features in the $^7Li^+$ spectra are due to single scattering events, our simulation targets were kept relatively small. This was necessary to keep our computation time reasonable. Unfortunately, small targets do not provide deep scattering centers responsible for the broad background signal underneath the features we wish to model. To correct for this inadequacy we are forced to assume and subtract a smooth background of multiply-scattered atoms from the TOF spectra before fitting them to the simulated spectra. The minimal energy requirements for the TOF detector restrict the energy of the incident Li ion to be above 1.2 keV. Also, at high incident energies (greater than about 2.0 keV), the continuous losses so broaden the features that they are difficult to discern from each other. Still, we can gain valuable insight as to the nature of vacancy production in ion-surface collisions by studying this system in the range of available energies.

Our model target was prepared as a face-centered-cubic lattice of ^{27}Al with its (100) surface normal to the incident $^7Li^+$ ion. There were 5 atomic layers in the target with 49 atoms in each layer.

All interactions were of the two-body type and derived from Moliere, $V(r) = (A/r)[0.35\exp(-0.3r/a)+0.55\exp(-1.2r/a)+0.10\exp(-6.0r/a)]$, and Morse, $V(r) = D\{\exp[-(r-r_{eq.})/b]-1\}^2$, potentials [2]. The $^7Li^+$ -^{27}Al interaction was Moliere (A=561.561eVÅ, a=0.1533Å) for all ion-atom separations. The ^{27}Al-^{27}Al interaction was assumed to be Moliere (A=1946.64eVÅ, a=0.12547Å) for r< 1.0Å, and Morse (D=0.456eV, $r_{eq.}$=2.953Å, b=0.8842Å) for r> 1.697Å. The Moliere coefficient A is 0.8 times the standard theoretical value $Z_1\ Z_2\ e^2$ which permits a smoother spline between the two regions. A cubic spline, $V(r) = C_0+C_1r+C_2r^2+C_3r^3$, ($C_0$=662.336eV, C_1=-1107.160eV/Å, C_2=626.970eV/Å^2, C_3=-119.705eV/Å^3) was interpolated between the Moliere and Morse regions.

All events began with the incident $^7Li^+$ ion 3 Å above the target surface and each was integrated for 50 femtoseconds. We simulated the bombardment of the targets with normally incident $^7Li^+$ ions of 1.2 keV and 2.0 keV. After a coarse scan of

impact parameters in the central unit cell on the surface, we determined that only those impacts within 0.42 Å and 0.32 Å of the surface and subsurface aluminum atoms, respectively, were scattered back from the target. This permitted us to do a much finer scan of impacts while neglecting those regions which did not contribute to the scattered $^7Li^+$ spectrum. No attempt was made to model the effects of thermal vibrations in the lattice. At zero temperature, and for normally incident ions, the number of events to be run can be further reduced by a factor of eight by taking advantage of the symmetry of the square unit cell of the target surface. However, when using this symmetry to reduce the number of impacts run, care must be taken to count properly the ions scattered into a detector placed at an angle to the surface normal. We ran, in the central unit cell, an evenly spaced grid of impact parameters of what amounted to 1300x1300 and 1600x1600 impacts for the 1.2 keV and 2.0 keV incident $^7Li^+$ ions. However, by rejecting those impacts too far from the surface or subsurface atoms to be backscattered, and by taking advantage of the surface symmetry, we were able to reduce the number of runs in each case to between 20,000 and 30,000. For each impact parameter, the final position and velocity of the Li atom were saved so that its contribution to the spectrum of lithium atom energies seen at the detector could be determined.

A molecular dynamics simulation in which the force between particles depends only on the particles' relative positions is necessarily conservative. The inclusion of discrete inelastic processes in the simulation, such as the loss due to K-shell vacancy production in Li during hard Li-Al collisions, must be handled carefully. To accomplish this we use a 'step-out' procedure to remove energy from binary collisions determined to be inelastic [19]. When the Li and Al inelastic collision partners pass their distance of closest approach, a nonconservative integration step is taken by the integrator which moves them away from each other by a distance sufficient to decrease their relative potential energy by the amount of the discrete inelastic loss. Since the Li-Al potential is quite steep near all distances of closest approach in collisions deemed inelastic, the displacement is small. In this procedure velocities of the partners are unchanged and the step-out is taken in a manner which retains their relative center

of mass.

This procedure is simple and is relatively easy to introduce into an elastic molecular dynamics code. It treats each quasi-binary collision as an interaction black box: two particles enter, two particles exit and the kinematics of the inelastic collision are satisfied. In this sense the dynamics are to be as trusted as any output from a reasonable molecular dynamics calculation — good for statistics, not good for individual trajectories. This procedure is certain to fail in cascades with high spatial density where the step-out results in a significant change in the potential energy between a binary collision partner and some other nearby atom. In this case kinematics will not be satisfied. In the present simulations the densities are always low enough that this is not a problem.

The objective of the simulation is to find the probabilities of single and double vacancy production as a function of DCA during hard Li-Al collisions. We have already noted (see the introduction) that even during a very hard collision, in which the Li-Al collision partners are forced closer together than the standard Fano-Lichten radius, a vacancy is not produced with unit probability. Having the integration routine generate a random variable, calculate the probability p_* and p_{**} for single and double vacancy production, and then perform (or not perform) the step-out procedure after comparison of p_* and p_{**} to the random variable would be an extremely inefficient method to compile statistics. First, many runs of every impact parameter which led to a possible inelastic loss would be required. Second, all of those runs would have to be repeated if new rules for p_* and p_{**} were to be tested. To avoid this, we chose to make three parallel runs of each impact position. The first run allowed only elastic collisions; the step-out was never performed. Respectively, the second and third runs performed step-out procedures corresponding to 59.1 eV and 142 eV losses for the first Li-Al binary collision with a DCA < 0.44 Å. In addition to the final position and velocity, for all Li suffering an inelastic loss, the DCA to the exciting Al atom was also saved. The trajectories and DCA's for all three possible vacancy production outcomes for each impact position can then be combined to allow us to predict the TOF spectra given a variety of models for the probabilities of vacancy production.

3.3 Results

The experimental data shown in figure3.1 were taken with the detector placed 12° from normal along the [100] direction of the Al (100) surface. The detector acceptance was ±2°; further details of the experiment are described in reference [21]. In the simulation all Li atoms with velocities directed into the cone of angle δ about the same detector position were collected. To improve statistics in the simulation, we chose a larger detector size of $\delta = \pm 10°$.

The simulated spectra of lithium atoms scattered elastically and inelastically in the three types of runs described above are shown in figure 3.3. In the simulation, the probabilities for single and double vacancy production and the spectra of elastically and inelastically scattered Li determine the spectrum of Li atoms seen at the detector. To derive the spectrum which is predicted for a particular choice of the probabilities of single and double vacancy productions, p_* and p_{**}, the following procedure is followed. For each impact position:

1) If the Li could have suffered an inelastic loss (*i.e.*, if the DCA to any Al atom was less than 0.44 Å), then:

a) The Li atom from the run which did not permit inelastic losses is checked to see if it is caught by the detector. If so, the weight $p_0 \equiv 1 - p_*(DCA) - p_{**}(DCA)$ is added to the appropriate energy bin.

b) The Li atom from the run which enforced a 59.1 eV loss for all DCA < 0.44 Å is checked to see if it is caught by the detector. If so, the weight $p_*(DCA)$ is added to the appropriate energy bin.

c) The Li atom from the run which enforced a 142 eV loss for all DCA < 0.44 Å is checked to see if it is caught by the detector. If so, the weight $p_{**}(DCA)$ is added to the appropriate energy bin.

2) If the Li could not have suffered an inelastic loss (*i.e.*, if the DCA to no Al atom was less than 0.44 Å), then the results of all three runs are the same and the weight 1 is added to the appropriate energy bin.

To fit the simulation (performed with thin targets) to the experimental data, we

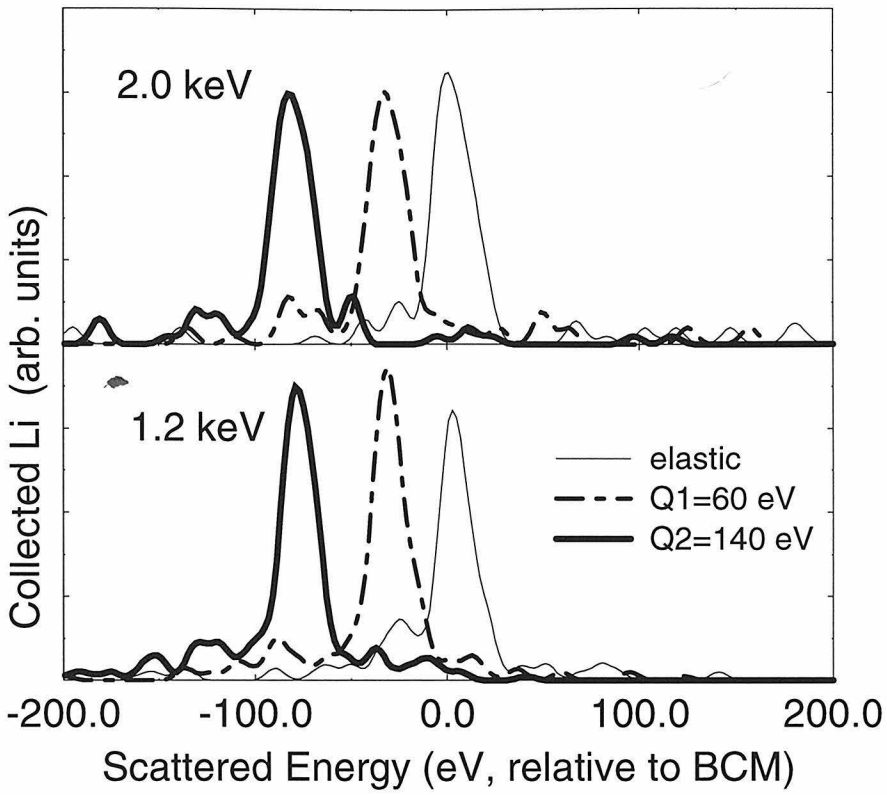

Figure 3.3: Spectra of scattered Li atoms from simulations permitting inelastic losses of 0 eV, 59.1 eV, and 142 eV during the first Li-Al collision with a distance of closest approach of less than 0.44 Å. In each case the spectrum of atoms was collected by an imaginary detector placed 12° from normal along the [100] direction of the target; detector acceptance was ±10°. The spectra have been smoothed by convolving a 5 eV wide Gaussian with the energy of each collected Li atom. Note that the weight of the scattering peak is roughly unchanged even though the energy of the peak maximum decreases with increasing inelastic loss.

must estimate the contribution of deeply scattered ions to each experimental spectrum and remove it. We assume that any sharp or sudden changes in the experimental spectra are due to the three single scattering peaks of interest, and also, that the peaks ride on the (presumably) smooth background we wish to subtract. In figure 3.1 we have indicated the background we have removed before fitting simulation to experiment. The 1.2 keV and 2.0 keV TOF spectra have the sharpest distinction between binary collision features and the deep scattering background (see figure 3.1). Because of this, we have only attempted to simulate these two spectra.

We can now determine p_* and p_{**} as a function of DCA. During the simulation, the distance of closest approach of each Li to its primary Al hard-collision partner (the Al responsible for scattering it back to the detector) was recorded. In figure 3.2 we show the distribution of primary DCAs of trajectories that result in successful scattering into the detector. (During a previous, unpublished investigation we performed simulations of 0.5 keV, 1.0 keV, and 1.5 keV $Li^+ \rightarrow$ Al (100).) For incident energies greater than or on the order of 1.0 keV with trajectories resulting in detection, we find the distributions of DCAs to be narrowly peaked. For the 1.2 keV Li atoms scattered to the detector, the peak is centered on 0.20 Å, while for the 2.0 keV Li atoms, the peak is centered on 0.15 Å. Further, note in figure 3.3 that the effect of a discrete inelastic loss is merely a shift downward in energy of the entire peak; the weight of the peak is not appreciably changed. Given these two observations, the weights of the experimental peaks (after background subtraction) will be roughly in the ratio W1:W2:W3$\simeq p_0(DCA) : p_*(DCA) : p_{**}(DCA)$.

After subtracting a smooth background from the experimental spectra (see figures 3.1 and 3.4), and using the DCA for the given incident energies found from the simulations, we see from the 2.0 keV TOF spectrum that for DCA$\simeq$ 0.15 Å, $p_0 : p_* : p_{**} \simeq$0.48:0.38:0.14, while from the 1.2 keV TOF spectrum that for DCA$\simeq$ 0.20 Å, $p_0 : p_* : p_{**} \simeq$ 0.65:0.29:0.06. Using these probabilities, and assuming a linear dependence of the vacancy production probabilities on the DCA for DCA$<$ 0.15 Å, we apply the procedure described above to derive the spectra predicted by the simulations. Because of the uncertainty of the background subtraction procedure

applied to the experimental spectra, sophisticated optimization criteria for evaluating the fit of simulation to the experiment were deemed unjustified. In figure 3.4 the simulated spectra derived using the procedure above can be seen to compare favorably to the measured spectra.

We can also use what we have learned from the 1.2 and 2.0 keV simulations to extract the vacancy production probabilities at other DCAs. Mapping the DCA as a function of incident energy, we find the power law relation DCA$\simeq (67eV/E_{inc})^{0.549}$ Å; this, of course, is valid only for the present geometry. Because a discrete loss seems simply to shift the single scattering peak downward in energy without changing the weight of the peak, we can determine the vacancy production probabilities by placing peaks at the energies predicted by the BCM and then adjusting their weights until the resultant spectrum resembles the observed spectrum. The relative weights of the peaks are the vacancy production probabilities p_0, p_1, and p_2 at the DCA for the particular incident energy. This allows us to extrapolate vacancy production probabilities to other DCAs without having to resort to simulation. For 2.5 and 3.0 keV incident energies, we used this method to derive the vacancy production probabilities at $\mathrm{DCA}_{2.5keV} = 0.137$ Å and $\mathrm{DCA}_{3.0keV} = 0.124$ Å (again, see figure 3.4). We find acceptable fits between the experimental spectra and these estimated spectra by assuming that the single vacancy production probability increases linearly with decreasing DCA and that the double vacancy production probability remains constant for DCA < 0.15 Å. The vacancy production probabilities versus DCA are shown in figure 3.5.

3.4 Discussion

The clearest result of this study is the demonstration that the probability of vacancy production in hard collisions during ion-surface scattering turns on gradually as the distance of closest approach decreases. We note that this result is independent of whether or not we remove the uncontrolled background of scattered Li atoms. Our results contrast starkly with the simple Fano-Lichten model commonly used in MD

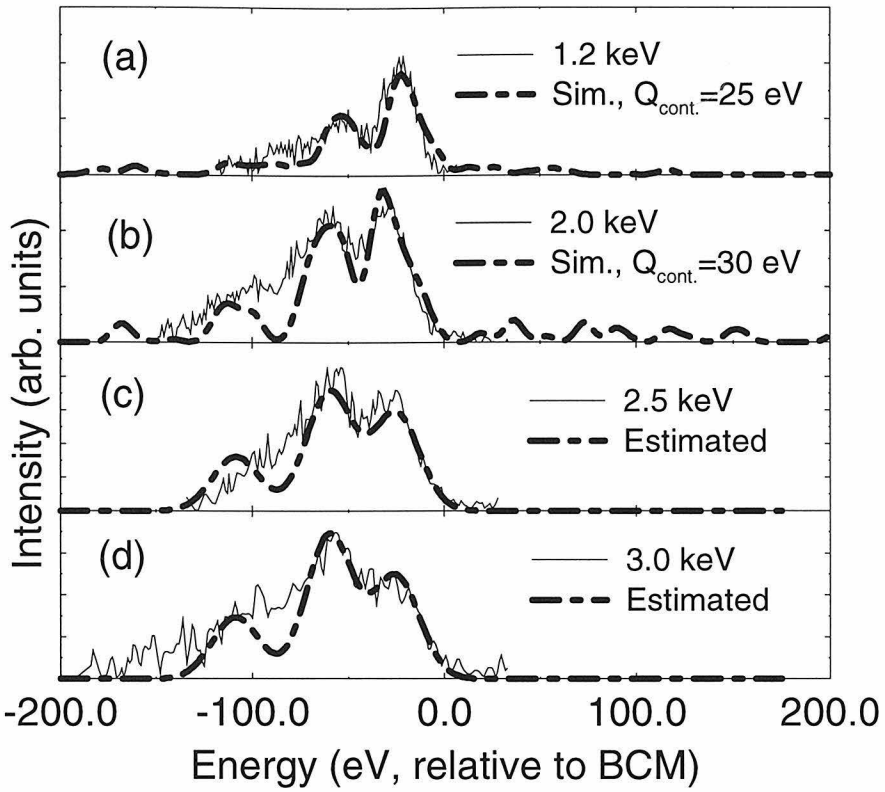

Figure 3.4: TOF spectra after an assumed smooth background (see figure3.1) has been removed. Also, in both (a) and (b), simulated elastic and inelastic spectra have been added together with weights chosen to match the experimental spectrum; the resulting simulated spectrum has also been shifted down in energy to reflect the effect of continuous losses suffered by the real ions but not modeled in the simulations. In (c) and (d), Gaussian peaks with relative separations predicted by the binary collision model are added together with weights chosen to fit the experimental spectrum. In each case, the relative weights of the simulated results or Gaussian peaks are the probabilities of producing zero, one, or two vacancies during the scattering process.

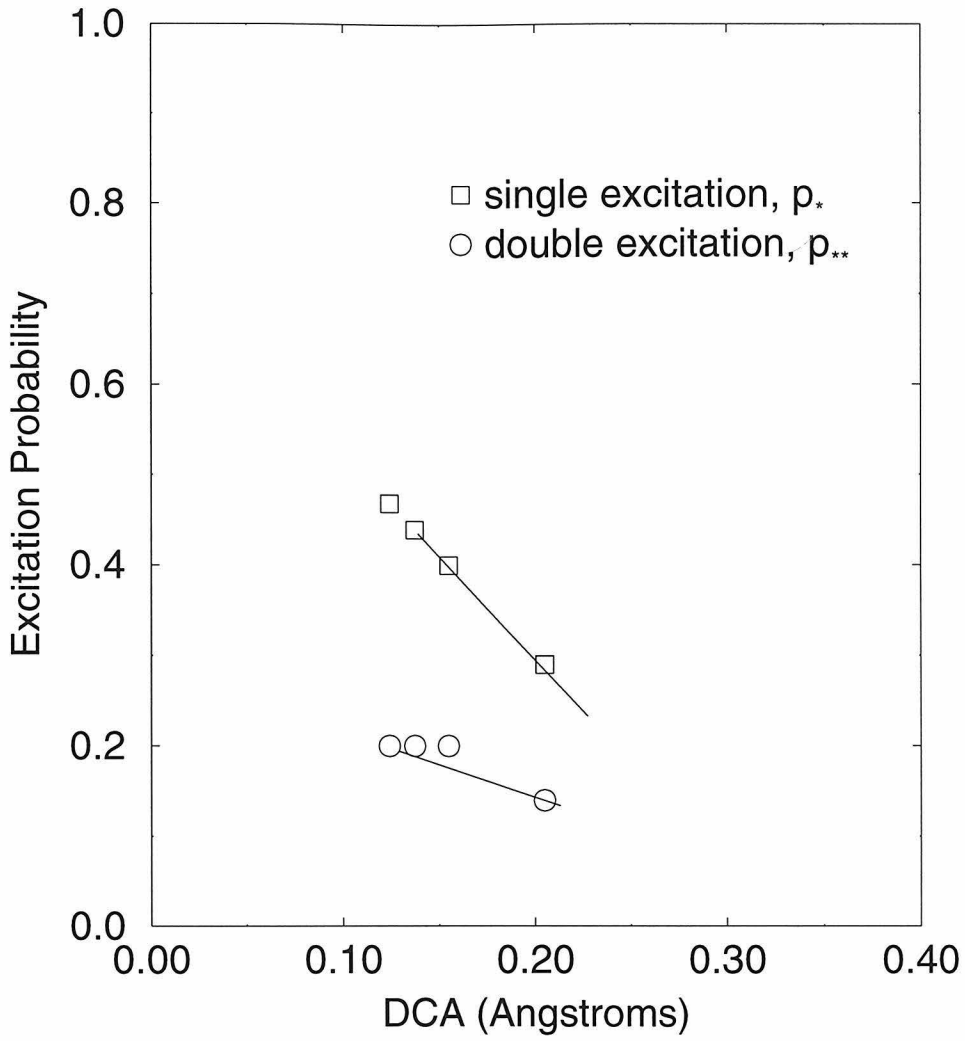

Figure 3.5: Single and double vacancy production probabilities implied by the fits in figure 3.4. For the spectra estimated by summing Gaussian peaks with separations set by the BCM, the formula DCA=$(67eV/E_{inc})^{0.549}$ was used to estimate the DCA for a particular incident energy in the present geometry.

simulations which assumes that the vacancy production probability has a step function dependence on the distance of closest approach.

We can understand the gradual turn-on of the vacancy production probability by considering the molecular orbital model description of the colliding Li and Al. When approaching the united atom limit in the molecular orbital theory of hard Li-Al collisions, the Li 1s orbitals evolve toward sulfur $3d\sigma$ orbitals, while the Al 2p, 3s, and 3p orbitals retain their character [10]. To illustrate the excitation mechanism, assume that the ground state configuration of the Al valence (n=3) electrons is $3s\sigma^2 3p\sigma^1$. Then the ground state valence (n=3) configuration of the Li-Al collision complex is $3s\sigma^2 3p\sigma^1 3d\sigma^2$ when the Li-Al separation is large. In the united atom limit, zero Li-Al separation, the ground state configuration must be $3s\sigma^2 3p\sigma^2 3p\pi^1$. This implies that during compression, and hence also relaxation, of the collision complex, the original configuration must become degenerate with many vacant configurations, *e.g.*, $3s\sigma^2 3p\sigma^2 3p\pi^1$, $3s\sigma^2 3p\sigma^1 3p\pi^2$, $3s\sigma^2 3p\sigma^1 3p\pi^1 3d\sigma^1$, etc. Mixing between these configurations and the original ground state configuration is responsible for the production of Li inner-shell vacancies: if the final configuration has a $3d\sigma^2$, $3d\sigma^1$, or $3d\sigma^0$ occupation, then zero, one, or two Li 1s vacancies result from the collision process, respectively.

A simple model of vacancy production might assume that the various configurations are degenerate at different Li-Al separations and occupation of the configurations after passing through the degeneracy is described by branching ratios. Then, as the Li-Al separation decreases, more degeneracies are passed providing more opportunities for the configuration to change. In this way, harder collisions provide more branching possibilities and hence a greater chance for vacancy production.

It is unclear that the valence electron wave-functions are well described by the isolated molecular orbital wave-functions ($3s\sigma, 3p\sigma$, etc.) when the collision occurs in bulk Al. In bulk Al, the valence electrons are more like free electrons than the isolated molecular orbitals assume. However, even though the relevant wave-functions and configurations may change, the spirit of the above argument should remain unchanged: At large Li-Al separation the Li 1s electrons are tightly bound beneath the

Fermi sea of Al valence electrons. As the Li-Al separation decreases, the Li 1s-like level is pushed into the valence band becoming roughly degenerate with the Al valence orbitals. At this point the various local electron configurations may suffer level crossings leading to possible occupancy transfers. Harder collisions lead to more crossings and possible transfers and hence a greater probability of Li vacancy production.

We wish to note that the importance of the molecular-dynamics simulations is twofold: first, they demonstrate that the weights of the scattered peaks are the same regardless of the loss imposed during the binary Li-Al collision (figure 3.4); and second, they show that the DCAs for scattering into the detector for a given incident energy are very sharply peaked (figure 3.2). These results should be easily generalizable to other systems in similar large-scattering-angle experimental configurations. Given a total atom spectrum displaying elastic and inelastic single binary scattering features P1, P2, etc., the probabilities of each of these events occurring during a binary collision are in the ratios W1:W2:,etc., where W1 is the weight of the peak corresponding to the first eventuality, etc. Then, if one can assume that the distribution of DCAs is sharply peaked at some value, the probabilities of the various outcomes may be determined as a function of the incident energy. Finally, if an interaction potential is assumed and a range of incident energies are available, the probabilities may be determined as a function of distance of closest approach, impact parameter, or other parameter of interest. In the present case we note that if we compute the DCA for a large scattering angle (*i.e.*, 180°) using the Moliere potential, the results agrees well with those seen in the simulation for incident energies $E_i > 1$ keV. Given a better approximation to the short range interaction potential, one could easily improve the derived dependence of the excitation probabilities p_* and p_{**} upon DCA.

We stress that the above procedure is valid only under certain assumptions. First, one must assume that a single hard scattering event is responsible both for scattering the incident ion into the detector and for causing the inelastic loss. If multiple small DCA scattering events lead to the ion finally being scattered into the detector, then one must adapt the molecular-dynamics loss procedure to deal the inelastic loss to each small DCA collision successively in separate runs of the same impact parameter.

Further, one must consider the possibility that more than one inelastic loss may occur during the multiple small DCA scattering events. Obviously, the implementation of such a procedure rapidly becomes very complicated. By restricting the investigation to large scattering angles and high incident energies, one can increase the probability that only single hard collisions are responsible for scattering the ion into the detector. Given such an experimental configuration, a scan of impact parameters by a molecular dynamics routine can then insure that the contribution of trajectories with multiple small DCA scattering events to the total yield of backscattered ions is small.

Chapter 4 Formation of clusters during large sputtering events

4.1 Introduction

During bombardment of a surface by $\sim$ keV/amu ions, target atoms may be sputtered as individual atoms or in clusters of two, three, or more atoms (monomers, dimers, trimers, *etc.*). While the production of monomers is well described by the linear cascade theories of Sigmund and Thompson [22], the production of clusters has no comparably successful description. Intrinsic interest in the processes which lead to the formation of clusters during sputtering is spurred by two maddeningly simple experimental observations: 1) in a variety of ion-target sputtering systems the yield of k-atom clusters is found to have a power law dependence, $Y_k \propto k^{-\delta}$, where $\delta \sim 4-8$ [23], and 2) the energy spectra of the k-clusters for clusters $k \geq 3$ have remarkably similar high energy asymptotes [24]. Both of these observations defy current attempts at explanation.

In this particular case, simulations of cluster producing processes can be particularly fruitful. The measurement taking capabilities of simulations – on admittedly greatly simplified systems – are far greater than those of a real experiment. Experimental measurements are typically limited to absolute yields and spectra – quantities which characterize the entire ensemble of possible sputtering events. Because the yield of clusters falls rapidly with cluster size, one expects that the ensemble of sputtering events responsible for producing large clusters might not resemble the entire distribution of sputtering events. Simulations, with their single event integrations, can identify the cluster producing events trivially and demonstrate what event characteristics lead to cluster production.

The distribution of event sizes is often ignored when considering sputtering pro-

cesses – despite the fact that there is a large variance in the number of atoms sputtered after any given ion impact [25]. The formation of atomic clusters during sputtering is a situation where intuition suggests that the size of the individual impact events may be of great importance; however, experimental measurements of such a correlation are difficult because they would require an impact by impact evaluation of the yield of sputtered atoms and clusters. As yet, such measurements have not been attempted. In the absence of data, theoretical treatments of cluster formation also have neglected dependence on event size, even though the only present quantitative model of cluster formation, the recombination model, is easily generalizable to include such dependence. The primary assumption of the recombination model is that atoms are sputtered in a completely uncorrelated manner and that clusters form accidentally when multiple atoms happen to be sputtered from nearby positions at nearly the same time and with momentum differences small enough to allow the inter-atomic potential to bind them all together into a cluster. The recombination models of Konnen *et al.*and subsequent generalizations begin with the average flux of atoms and assume the recombination proposition to predict (with limited success) the energy spectra of clusters of various sizes [26]. Gerhard considers the flux from a single average event to derive the yield of dimers relative to monomers [27]. Implicit in both types of recombination models is the assumption that only the 'average' sputtering event is important. We find that this is not the case. During a single sputtering event, all atoms are sputtered from the vicinity of the initial impact whether the event is large or small, *i.e.*, whether many or few atoms are sputtered. Considering this, it is clear that the recombination proposition will result in disproportionately more clusters being produced during larger (and hence denser) sputtering events.

Recent sputtering experiments by Lill *et al.*[28] using liquid indium-gallium targets indicate the importance of event size in the production of clusters. In In-Ga targets, Gibbsian segregation pulls the relatively strongly interacting Ga into the bulk leaving the surface with a high concentration of In. As the depth into the target increases, the bulk Ga concentration is quickly attained [29]. Because the target is liquid, if the flux of the sputtering beam is low enough, any region damaged by sputtering can

reequilibrate to the indium-on-top concentration profile before the next impact in the region occurs. When investigating the mass spectra of clusters sputtered from these targets, Lill *et al.*observe that the average Ga content of the clusters increases with cluster size [28]. They find that the mass spectrum of k-clusters is fit by a binomial distribution

$$P(M_k) = \frac{k!}{(k-n_{Ga})!n_{Ga}!}(1-x_{Ga})^{k-n_{Ga}}x_{Ga}^{n_{Ga}} \tag{4.1}$$

in which M_k is the total mass of the k-cluster, $k - n_{Ga}$ and n_{Ga} are the number of indium and gallium atoms in the cluster, and $1 - x_{Ga}$ and x_{Ga} are the concentrations of indium and gallium atoms in the mass spectrum. Because the target continually reestablishes the equilibrium concentration profile, this implies that the average depth of origin of atoms in a cluster is increasing as the cluster size increases. If the cluster is formed and ejected intact from within the target, the material above it must also be sputtered. Alternatively, if the cluster is formed by recombination above the surface, the high Ga content suggests that the event has been violent enough to sputter atoms from beneath the surface. Both interpretations imply that clusters are produced during events which sputter many atoms. Still, this does not provide a direct link between the production of clusters and the size of the individual sputtering events.

Molecular Dynamics (MD) simulations of sputtering events provide access to details of the process which are not easily observed in the laboratory. Because an MD simulation deterministically integrates impacts and subsequent sputtering events one at a time, the correlation of clusters to their depth of origin and to the total number of atoms sputtered during the event is automatic. We have performed a series of 3 keV $Ar^+ \rightarrow$ In-Ga (liquid) simulations which confirm a strong correlation between production of large clusters and the size of the individual sputtering events. We also find that this trend in cluster production is predicted by a simple generalization of the recombination model; we present this model below, with the hope that it can be useful in designing experiments to investigate such effects in greater detail.

4.2 Formation of Clusters During Uncorrelated Emission

The limitations of the recombination model are commonly known; in particular the model fails to predict the shape of the observed energy spectra of sputtered atomic clusters. However, the recombination of uncorrelated sputtered atoms into clusters is an intuitively appealing and easily understood model whose development provides valuable intuition about the formation of clusters. Also, when compared to simulation or experiment, it provides an estimate of the number of cluster emissions resulting from correlated emission effects.

The basic assumption of the model is that atoms are sputtered from the target in an uncorrelated fashion and that a k-cluster forms when k atoms happen to be sputtered with similar momenta, from nearby positions, and at nearly the same time. The uncorrelated atoms have a probability density $\frac{dN}{d\gamma}(\gamma)$ of being sputtered from the initial position $\mathbf{x}$ with a momentum $\mathbf{p}$ at the time t, where $d\gamma \equiv d^3x d^3p dt$ and $\gamma \equiv (\mathbf{x}, \mathbf{p}, t)$. By definition the total number of atoms sputtered is $N \equiv \int d\gamma \frac{dN}{d\gamma}(\gamma)$. We stress that we are deriving the expected yield of k-clusters during a single event which sputters N atoms.

If k atoms form the cluster then the origin of the cluster is $\mathbf{x} = \frac{1}{k}\sum_{i=1}^{k} \mathbf{x_i}$, the momentum of the cluster is $\mathbf{P} = \sum_{i=1}^{k} \mathbf{p_i}$, and the time of cluster sputtering is $t = \frac{1}{k}\sum_{i=1}^{k} t_i$. The cluster will be bound only if its internal energy is less than its dissociation energy.

If we assume that all atoms are emitted in a uncorrelated manner according to the probability density $\frac{dN}{d\gamma}$, then the N-atom correlation function is

$$\rho_N(\gamma_1, \ldots, \gamma_N) = \frac{1}{N}\frac{dN}{d\gamma_1} \cdots \frac{1}{N}\frac{dN}{d\gamma_N}. \tag{4.2}$$

We can write the probability density for k-cluster emission as

$$\frac{dY_k}{d\gamma}(N) = \int d\gamma_1 \ldots d\gamma_N B_k(\gamma_1, \ldots, \gamma_N)\rho_N(\gamma_1, \ldots, \gamma_N), \tag{4.3}$$

where B_k ensures that k, and only k, of the N atoms combine into a cluster and enforces $\gamma = \frac{1}{k}\sum_{j=1}^{k}\gamma_{i_j}$. Here $\gamma \equiv (\mathbf{x}, \mathbf{p}, t)$ is the position, momentum per cluster atom, and sputtering time of the k-cluster, and $i_j \in (1, N)$.

We can approximate the expression for the cluster yield by noting that for k atoms to join into a k-cluster with phase per atom $\gamma \equiv (x, p, t)$, they all must be emitted from a small region of phase space $\Delta\gamma \simeq \Delta^3 x \Delta^3 p \Delta t$ about γ. For the atoms to be bound, they must be emitted within the range of the binding potential of each other, and with a small enough momentum difference that the potential is strong enough to bind them to the cluster. If the binding potential has a minimum $-V$ at separation a, then we can estimate $\Delta^3 x \sim a^3$ and $\Delta^3 p \sim (2mV)^{3/2}$. For the atoms to be bound to the cluster, they must be sputtered within $\Delta t \sim am/p$ of the cluster sputtering time; p/m is the average velocity of atoms in the cluster, so this is the time the cluster requires to travel further than the range of the potential; if an atom is not emitted during this time, it will not join the cluster. For a k-cluster to be formed, k of the N atoms must be within $\Delta\gamma \sim a^3(2mV)^{3/2}am/p$ of each other while the other N-k atoms must be away from this volume. The probability that a particular 1 of the N sputtered atoms happens to be sputtered from $\Delta\gamma$ about γ is $\frac{\Delta\gamma}{N}\frac{dN}{d\gamma}$, so the probability that k (and no more) of the atoms are sputtered from there is

$$\Delta\gamma \frac{dY_k(N)}{d\gamma} \simeq \frac{N!}{(N-k)!k!}(1 - \frac{\Delta\gamma}{N}\frac{dN}{d\gamma})^{N-k}(\frac{\Delta\gamma}{N}\frac{dN}{d\gamma})^k. \tag{4.4}$$

We can begin to simplify this expression by assuming that the single atom sputtering density, $\frac{1}{N}\frac{dN}{d\gamma} \equiv \frac{1}{N}\frac{dN}{d^3x d^3p dt}$, is separable, that the rate of sputtering slows exponentially and is characterized by a time constant τ, that the N atoms in the event are sputtered uniformly from a volume Ω of the target about the initial impact, and that the momentum distribution of the sputtered atoms satisfies a Sigmund-Thompson distribution. Then, after some manipulation, the probability of an atom being captured by the cluster emitted with phase per atom γ can be written

$$\Delta\gamma \frac{1}{N}\frac{dN}{d\gamma} \simeq \quad (z\alpha)e^{-t/\tau}\frac{\cos^q\theta}{(1+\epsilon/U)^{n+1}} \qquad \mathbf{x} \in \Omega, t > 0,$$

$$\simeq \qquad 0 \qquad , elsewhere, \tag{4.5}$$

where U is the 'binding energy' of atoms to the surface, $\epsilon = p^2/2m$ is the kinetic energy of the atom, and

$$z\alpha = z\frac{n(n-1)(q+1)}{\pi}\frac{a^3}{\Omega}(\frac{V}{U})^{3/2}\frac{ma/\tau}{\sqrt{2mU}} \tag{4.6}$$

is a dimensionless constant which indicates how effectively recombination of uncorrelated emissions produces clusters. The parameter $z \sim 1$ is introduced by the crudeness of our approximation for $\Delta\gamma$: $\Delta\gamma \simeq za^3(2mV)^{3/2}ma/\sqrt{2m\epsilon}$.

If we work under the assumption $z\alpha \ll 1$, then we can further simplify equation 4.3. Since $\frac{\Delta\gamma}{N}\frac{dN}{d\gamma} < z\alpha$ we can approximate $(1 - \frac{\Delta\gamma}{N}\frac{dN}{d\gamma})^{N-k} \simeq 1$. Generalization to larger $z\alpha$ is straightforward but unnecessary in the present case. Typically, the entire phase space distribution of clusters is inaccessible. If we integrate away the spatial and time dependence, and make the substitution $E = k \cdot \epsilon$, where E is the translational energy of the k-cluster, we find

$$\frac{dY_k(N)}{dEd(\cos\theta)} \simeq \frac{N!}{(N-k)!k!}\frac{n(n-1)(q+1)(z\alpha)^{k-1}}{k^2}\frac{E}{kU^2}(\frac{\cos^q\theta}{(1+E/kU)^{n+1}})^k. \tag{4.7}$$

An important consequence of equation 4.7 is that the yield of k-clusters from an event of size N, $Y_k(N) = \int dEd(\cos\theta)\frac{dY_k(N)}{dEd(\cos\theta)}$, scales as $\frac{N!}{(N-k)!k!}\alpha^{k-1}$ or, for $k \ll N$, $Y_k(N) \sim N^k/\Omega^{k-1}$. This immediately implies that if the initial density of sputtered atoms increases as the events get larger, then the production of clusters becomes more likely during larger events. In fact, as we increase the event size, we should see faster than linear growth of the production of dimers, faster than dimer growth of the production of trimers, *etc.* This pattern of growth will continue until the increase of the initial density N/Ω saturates at the density of the target. In this model the average yield of k-clusters after many sputtering events is the sum of the individual yields from events of size N, each weighted by the probability that a randomly placed impact results in an event of that size: $Y_k = \sum p(N)Y_k(N)$. Large events are less likely than small events, but because of the geometric growth of the probability of k-

cluster production with N (until the initial density saturates) the total yield of larger and larger k-clusters is dominated by larger and larger events.

4.3 Results and Discussion

The results we present are of approximately 30,000 simulated $Ar^+ \rightarrow$ In-Ga (liquid) sputtering events. Before the sputtering event, targets were "melted" for many picoseconds to allow the In-Ga concentration profiles to equilibrate. On each target, 400 separate impacts were evolved, and a total of 78 targets were used. Morse pair potentials, with attractive minima of $\sim$ -0.3 eV at $\sim$ 4 Å, were used to simulate equilibrium interactions between the indium and gallium atoms in the target. At closer separations Moliere potentials were used, cubic splines were interpolated between these regions. The Ar^+ ion interacted with both In and Ga atoms through appropriate Moliere potentials. For a more detailed discussion, see reference [30].

In spite of the great number of simulations, the simulated yield of large clusters was small. We found no clusters of more than four atoms. Still there are a number of interesting and relevant conclusions suggested by the analysis of our simulations.

A possible interpretation of the observation of Lill *et al.*[28] that larger clusters sputtered from In-Ga targets have a greater Ga content, is that large clusters come from deeper within the target. Because atoms sputtered from beneath the surface typically are more energetic, such a result could help to explain the recombination model's failure to predict the proper energy spectra of large k-clusters: more energetic k-clusters are seen than the recombination model predicts because clusters are not formed from the entire spectrum of sputtered atoms; they are formed from the more energetic atoms sputtered from deep within the target. In the results of our simulations we find that the depth of origin of sputtered k-clusters, defined by $x_\perp = \frac{1}{k}\sum x^i_\perp$, is weakly correlated to the size of the cluster. In figure 4.1 a gradual trend indicating that larger clusters come from deeper within the target is suggested. Because we know the distributions of depths of origin of the atoms in monomers, dimers, and trimers, and can measure directly the concentrations of indium and gallium in the simulation

targets as a function of depth (see figure 4.2), we can calculate the expected concentration of indium and gallium in the different sized clusters. In figure 4.2 we see that the concentration of Ga in ejecta sputtered from a given depth is greater than the concentration of Ga at that depth. The lighter mass of gallium leads to its preferred sputtering; this effect suggests the possibility that mechanisms responsible for cluster formation may also preferentially create clusters with high gallium content. In figure 4.3 we present mass spectra of the monomers, dimers, and trimers formed during the simulation; each spectrum has been normalized to unity. Clusters are sputtered with indium concentrations x_{In} of 0.809, 0.76, 0.82, and 0.63 for monomers, dimers, trimers, and tetramers, respectively.

According to the interpretation of Lill *et al.*, we expect the indium concentrations of the k-clusters to reflect the depth from which the atoms in the cluster were sputtered, $x^{In}_{k,eff} = \int x^{In}(z)\frac{dN}{dz}(z)dz/N_{in\,k-clusters}$. We can take into account the result that gallium is more easily sputtered from under the surface (see figure 4.2) by using the sputtered indium concentration instead of the target indium concentration for $x^{In}(z)$. We find these expected concentrations to be 0.809±0.002, 0.78±0.02, 0.81±0.08, and 0.67±0.23 for monomers, dimers, trimers, and tetramers, respectively; error estimates (67% confidence) have been calculated by considering the finite number of k-clusters formed during the simulation: the observed concentration may not be the same as that of the parent distribution. If we use the actual concentration of indium in the target as a function of depth to predict the indium concentration in the clusters, the predicted indium concentrations are 0.815, 0.79, 0.81, and 0.69 for the monomers, dimers, trimers, and tetramers, respectively; the indium concentrations of the monomers and dimers deviate from that seen in the simulation by a possibly statistically significant amount. To within statistical uncertainty, our results confirm the proposition of Lill *et al.*that the gallium content of the clusters reflects their depths of origin and support their claim that larger clusters originate from a greater depth beneath the target surface.

While the depth of origin is weakly correlated to cluster size, we find a much stronger correlation between cluster size and the distance between the sites of its

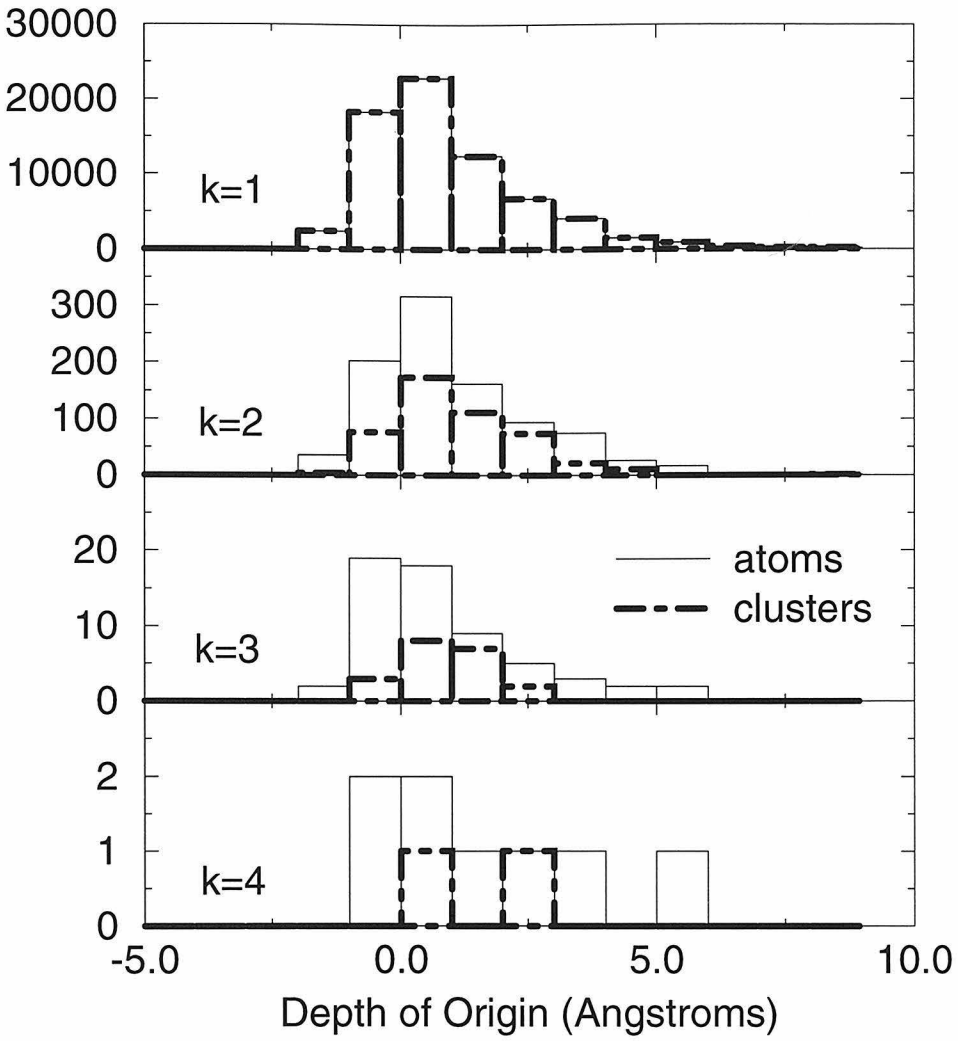

Figure 4.1: The distributions of depths of origin of clusters and atoms within those clusters. A weak trend of larger clusters coming from deeper within the target is seen. The vast majority of atoms are sputtered from within one atomic diameter ($\sim$ 4 Å) of the target surface.

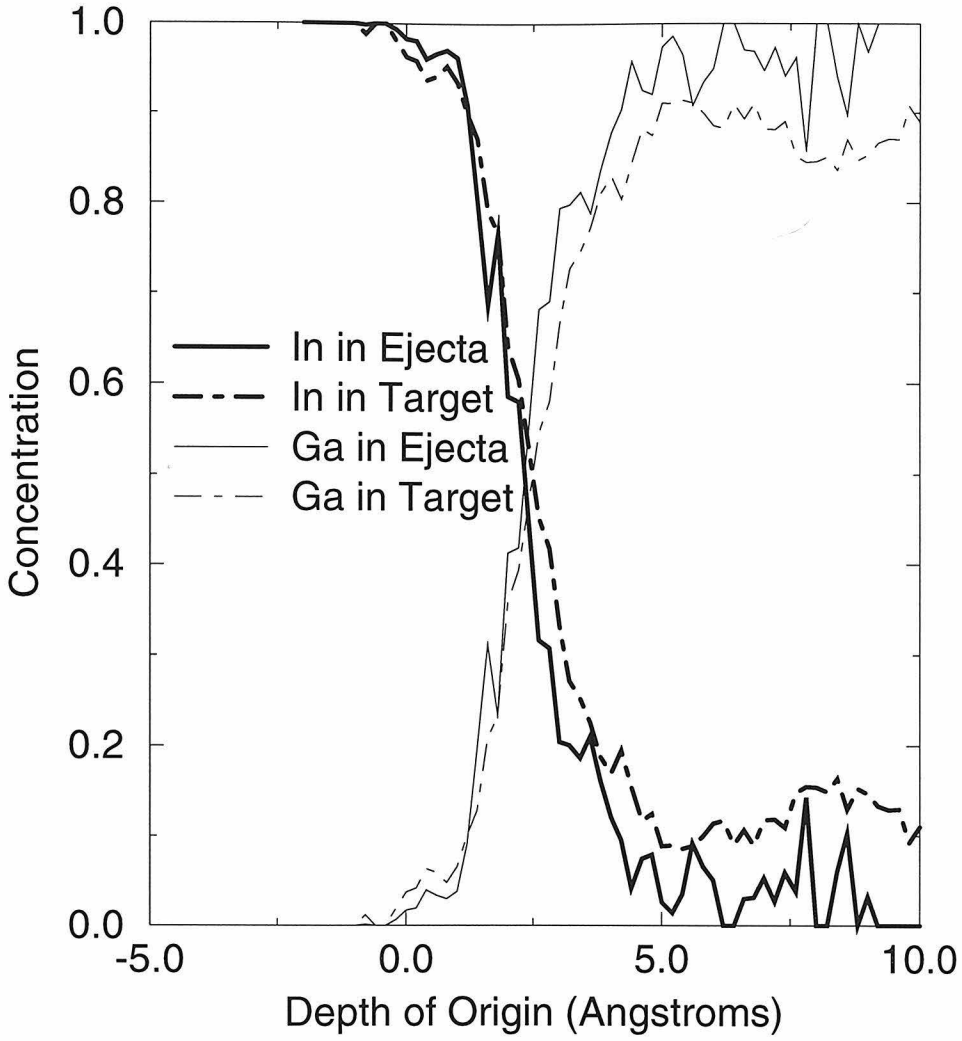

Figure 4.2: The concentrations of indium and gallium in the target at a given depth and in the ejecta sputtered from a given depth. Gallium is seen to be preferentially sputtered.

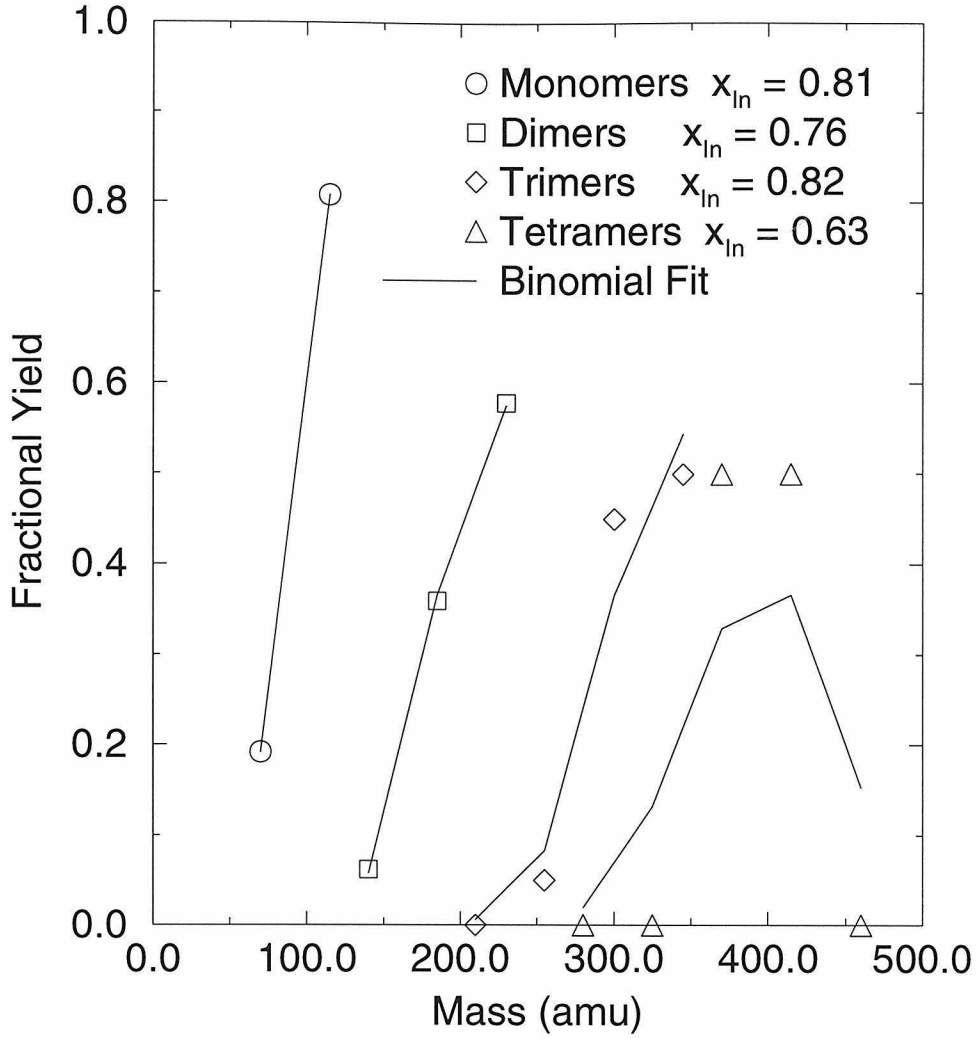

Figure 4.3: The spectra of cluster masses seen in the simulation. Fits to the statistical prediction $P(n_{In}, n_{Ga}) = (n_{In} + n_{Ga})! x_{In}^{n_{In}} x_{Ga}^{n_{Ga}} / n_{In}! n_{Ga}!$ with the overall k-cluster indium concentration (x_{In}) are also shown.

emission and the sputtering ion impact. Larger clusters are emitted further from the initial impact (see figure 4.4). This agrees with the results of $Ar^+ \rightarrow$ Cu (111) simulations performed by Betz and Husinsky [31]. They found that the cascades produced by the impact of the ion produced a large circular mound of atoms, and that large clusters were sputtered late in the development of the cascade and from the edge of the mound. We note that none of these results are consistent with the formation of clusters by uncorrelated sputtering of atoms. In figure 4.4, the majority of atoms are seen to be sputtered from very near the impact site; thus, the recombination model would predict that clusters should be most readily formed in this same region. Neither our results nor those of Betz and Husinsky support this; this indicates that some correlated motion taking place far from the impact site and late during the cascade development must contribute to cluster production. From our development of the recombination model, we expect that the production of clusters is most effectively accomplished by large events. In figure 4.5 we have separated the yield of clusters according to the size of the event, N, which produced them. Figure 4.6 shows the frequency with which events of size N were produced during the Ar^+ sputtering of the In-Ga targets. While the total number of trimers and tetramers is insufficient to produce a smooth distribution of clusters per event size, we do see strong trends in the distributions which indicate that larger clusters are produced primarily by larger events.

Recombination of uncorrelated emissions predicts that events with high initial density of sputtered atoms more efficiently produce large clusters. Typically, atoms are sputtered from within several atomic diameters of the initial ion impact site and from the first layer of the surface. If one assumes that small and large linear-cascade events differ in that the large events are simply collections of interpenetrating small events, then it is rational to assume that the sputtering volume about the impact site is independent of event size. Hence $N/\Omega \sim N$, and the recombination model predicts the dependence $Y_k(N) \sim N^k$. Because the frequency of production of events of size N during our $Ar^+ \rightarrow$ In-Ga (liquid) simulations scales roughly as $\exp(-0.22N)$ (see figure 4.6) we expect the total production of k-clusters by events

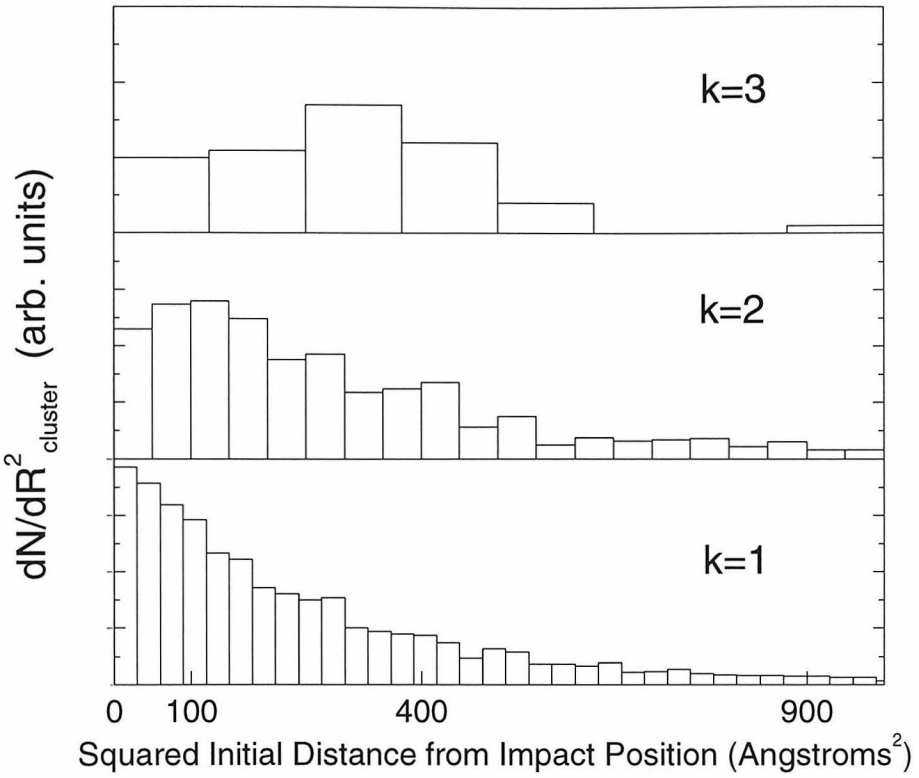

Figure 4.4: The distribution of distances from the cluster origin to the initial ion impact. Distances are binned according to R^2 so that the distribution is normalized to constant area. Larger clusters are seen to originate farther away from the impact site.

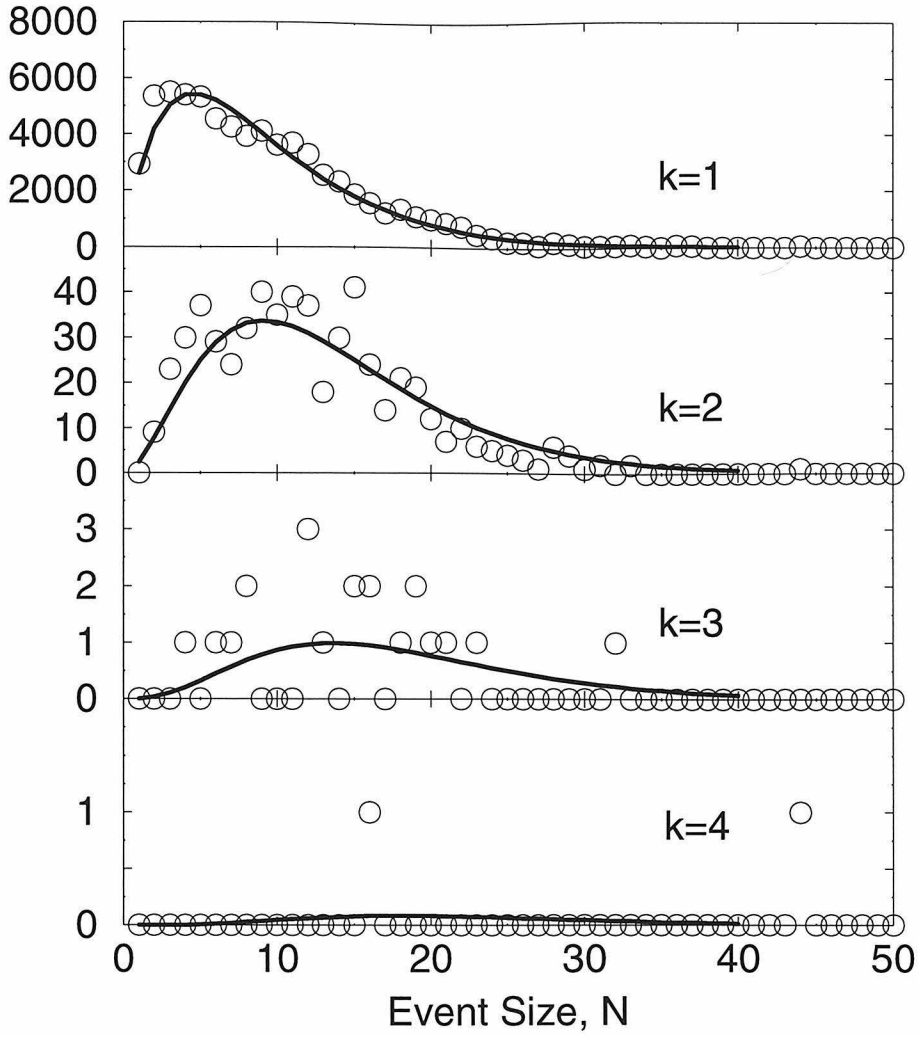

Figure 4.5: The total yield of k-clusters from all events of each size N. Larger events are seen to be responsible for the production of larger clusters. Also included are the predictions of the recombination model for the total yield of k-clusters given the frequency of event production: $N^k \exp(-0.22N)$, where the normalization has been chosen so that the absolute cluster yield agrees with that of the simulations.

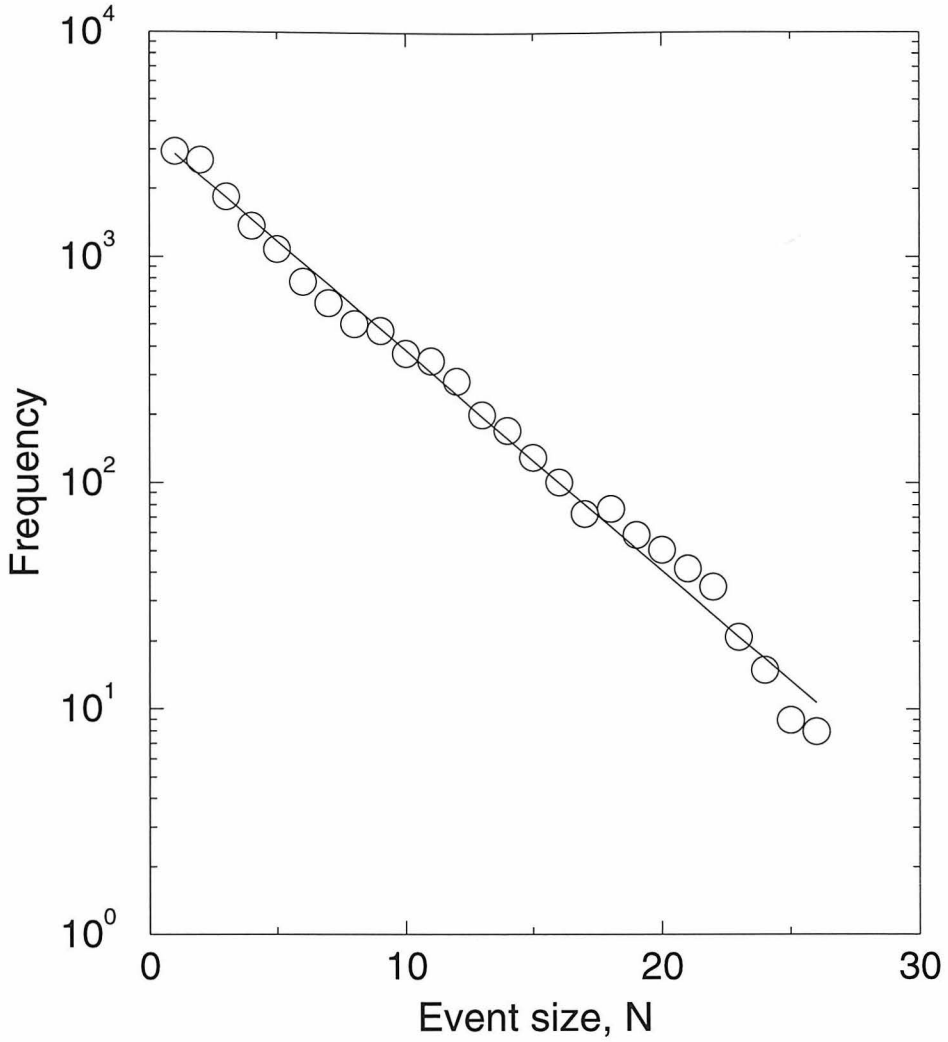

Figure 4.6: The distribution of events of size N produced during the simulations. The probability of the 3 keV $Ar^+ \rightarrow$ In-Ga (liquid) impact producing an event of size N is proportional to $\exp(-0.22N)$.

of size N to scale as $N^k \exp(-0.22N)$. Figure 4.5 includes fits of this form which have been normalized to the absolute yield of k-clusters. To within counting error, the predictions of the recombination model are seen to agree well with the simulation results for the formation of small clusters.

One hope of including the distribution of event sizes within the recombination model is that it may fix the model's predictions of the high energy asymptotes of the energy distributions of k-clusters, $\frac{dY_k}{dE} \sim E^{1-k(n+1)}$, which is known to decay more sharply than observed spectra. Because we have demonstrated that larger clusters are produced dominantly by larger events, if we could demonstrate that larger events sputter a distribution of more energetic atoms, then we could argue that the cluster distribution should also be more energetic. Unfortunately, the energy spectra of very large events are difficult to determine because the events occur infrequently. When studying the energy distributions of particles sputtered from events of a given size N, we are unable to discern a deviation of the distribution of sputtered atoms from the Sigmund-Thompson form with the usual exponent n=2.

If we independently examine the energy spectra of indium and gallium (see figure 4.7), we find that while the indium has a high energy asymptote $\sim E^{-2}$, the gallium energy spectrum asymptotes to a more gradual $E^{-1.5}$; the gallium spectrum is harder because slow moving gallium sputtered from beneath the surface are filtered by atoms on the surface. We also find that the concentration of gallium sputtered during events of size N gradually increases from about 17% in 1 or 2 particle events to about 21% for events of 15 or more particles. While these two results are consistent with the proposition that larger events may have a more gradual decay of their high energy spectra than does the spectrum of atoms sputtered from events of all sizes, the trends are not strong enough to salvage the energy spectra predictions of the recombination model. From the $\sim N^k \exp(-0.22N)$ fit of the total yield of k-clusters from events of size N, we predict that k-clusters are produced mainly by events of size $k/0.22$. If the observed high energy asymptote of the k-cluster spectra is $E^{-\delta_k}$, the recombination model requires events of size N $\sim$ k/0.22 to have atomic energy spectra with the asymptote $E^{-(\delta_k+1-k)/k}$. Because δ_k is typically observed to be independent of k and to

have a value of order 3.0 or 4.0 [24], one discovers the absurd requirement that atomic spectra for large events must have a divergent asymptote. Unless atoms are sputtered from these large events according to an energy distribution not described by a power-law, this indicates that even with the inclusion of event size, the recombination model has no hope of completely describing the formation of large clusters.

Still, one hopes that recombination describes the formation of at least some of the k-clusters produced, and that for small clusters it accounts for a significant fraction of the yield. Assuming that all events sputter roughly the same energy and angular distribution of atoms simplifies the predictions of the recombination model. Because the exponents n and q in equation 4.7 are assumed independent of N, we can fit the parameters of the Sigmund-Thompson distribution by fitting the total energetic and angular spectra of sputtered atoms. We find that the spectra are fit well by assuming q = 2.3, n = 2.0, and U = 2.3 eV (not shown). Given that the probability of producing an event of size N during these simulations has been found to be P(N)=$e^{-\beta N}(1-e^{-\beta})$ (see figure 4.6), we can predict the total yield of k-clusters to be

$$\begin{aligned} Y_k &= \int dEd(\cos\theta) \sum P(N) \frac{dY_k(N)}{dEd(\cos\theta)} \\ &= \frac{1}{k} \frac{(z\alpha)^{k-1}}{(e^{\beta}-1)^k} \frac{n(n-1)(q+1)}{(kq+1)[(n+1)k-2][(n+1)k-1]}. \end{aligned} \tag{4.8}$$

All the parameters are fixed except the sputtering volume Ω (a factor in α) and z (assumed to be of order unity). During the simulations we found that a 70Å by 70Å target was large enough to contain the vast majority of sputtered atoms. Thus, because most sputtered atoms come from the first atomic layer of the target, we expect the sputtering volume to be some fraction of the volume of the first layer of the target. If we match the relative simulation yields of dimers and monomers to the prediction of equation 4.8, we find that we require $z\alpha = 0.064$ so that $\Omega/z = 1200$ Å^3, *i.e.*, $\Omega = (4\text{Å})\ \pi r^2$ where r = 10 Å$/\sqrt{z}$, an acceptable result which indicates that most of the atoms sputtered come from within several atomic diameters of the initial ion impact site. Using this result, we predict the yield of trimers and tetramers and compare the predictions to the results of the simulations in figure 4.8. Also included

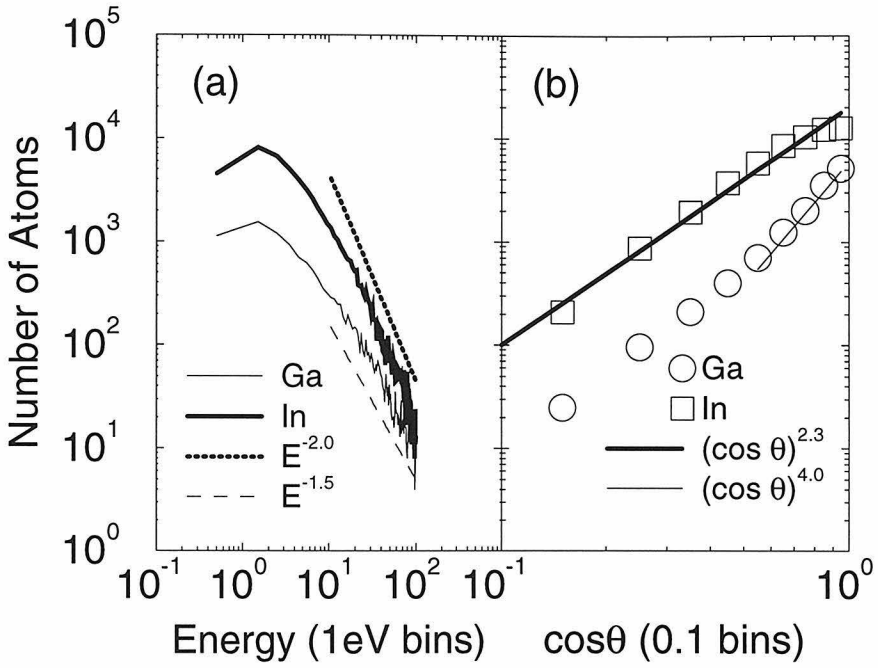

Figure 4.7: (a) The energy spectra of indium and gallium monomers. The asymptotic functions $E^{-1.5}$ and $E^{-2.0}$ are included for comparison. (b) The angular spectra of indium and gallium monomers. The gallium distribution is much more forwardly peaked than that of indium because the first layer of the target is nearly all indium.

in the figure for comparison is the power law fit $Y_k \sim k^{-\delta}$ with $\delta = 8.1$. The most obvious thing to note about the uncorrelated recombination prediction for the yield of k-clusters is its exponential decay with cluster size. We discuss this in more depth below.

Having fixed all the parameters in the recombination model, we can compare its predictions to the results of the simulations. The total energy or angular spectrum is found by integrating away the irrelevant variable in $\frac{dY_k}{dEd(\cos\theta)} = \sum P(N) \frac{dY_k(N)}{dEd(\cos\theta)}$. The recombination predictions are

$$\frac{dY_k}{dE} \simeq \frac{(z\alpha)^{k-1}}{(e^{\beta}-1)^k} \frac{n(n-1)(q+1)}{(kq+1)k^2} \frac{E/kU^2}{(1+E/kU)^{k(n+1)}} \tag{4.9}$$

for the energy spectra, and

$$\frac{dY_k}{d(\cos\theta)} \simeq \frac{(z\alpha)^{k-1}}{(e^{\beta}-1)^k} \frac{n(n-1)(q+1)}{k[k(n+1)-2][k(n+1)-1]} \cos^{kq}\theta \tag{4.10}$$

for the angular spectra. In figure 4.9 a and b we present both the recombination predictions and the simulation results; the recombination predictions have been scaled so that the monomer spectra, which are fits to the simulated spectra and taken as inputs for the recombination model, have the same magnitude as the simulated spectra. Because the monomer energy spectrum is well fit by the assumption n=2, the model predicts that the dimer energy spectrum should asymptote to $E^{1-(n+1)k} \sim E^{-5}$. In the simulations the dimer energy spectrum asymptotes to $E^{-3.2}$ in rough agreement with a variety of MD and experimental results [24] and, as usual, in contradiction with the recombination model.

We note that the maximum of the dimer spectrum occurs at a higher energy than that of the monomer spectrum. This agrees with experimental observations by Lill *et al.*[32] of a variety of systems which indicate that typically $E_1^{max} \leq E_2^{max}$. This contradicts the uncorrelated recombination model which predicts the peak energy, $E_k^{max} = U/(n+1-1/k)$, of the k-cluster spectra to occur at *smaller* energies for larger clusters. For clusters larger than dimers, they see the peak energy decrease which is

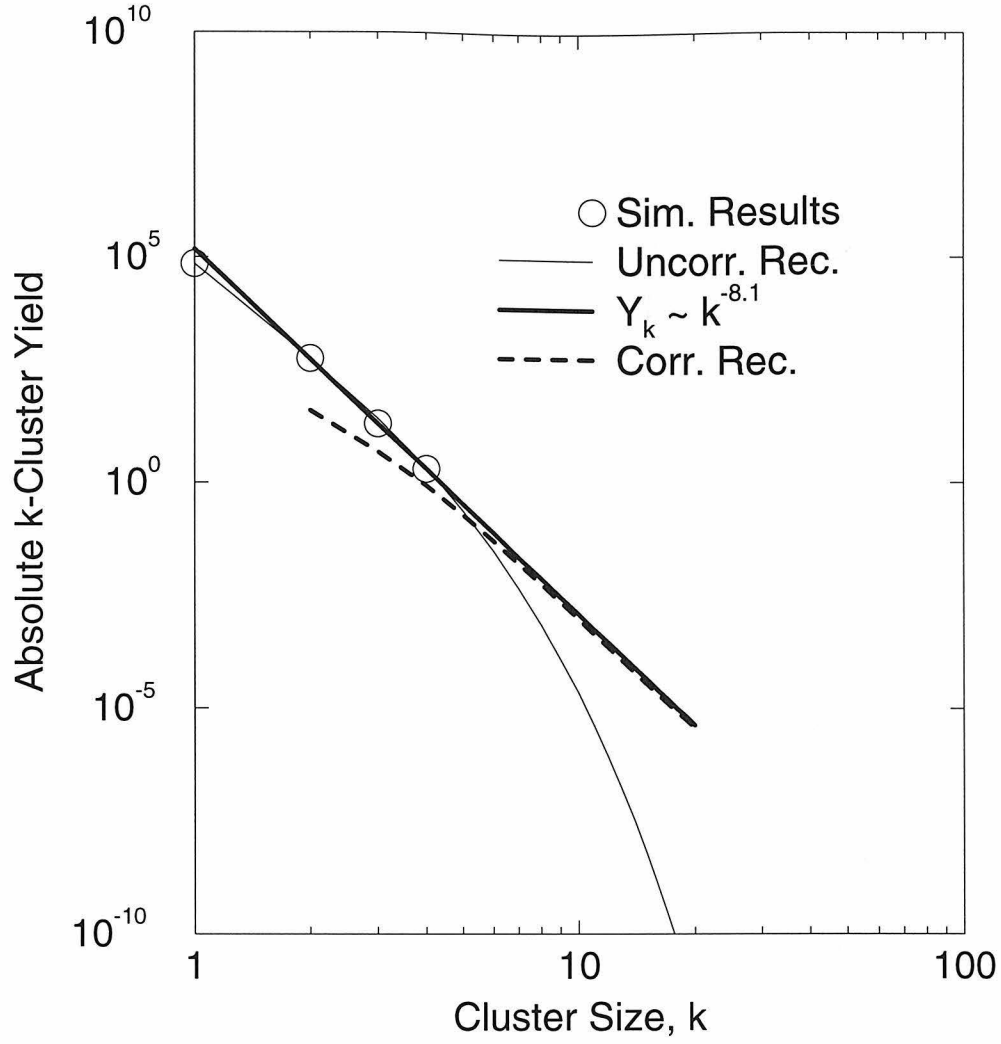

Figure 4.8: The yield of k-clusters in the simulation, the recombination prediction, and the power law fit $Y_k \sim k^{-8.1}$. Note the exponential decay of the uncorrelated recombination prediction. Also included is the prediction of a simple model of the recombination of correlated emissions into k-clusters.

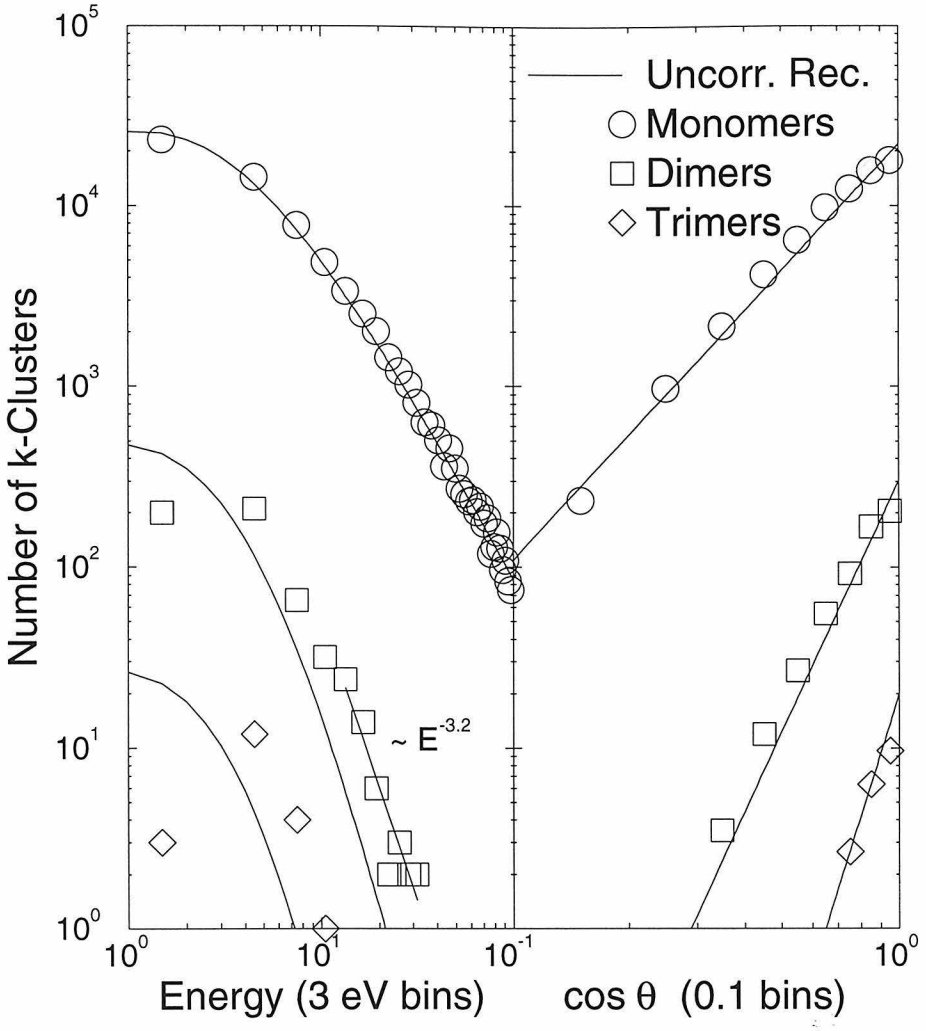

Figure 4.9: (a) The energy spectra of clusters and the recombination prediction. The yield of high energy clusters is under predicted by the uncorrelated recombination model. (b) The angular spectra of clusters and the recombination prediction.

consistent with the predictions of the model. (The statistics of our simulated trimer spectrum are unfortunately too poor to comment on this.) However, the model's failure with the dimer spectra is significant because uncorrelated recombination should be most effective in producing small clusters. As noted below, the production of larger clusters by uncorrelated recombination is suppressed exponentially so that some other production mechanism must occur.

If we separate the indium and gallium angular spectra, we find that the gallium spectrum is peaked forward strongly, obeying $\sim (\cos\theta)^4$ for small angles from the normal, while the indium spectrum follows the more gradual $\sim (\cos\theta)^{2.3}$. The sharp forward peak in gallium sputtering agrees with the observations of Hubbard *et al.*[33] and is due to the forward 'steering' of atoms sputtered from beneath the surface by the atoms on the surface. The angular spectra of the k-clusters are best fit by ignoring the species of the atoms forming the cluster and using the total atom exponent $\frac{dN}{d(\cos\theta)} \sim (\cos\theta)^{2.3}$.

The event-size-correlated recombination model seems to offer an explanation of observations that systems with large sputtering yields tend to have greater cluster yields and hence smaller power law exponents [34]. For systems with an event size probability distribution like the present P(N) $\sim e^{-\beta N}$, the average sputtering yield is roughly $1/\beta$. In equation 4.8 we see that larger average yields, smaller β's, lead to more clusters being formed. However, this apparent success is tempered by the observation that the uncorrelated recombination model predicts an exponential decay, $Y_k \sim (z\alpha/\beta)^k$, of the production of large clusters. Because there are a number of observations that a power law yield $Y_k \sim k^{-\delta}$ is satisfied for clusters up to size k = 20 and beyond [34], we must conclude again (just as with the increasing distance of origin of large clusters from the ion impact site and the failure of the energy spectra predictions) that some correlated process also contributes to cluster production.

To illustrate how a correlated emission process might lead to a power law dependence of the cluster yield, consider the following. A strong correlated motion present near the surface of the target might lead to a large number of neighboring atoms being ejected at the same time with similar momenta, like many heads of cabbage on

the surface of a bouncing trampoline. If k of the atoms happen to be bound, then the probability that *none* of their N_k neighbors happen to have the right momentum to join the cluster is $(1-p)^{N_k}$, where p is the probability that a given neighbor does have the right momentum to join. Thus the probability that the k-cluster grows to size k+1 or larger by capturing some of its neighbors is $1-(1-p)^{N_k}$. This describes an emission-intact model of cluster formation. If these simple statistics describe the growth of clusters during correlated emission, then the yield of large k-clusters relative to that of dimers emitted during the process is

$$Y_k = (1-p)^{N_k}\{\Pi_{q=2}^{k-1}[1-(1-p)^{N_q}]\}Y_2. \tag{4.11}$$

We find that regardless of how we count the neighbors of a k-cluster of atoms on the surface of the target, $N_k \propto k$ so that $(1-p)^{N_k} \simeq \exp(-\alpha k)$. Because of the way in which the capture probability enters, equation 4.11 provides a single parameter fit, characterized by α, of this simple model to experimentally observed power laws. In figure 4.8 we have included the spectrum of k-clusters predicted by equation 4.11 under the assumptions $N_k = k$ and $p = 0.066$. For large clusters, the spectrum resulting from this correlated recombination assumption is seen to behave much more like a power law than the uncorrelated recombination prediction.

The assumption of recombination of correlated emissions also is appealing because it offers an explanation of the often observed similarity in the power spectra of all large clusters. Because, by assumption, all the atoms in a correlated emission are ejected with similar momenta, the energy per cluster atom is independent of cluster size, and the energy spectra for all cluster sizes should have roughly the same form. In this case the shape of the energy spectra is determined by the correlated process responsible for the ejection the large surface region from which the clusters recombine.

4.4 Conclusions

The results of our Molecular Dynamics simulations suggest that large events, though rare, are important in producing large clusters. We find that regardless of the event size, the vast majority of atoms are sputtered from within one atomic diameter of the surface of the liquid target, and from within a few atomic diameters of the ion impact site. Given this result, the recombination model we present here, generalized to consider the different number of particles sputtered during different events, adequately predicts the dependence of the production of small k-atom clusters during events which sputter a total of N atoms: $Y_k(N) \sim N^k$.

We find a correlation between the depth of origin of clusters (containing up to four atoms) and their size. We find that in the In-Ga targets, gallium is sputtered more easily from beneath the surface than is indium. Our results confirm the proposition of Lill *et al.*that the average indium concentration of k-clusters reflects their depths of origin. However, because of the preferential sputtering of gallium, the depth of origin for a cluster with high gallium content need not be as great as one would assume given the actual indium-gallium concentration profile of the target.

In the simulations, the energy distributions of gallium and indium sputtered from the In-Ga target asymptote to $E^{-1.5}$ and $E^{-2.0}$, respectively. Because the gallium is sputtered from beneath the surface, this suggests that atoms sputtered from deeper within the target are more energetic. The angular distribution of sputtered atoms, without regard to atomic species, roughly obeys $dN/d(\cos\theta) \sim \cos^{2.3}\theta$, while the angular distribution of the gallium is much more forwardly peaked than that of the indium because of the steering effects of atoms on the surface upon atoms being sputtered from below. We find that the uncorrelated recombination prediction for the angular distributions of k-clusters, $dY_k/d(\cos\theta) \sim \{dN/d(\cos\theta)\}^k$, is roughly satisfied by the small clusters ($k < 4$) we see here. However, the predictions for the energy spectra, $dY_k/dE \sim E\{E^{-1}dN/dE\}^k$, underestimate the number of high energy k-clusters seen in the simulation.

The yield of the small k-clusters seen during these simulations decays with a $k^{-8.1}$

power law; the rapid decay is probably due to the relatively weak cluster binding potentials of the two-body potentials used during the simulation.

The recombination of uncorrelated emissions has been shown to lead to an exponential decay of the yield of clusters. We have demonstrated how simple models of the recombination of correlated emissions may explain the oft experimentally observed power-law decay of the yield of large clusters, and how they may also explain the similarity between the energy spectra of different sized clusters.

Chapter 5 Using intra-cluster correlation to probe the range of surface hydrogen desorption by charged ions

5.1 Introduction

When a fast ion penetrates the surface of a target, a yield of desorbed particles results from ion-surface interactions (see figure 5.1 a). The yield of hydrogen ions, Y_{H^+}, is of particular interest because for a large range of incident ion charge, $q \in (2, 30+)$, measurements indicate that the desorbate yield has a simple dependence: $Y_{H^+} \propto q^{\delta}$, $\delta \simeq 2.7$ (see figure 5.2), where, strikingly, no dependence of the yield on incident ion velocity or nuclear charge is observed [35].

At present, no universally accepted model exists for the desorption mechanism responsible for these two seemingly related processes [38]. We too have no *a priori* model describing this q^{δ} law. Still, even without a firm understanding of the de sorption process, we find that we can determine the length scale of the desorption mechanism by studying the yield of *transmission* desorbate during cluster bombardment of thin films (see figure 5.1 b). A fast ion traveling through a thin foil suffers a succession of small angle deflections caused by collisions with the atoms in the solid. This results in a random walk in the plane normal to the direction of travel, and a spread of possible exit locations on the exit side of the foil. When a cluster of n ions penetrates a very thin foil, so that the spread of the cluster ion exit sites is smaller than the length scale of the desorption mechanism, the hydrogen ions on the exit surface desorb by a power law similar to that observed for charge induced desorption: $Y_{H^+} \propto n^{\delta}$; if the foil is thick enough that the ions have widely separated because of small angle deflections and ion-ion Coulomb repulsion, the desorption process takes

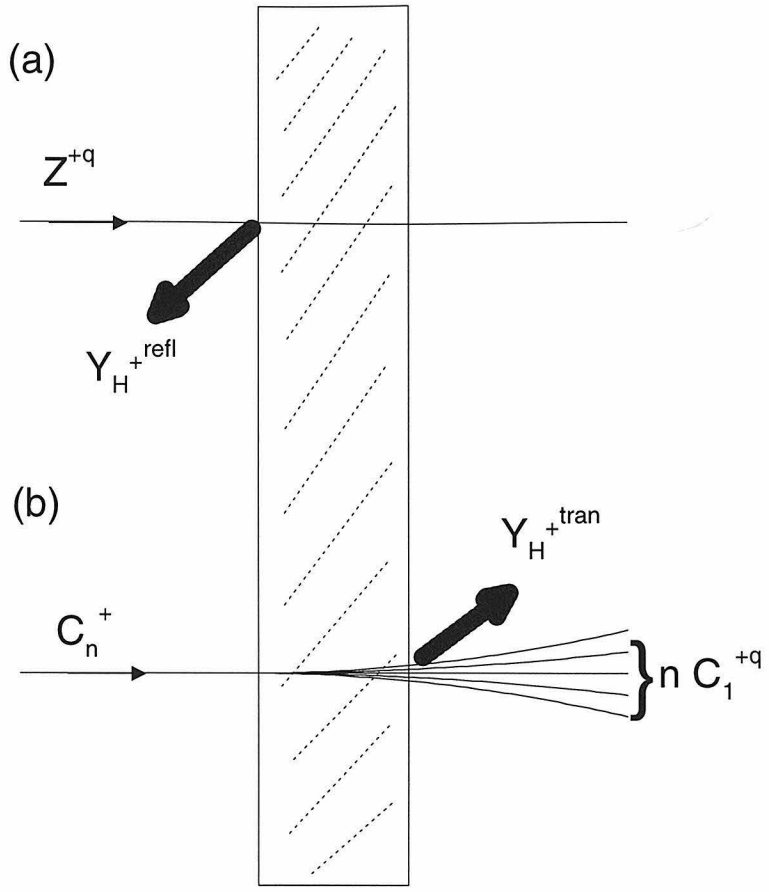

Figure 5.1: (a) A single ion of charge q desorbs H^+ ions from the surface of a target, $Y_{H^+} \propto q^{2.7}$ for large q. (b) A cluster of n atoms penetrating a thin foil target desorbs H^+ ions from the exit side of the target, $Y_{H^+} \propto n^{2.7}$ for thin targets, $Y_{H^+} \propto n$ for thick targets.

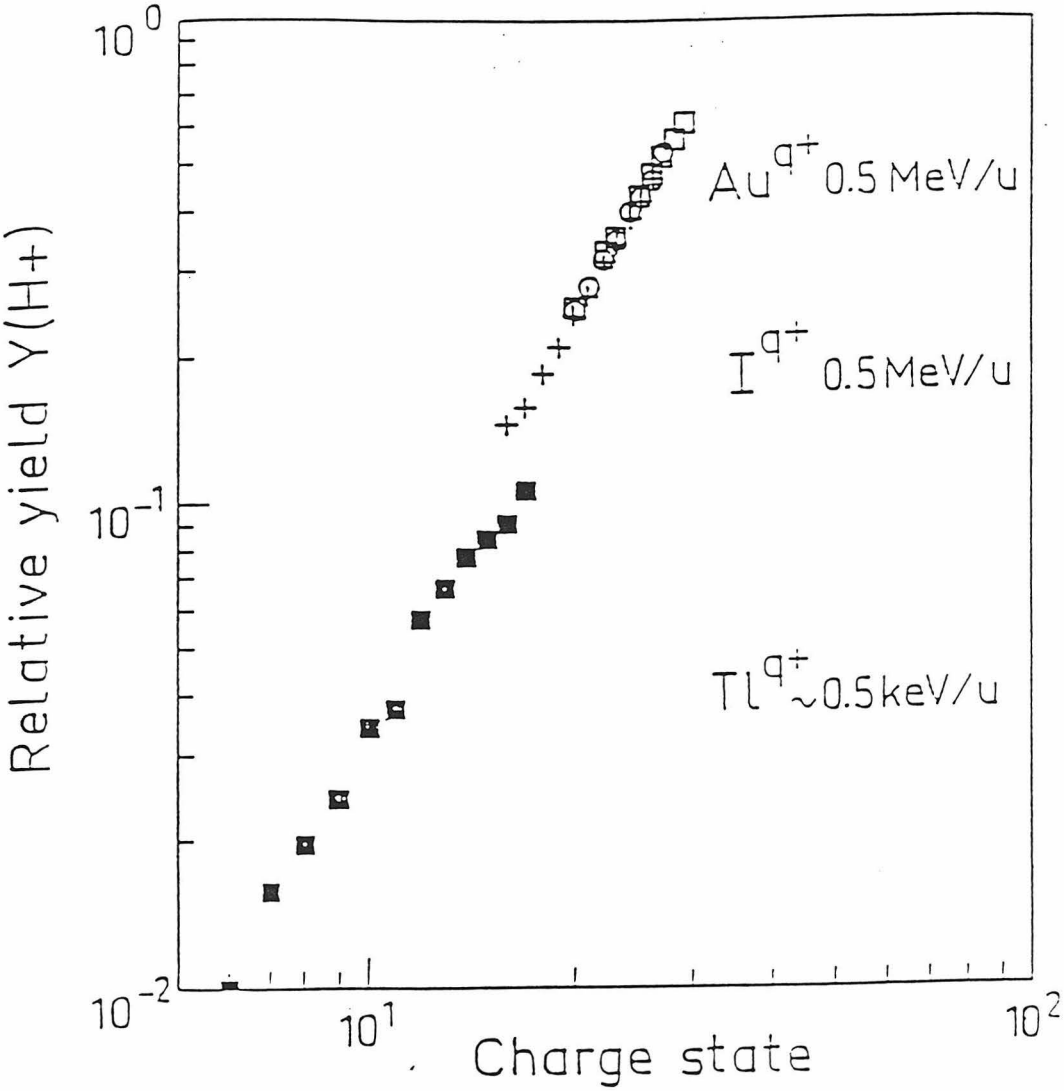

Figure 5.2: The $Y_{H^+} \propto q^{2.7}$ law for H^+ ion desorption by single ions of charge q is robust for $q > 2$ and is independent of ion species and energy [35]. See also figure 5.3.

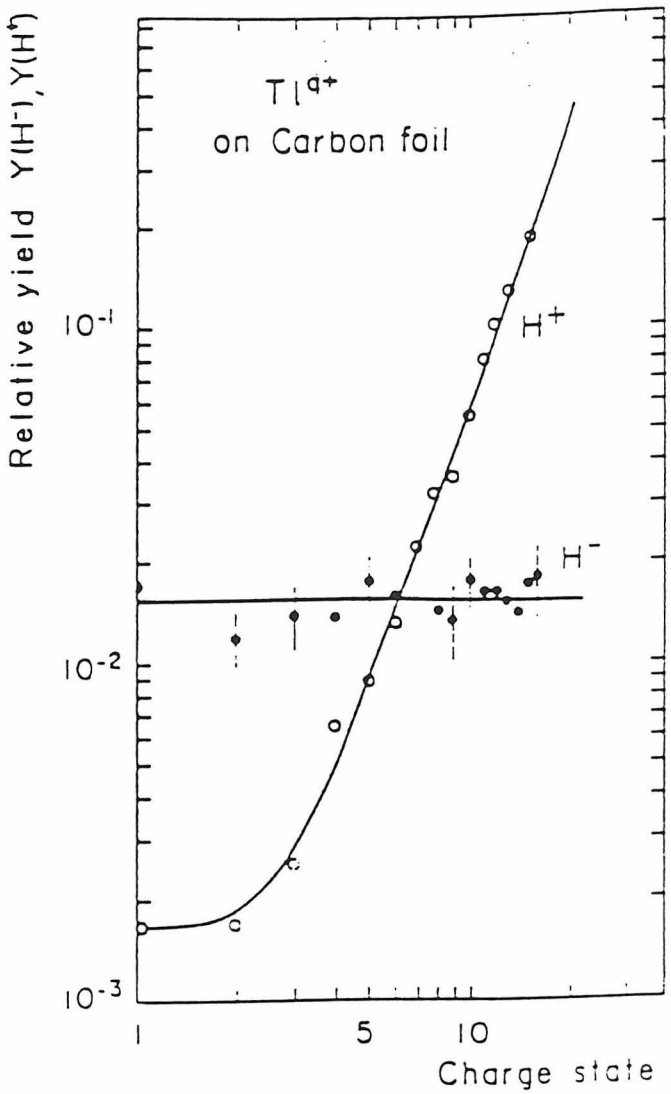

Figure 5.3: The $Y_{H^+} \propto q^{2.7}$ law for H^+ ion desorption fails for small ion charge [36].

place at n independent sites on the exit side of the foil, and $Y_{H^+} \propto n$ (see figure 5.4). If one could measure the inter-ion separation at the exit side of a foil of given thickness to determine the separation at which the n^δ yield became more n-like, then the range of the desorption mechanism (at least for the cluster effect) would be known. Of course, it is difficult to imagine how such a measurement could be made, so that to determine ion-ion exit surface correlations we appeal to simulation of the system.

The simulation of cluster penetration of moderately thick targets is a unique problem in that neither of the standard methods of ion induced target damage simulation are completely appropriate. Because the targets are relatively thick (hundreds of nano-meters), a Molecular Dynamics (MD) integration of the cluster penetration is very costly. Also, Binary Collision (BC) integration of the cluster trajectory is not possible because the ions in the cluster are co-moving and hence not in the BC regime. In order to avoid a costly full MD integration of the cluster target interaction while still retaining proper integration of the intra-cluster forces and the speed of a BC calculation, we have developed a hybrid algorithm which can predict the intra-cluster ion-ion correlations we require to determine the range of the H^+ desorption process.

5.2 Simulation Algorithm

For fast ions, the interactions between ion and target atoms are adequately described in the binary collision approximation (BCA). This is because the ion passes a target atom so quickly that the atom has little time to recoil into its neighbors. Binary collision codes such as TRIM and MARLOWE [1, 7] are widely available and can be used to calculate ion distributions at the exit side of a thin film. Because these codes can use an algorithm which employs pre-integrated scattering matrix elements, they are very fast. However, they cannot simulate the intra-cluster ion-ion interactions and so do not predict the proper exit-side ion distributions when several ions enter the target as a single tightly correlated cluster. Molecular dynamics codes, on the other hand, integrate the full equations of motion for all atoms, and properly handle both ion-atom and intra-cluster ion-ion interactions. For this reason, however, they are

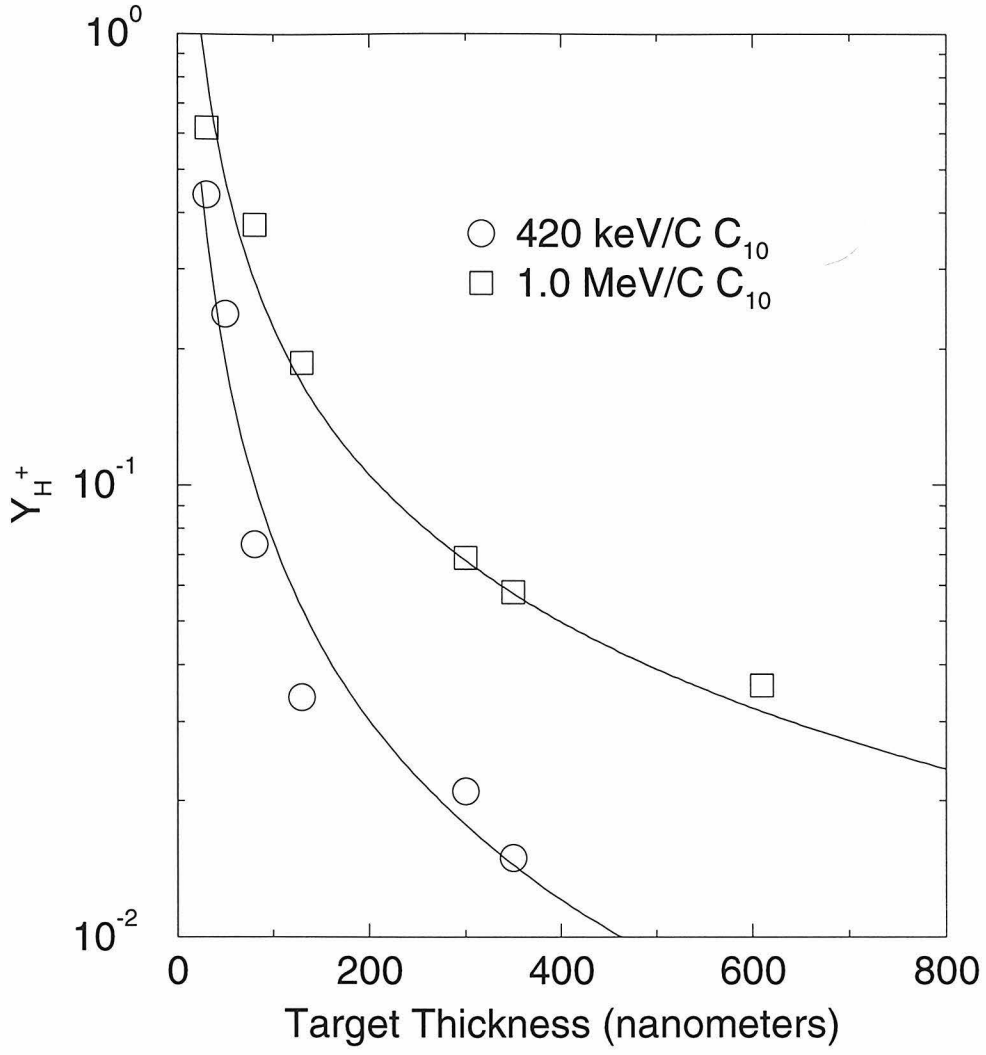

Figure 5.4: Observed transmission Y_{H^+} from 0.42 and 1.0 MeV/C clusters of C_{10} [37]. Lines are only included to guide the eye. Because the ions slow appreciably as the cluster travels through the thicker targets, one would expect to see a strong q dependence in the yield of H^+ ions; however, such a dependence is not observed.

very slow compared to the binary collision codes. For single ion penetration, they are strictly required only when the ion is relatively slow and the BCA is inappropriate.

For a fast cluster, one wishes for the best of each of the binary collision and molecular dynamics codes. One wants a speedy pre-integrated algorithm to handle the ion-atom collisions while retaining proper integration of the ion-ion interactions. Intuitively, this separation of interactions is sensible. A fast ion scattering from a stationary atom suffers only small position and momentum perturbations for all but the smallest of impact parameters. Thus, the initial gross evolution of the cluster is due to the Coulomb explosion: upon target penetration, valence electrons responsible for binding the cluster together are stripped and the cluster atoms begin to push apart. With this in mind, ion-atom collisions manifest themselves as relatively small random momentum impulses on top of the steadier ion-ion interactions. As the cluster expands, the ions decouple and their trajectories begin to evolve independently. We describe below a hybrid algorithm which permits the combination of binary ion-atom and molecular dynamic ion-ion integration of cluster ion trajectories.

We have developed two hybrid algorithms which are simple generalizations of the logic of TRIM and MARLOWE -type codes; these codes string together binary collisions. When an ion scatters from an atom, the momentum transfer is a function of the incident energy and impact parameter, and simply points the atom in a new direction with a slightly smaller momentum. In the impulse approximation, the ion follows a straight trajectory until reaching a turning point, whereupon the entire momentum transfer is applied, and the ion leaves on a new trajectory with a slightly changed momentum (see figure 5.5). We have two codes which use this approximation for ion-atom scattering while simultaneously integrating the ion-ion interactions exactly using a discrete time-step integrator.

The first version of this hybrid algorithm can follow the trajectories of several ions through a crystalline lattice. After an ion-atom collision, the positions and velocities $\{\vec{r}, \vec{v}\}$ of each ion in the cluster are considered to decide which of the ions in the cluster will suffer the next ion-atom collision. The time $\Delta t = \frac{\|\vec{r}_t - \vec{r}\|}{\|\vec{v}\|}$ to that next collision is determined (see figure 5.5). Standard MD methods are used to integrate the ions

forward in time by Δt under the ion-ion interactions; during this time ion-atom interactions are ignored. Then when the MD integrator reaches the turning point of the next ion-atom collision, the proper ion-atom momentum impulse is given to the particular ion which set Δt, the algorithm looks for the next ion-atom collision, and repeats. In this version of the code, the impact parameter of each ion-atom collision is known deterministically because the paths of the ions through a predetermined lattice are followed.

A second version of the algorithm treats amorphous targets and is slightly faster. The ion trajectories are integrated under the ion-ion interaction by standard methods, but the ions' positions relative to the lattice atoms do not need to be followed. Instead, because the target is assumed amorphous, an ion-atom binary collision is dealt to each ion every time it travels a unit length $a = \nu^{1/3}$; here ν is the unit volume of an atom in the solid. In this algorithm, the impact parameter for each ion-atom scattering event is chosen randomly from an appropriate distribution.

In both versions, electronic energy loss is easily included. Because we are interested in simulating the penetration of $\sim$MeV/ion clusters, electronic stopping is very important and must be included.

5.2.1 Integration Accuracy

Decoupling the ion-ion and ion-atom interactions seemingly is a poorly defined process. The true trajectories of ions interacting with each other and the atoms in the lattice are not the same as those they follow under the algorithm defined above. However, in the fast ion limit, the error in trajectory is sufficiently small that the difference is insignificant. Typically, as a fast ion travels forward by a lattice constant of length, there is only an infinitesimal perturbation to the straight line trajectory a free ion would have. An important point to be made is that the influence of the ion-ion interaction over this length scale is very weak. If we assume that the ion-ion interaction is Coulombic, then the displacement due to ion-ion interactions while the

ion travels forward by a single lattice constant is on the order of

$$\begin{aligned} \delta r|_a &\simeq \frac{1}{2}\frac{Z_1 Z_2 e^2 n}{mr^2}(\delta t)^2, \qquad \delta t \simeq a/v \\ &\simeq 0.004(\frac{Z_{ion}}{10})^2 \frac{MeV}{E}\frac{n}{10}(\frac{a}{r})^2 \mathring{A}, \end{aligned} \tag{5.1}$$

where E is the ion kinetic energy and r is the separation between ions in the cluster. Because the separation between ions will be on the order of the lattice constant or larger, we see that for MeV ions, the Coulomb explosion contributes only a slight perturbation (~0.01Å) to the trajectory of the ion over each lattice constant traversed. It is only because the ions travel forward many lattice constants while still within interaction range of one another that the Coulomb explosion has a noticeable effect.

Similarly, the error introduced by the impulse approximation to the ion-atom scattering trajectory is small for fast ions. If one assumes that the ion scatters from the atom through a Coulombic interaction, then the center-of-mass scattering angle satisfies $\tan\frac{\theta}{2} = 2b\epsilon/Z_{ion}Z_{atom}e^2 \equiv 1/x$ where ϵ is the center-of-mass energy (see figure 5.5). When the ion passes the point of intranuclear separation $r = r_0$, dr/dt=0 so that energy conservation $(\frac{1}{2}\mu(\frac{dr}{dt})^2 + \frac{l^2}{2\mu r^2} + \frac{Z_{ion}Z_{atom}e^2}{r} = \epsilon$, where $l = b\sqrt{2\mu\epsilon})$ implies $b/r_0 = -x + \sqrt{x^2+1}$. From figure 5.5 $b/r_t = \sin\phi = 1/\sqrt{x^2+1}$. The greatest deviation of the impulse trajectory from the true trajectory occurs at $r = r_t$, so:

$$\begin{aligned} \delta r_{max} &= r_o - r_t \sim \frac{Z_{ion}Z_{atom}e^2}{2\epsilon} \\ &\sim 0.001(\frac{Z_{ion}Z_{atom}}{100}\frac{MeV}{2\epsilon})\mathring{A}. \end{aligned} \tag{5.2}$$

Note that this limit on the ion trajectory error is independent of the collision impact parameter.

Given these two crude limits on the trajectory errors inherent in our algorithm, one can estimate when it should begin to fail. Demanding that both δr remain smaller than some fraction of an Ångstrom suggests that the algorithm should be reliable for the integration of trajectories of ~ MeV/ion clusters. In fact, because we have used the rather stiff Coulomb interaction to set these limits, they are very conservative.

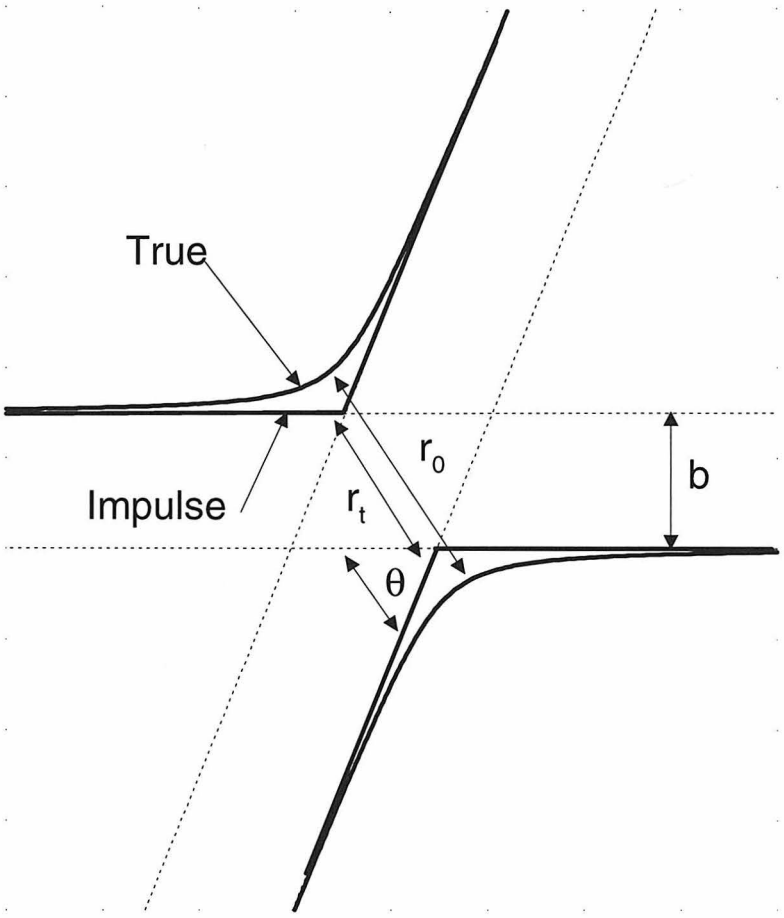

Figure 5.5: Center-of-mass collision partner trajectories in the impulse approximation.

5.3 Simulation Results: $C_n \rightarrow$ Amorphous Carbon

Using the amorphous target version of the code described above, we have simulated the penetration of amorphous carbon by 0.42 and 1.0 MeV/C C_{10} and 2.0 MeV/C C_5 clusters. During the simulations, the binary-collision ion-atom scattering has been described by the Magic Formula proposed by Biersack and Haggmark [1]. This Magic Formula is an approximation to the center-of-mass momentum transfer as a function of reduced center-of-mass energy and impact parameter. The Formula is described in detail in *The Stopping and Range of Ions in Solids* and is the basis of the Monte Carlo code TRIM [1].

The shapes of C_5 and C_{10} clusters are not experimentally known. If the clusters are formed with a significant amount of internal energy, then they are likely bound together as chains of atoms. To create clusters for target bombardment during the simulations, we placed carbon atoms in patterns generated by self-avoiding random walks of step lengths equal to the bond length in amorphous carbon [39] (see figure 5.6). Once a cluster strikes the target, the valence electrons which bind the cluster together are stripped and the cluster atoms, now ions, begin to repel each other through the Coulomb interaction. Because there are few occupied electronic states in carbon, we have assumed that charge equilibration occurs rapidly, in the first several layers of the target. To first order, the effective ion charge is determined by considering that all bound electronic states with Bohr velocity less than that of the ion in the solid are stripped away. We have used a slightly more refined approximation suggested by Brandt [40] to determine the effective ion charge. The interaction of ions co-moving and with velocities comparable to the Fermi velocity of the target electrons is itself a new and interesting problem. It is unclear that conduction-electron screening of the ion charge will be as effective for a very fast ion as it is for a stationary charge. We have performed simulations in which the intra-cluster potentials have been taken to be unshielded Coulomb with the effective charges given by the Brandt theory, and also simulations in which the intra-cluster interactions have been ignored completely. These two limits reflect no shielding and perfect shielding, respectively, and place

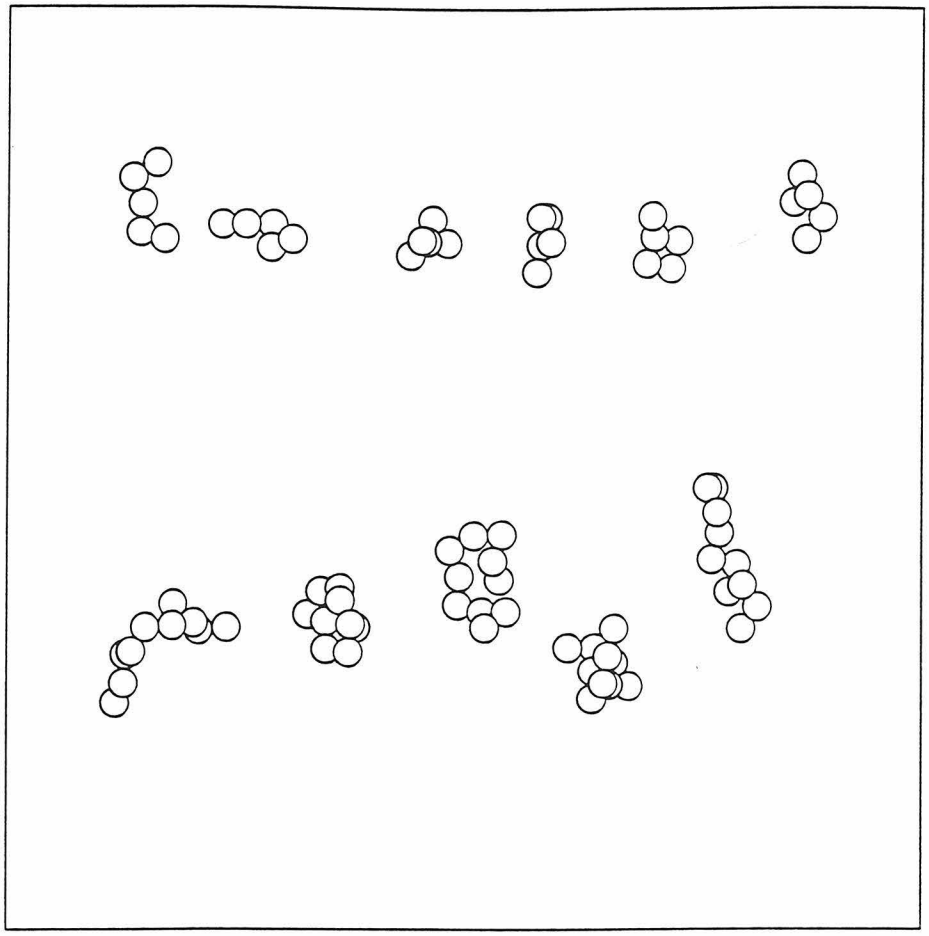

Figure 5.6: Examples of C_5 and C_{10} chain-like clusters generated by self-avoiding random walks.

limits on the real intra-cluster interaction.

The evolution of the ions in each cluster was followed as they penetrated 900 nm into amorphous target of amorphous carbon. The position and travel time of each atom in the cluster was recorded after it penetrated 25, 32.5, 82, 140, 300, 350, 615 and 900 nm into the target, allowing us to predict exit-side ion-ion correlations for several foil thicknesses from a minimal number of simulations.

A clear demonstration of these simulations is that for thick targets, the scattering of the cluster ions from the lattice atoms is the dominant effect responsible for the spread of the cluster ions upon exit (see figure 5.7, 5.8, and 5.9). For these thicker targets, the spread of exit sites is independent of whether or not the Coulomb explosion of the cluster is included. For thin targets, and relatively fast clusters, the Coulomb explosion may be important. In fact, if the desorption mechanism were better understood, one could hope to use it to determine the strength of the Coulomb explosion and hence the interaction between fast co-moving ions in a solid.

5.3.1 Hydrogen Desorption from Cluster Exit

The observation that the exit surface hydrogen desorption yield evolves smoothly from $Y_{H^+} \sim n^\delta$ to $Y_{H^+} \sim n$ as the n exit sites of ions in an n-cluster become decorrelated suggest that H^+ ions desorb from the surface if they are either very close to a single ion exit site or in a region about which many cluster ions exit. We can define an effective "desorption area" which is a function of the ion exit sites and an additional single length scale:

$$\begin{aligned} A_\infty = & \int d^2r\Theta(\textstyle\sum_{i=1}^{n} \frac{1}{|r-r_i|^{2/\delta}} - \frac{1}{r_c^{2/\delta}}) & \\ \sim & \quad \pi r_c^2 n^\delta, & (\Delta r_{ions})^2 < r_c^2 \\ \sim & \quad \pi r_c^2 n, & (\Delta r_{ions})^2 > r_c^2, \end{aligned} \tag{5.3}$$

Where $\{r_i\}_{i=1}^n$ are the exit sites of the ions in the cluster, Δr_{ions} is the spread of the cluster ion exit sites, and $\Theta(x)$ is the Heaviside function, which is 1 if $x > 0$ and

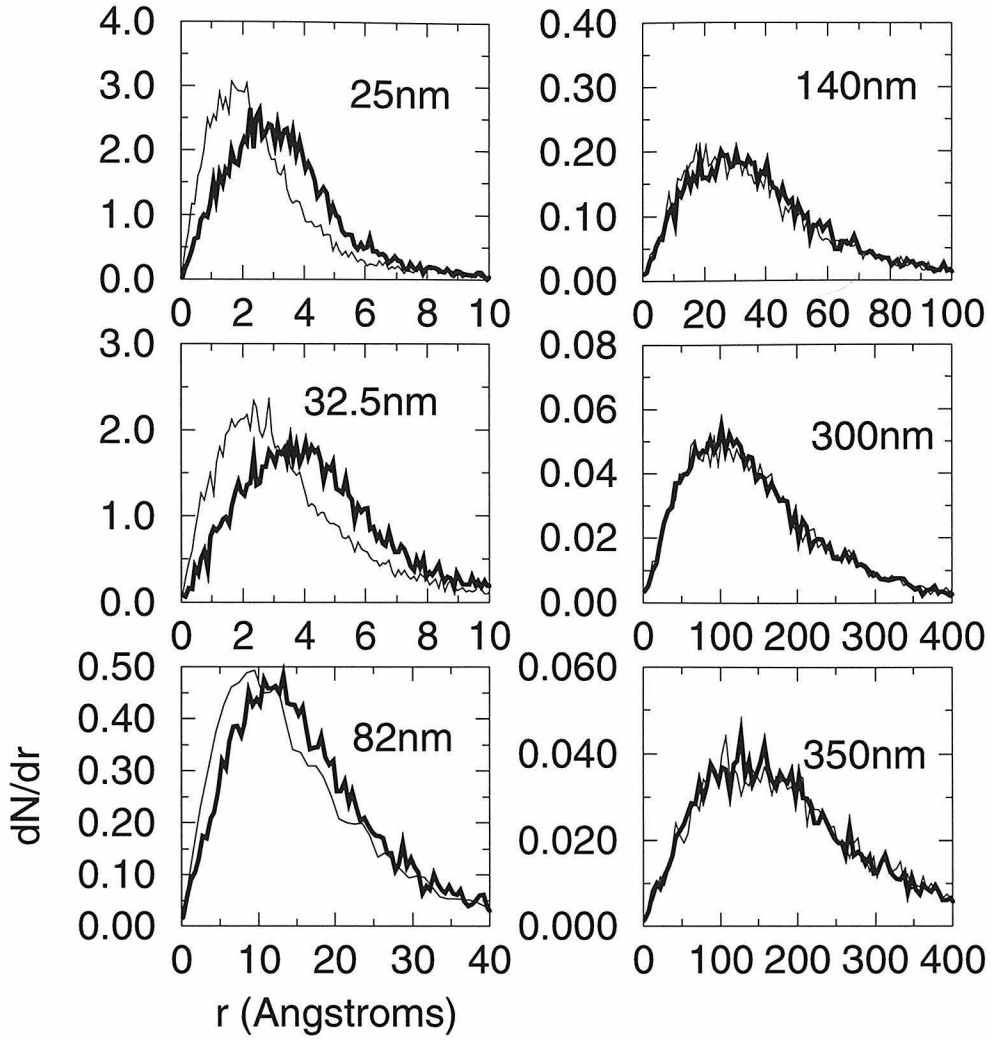

Figure 5.7: Distribution of ions at the exit side of targets of various thicknesses. Thick lines are the distribution predicted if one assumes an unshielded Coulomb explosion using effective ion charges according to Brandt (see text). Thin lines are distributions predicted if the intra-cluster interactions are ignored. Distances in each panel are target thicknesses. The density as a function of radial distance from the straight line trajectory is shown for C_{10} clusters of incident energy 420 keV/C.

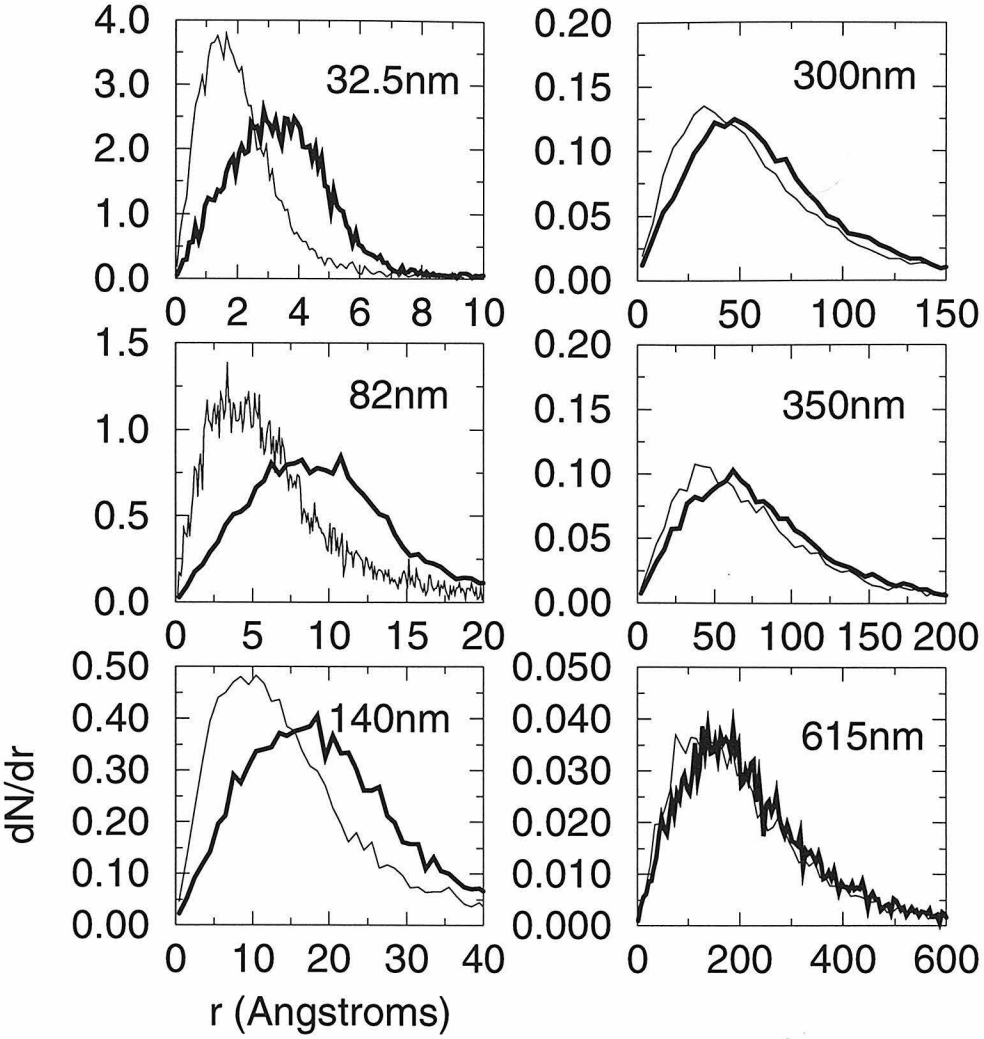

Figure 5.8: 1.0 MeV/C C_{10}. See caption of figure 5.7.

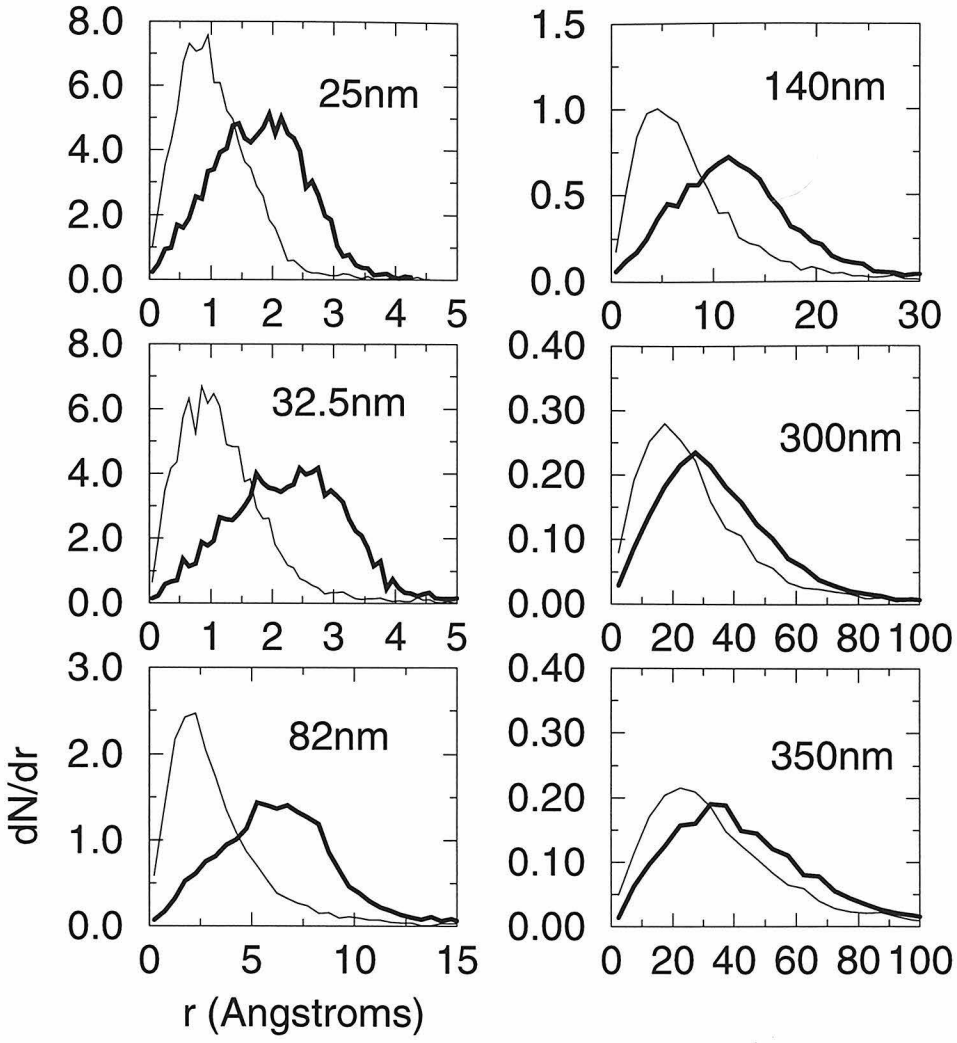

Figure 5.9: 2.0 MeV/C C_5. See caption of figure 5.7.

0 otherwise. Physically, we have in mind that desorption is driven by an additive 'desorption potential' which decays as $1/r^{2/\delta}$ from the site of ion exit and that if a hydrogen is found at a point where the total desorption potential is greater than some critical value, namely $1/r_c^{2/\delta}$, then it will be desorbed; the range of the desorption potential is simply r_c. Equation 5.3 represents the area of the exit surface on which the desorption potential is greater than $1/r_c^{2/\delta}$, the yield of desorbed H^+ should be that area times the density of hydrogen adsorbed to the surface, ρ_H, and the efficiency, f, with which H^+ escapes the surface without being neutralized, *i.e.*, $Y_{H^+} = f\rho_H A_\infty(r_c)$. While equation 5.3 may appear arbitrary, it only contains two implicit assumptions. The first is that the strength of the desorption mechanism is additive; the rather strange decay of the postulated desorption potential is required by the experimental observation of the correlated and uncorrelated limits. The critical value of the desorption potential has been written to display its relationship to the range of the potential. The second assumption is that the lifetime of the desorption mechanism is long compared to the time the cluster takes to pass the surface. If two cluster ions exit nearby the same hydrogen adsorption site but the second passes much later than the first, adsorption will not occur if the reaction of the bond adsorbing the hydrogen to the passing of the first ion has subsided sufficiently before the second ion passes. However, even the slowest clusters we consider, 4.2 MeV/C incident C_{10} clusters exiting from a 300nm foil, have a spread in exit times of only a few femtoseconds (see table 5.1). Thus, because the relaxation lifetime is likely at least of order a femtosecond, we feel the infinite lifetime approximation is acceptable.

Given the hopefully minimal assumptions which have gone into the above desorption model, we can extract the range of the desorption potential by choosing r_c so that the evaluation of equation 5.3 with the exit positions $\{r_i\}$ of the 1.0 MeV/C C_{10} cluster ions predicted by the simulations yields the proper transition of $Y_{H^+} \propto 10^{2.7} \rightarrow 10$ as the target thicknesses range from 32.5 to 300 nm. Evaluating equation 5.3 for an ensemble of cluster exit sites over a range of the critical desorption potential $1/r_c^{2/\delta}$ is a rather nasty, time consuming process. For the 32.5, 82, 140, and 300 nm thick targets each, we have evaluated A_∞ for an ensemble of 50 cluster exit distributions.

The area on which the additive desorption potential is greater than $1/r_c^{2/\delta}$ for the simulation distributions has been averaged over the ensemble and is presented in figure 5.10. All curves are bounded above by the large-r_c limit, $A \simeq \pi r_c^2 10^\delta$, and below by the small-r_c limit, $A \simeq \pi r_c^2 10$ (see figure 5.10). The first thing to notice is that for the transition of $Y_{32.5nm} \sim 10^\delta \rightarrow Y_{300nm} \sim 10$ to be possible, we require 0.1Å$< r_c <$ 3Å, otherwise all curves are on the $Y \sim 10^{2.7}$ or $Y \sim 10$ envelopes. The best fit to the relative observed yields with the smallest spread in the critical value of the desorption potential occurs for $r_c \simeq 0.6$Å. This fit requires that the absolute yield of desorbed hydrogen ions be scaled by a constant factor $f\rho_H \sim 1/1000\text{Å}^2$ (see figures 5.11 and 5.12). A similar procedure used to fit the 0.42 MeV/C C_{10} data yields similar values for r_c and $f\rho_H$ (see figures 5.13 and 5.14).

We learn two things from this fitting process. First, the range of the desorption process is of order $r_c \simeq 0.6$Å; this is remarkably similar to the charge radius of the 2s and 2p orbitals in the carbon ion (we have more to say about this momentarily). Second, the product of the adsorbed hydrogen density and the escape efficiency is $f\rho_H \simeq 1/1000\text{Å}^2$. If we assume the escape efficiency is of order 1% – a typical ion to neutral fraction, then we find that the density of surface hydrogen is $\rho_H \simeq 1/(\text{few Å})^2$, an appealing and reasonable result.

5.4 Discussion

Previous investigations of single ion desorption have suggested that the length scale of the hydrogen desorption process when it is driven by a single ion of charge q is on the order of $\sim$ 10 Å. Hence, the correlation length we require to fit the cluster desorption data is surprisingly small. However, the two proposed correlation lengths are not in contradiction, and can be explained in a unified manner through the concept of the desorption potential introduced above to quantify the correlation of the exit side cluster ions.

There are two important observations to be made about H^+ desorption yields caused by single ion and cluster penetration. First, the exit side cluster desorption

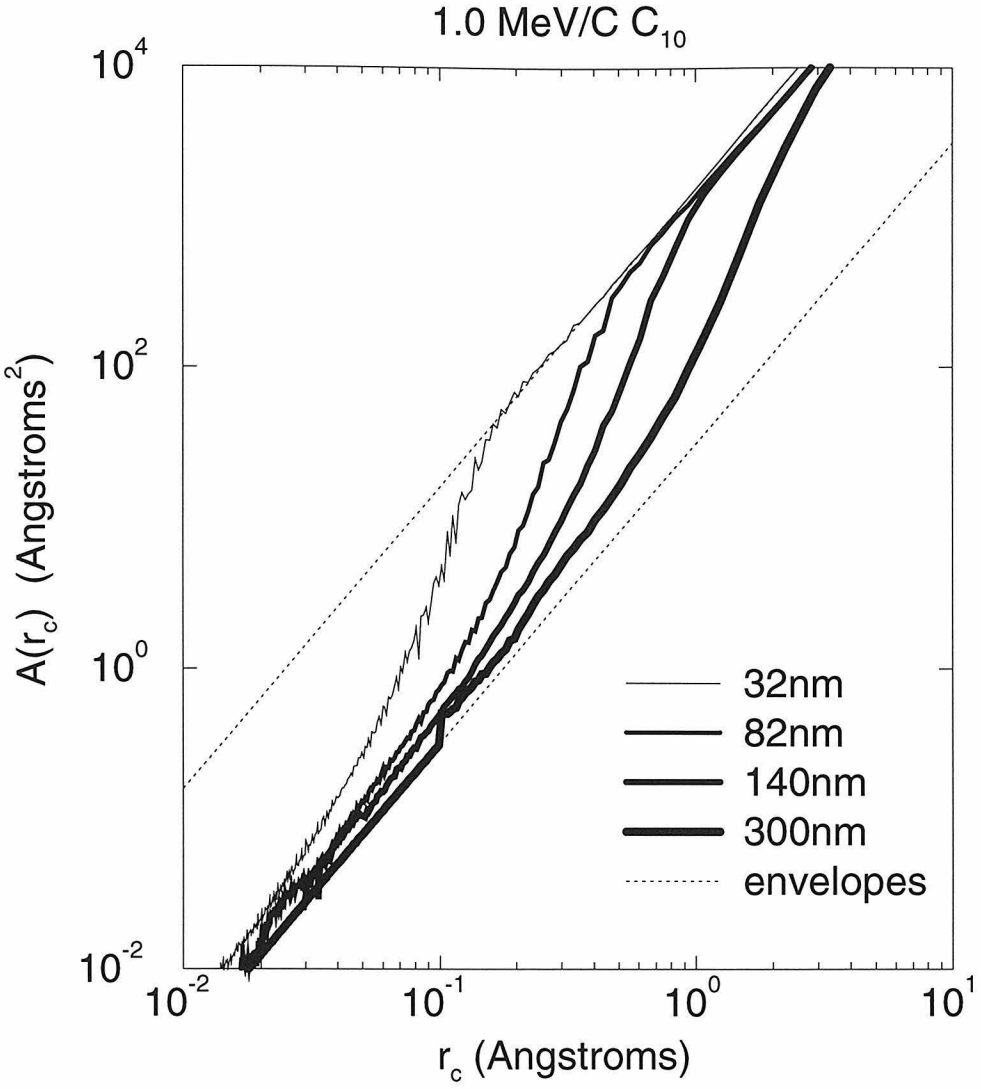

Figure 5.10: Exit side desorption area A_0 as a function of target thickness and r_c for 1.0 MeV/C C_{10} clusters. The transition from $\sim$ 10 to $\sim 10^{2.7}$ behavior is seen to occur for 0.1Å$< r_c <$ 3Å.

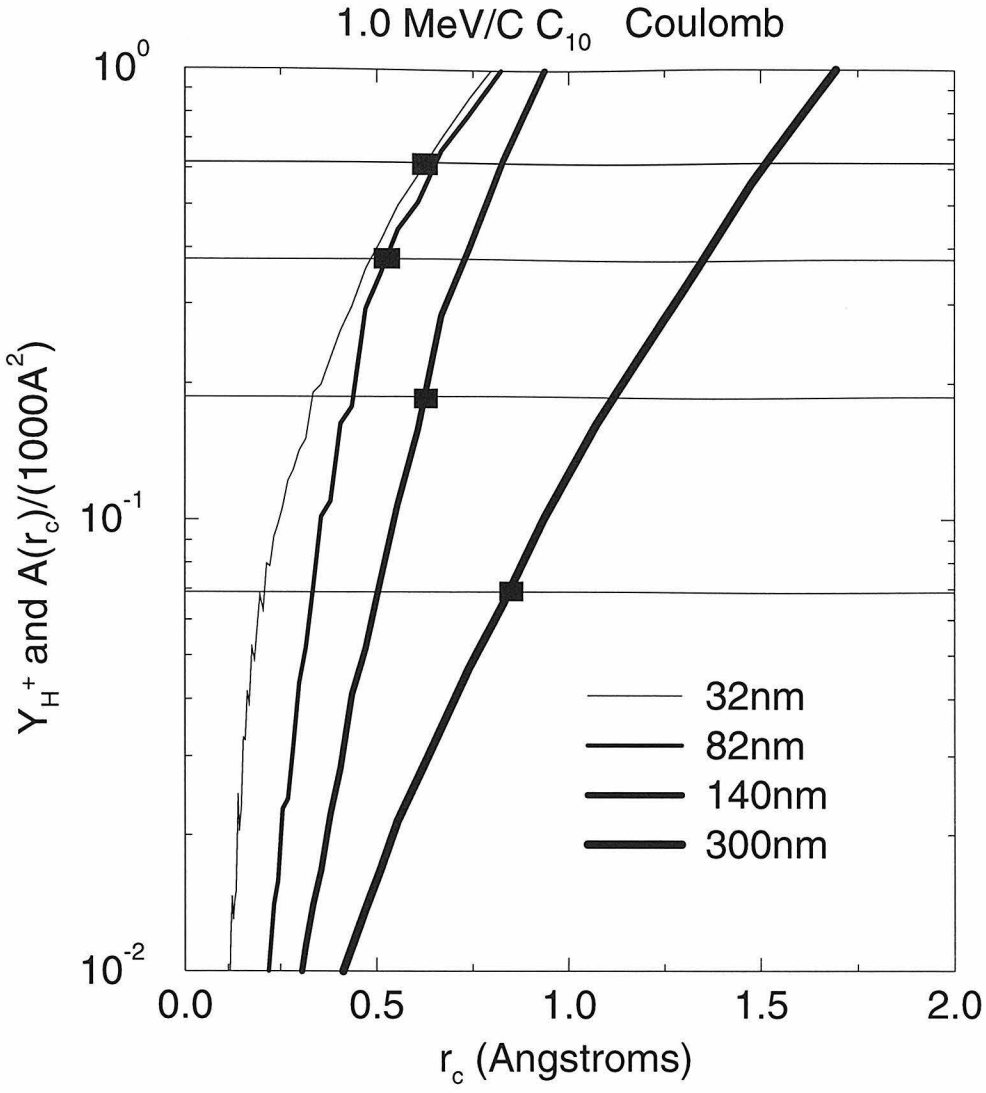

Figure 5.11: Exit side desorption area A_0 as a function of target thickness and r_c for 1.0 MeV/C C_{10} clusters with Coulomb explosion. The best fit of the model to observed yields occurs for $r_c \sim 0.6$Å. (See dark rectangles on each curve.) Areas have been scaled by a factor of $f\rho_H \simeq 1/(1000\text{Å}^2)$ to match the absolute scale of the observed H^+ yields.

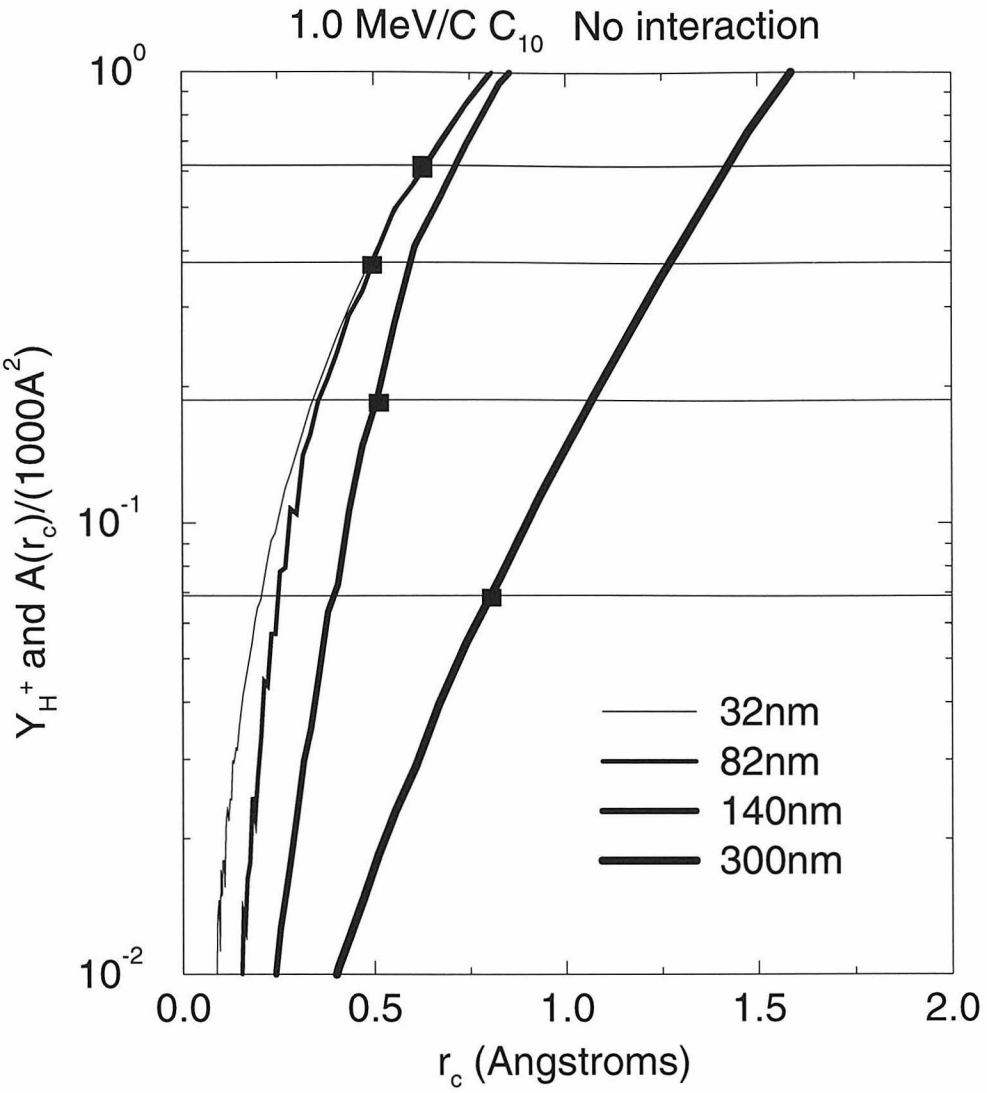

Figure 5.12: Same as figure 5.11 except the intra-cluster interactions have been turned off.

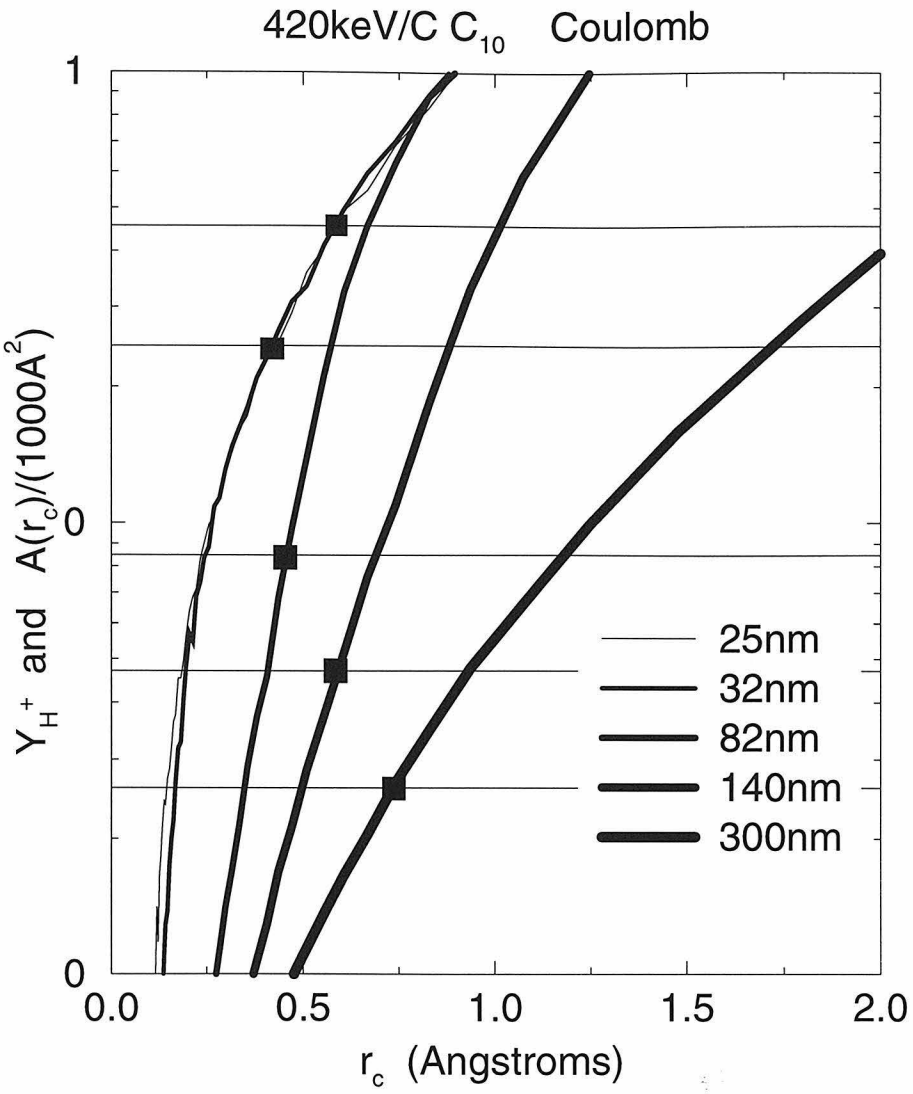

Figure 5.13: Exit side desorption area A_0 as a function of target thickness and r_c for 0.42 MeV/C C_{10} clusters. Similar to the 1.0 MeV/C data, a good fit of the model to observed yields occurs for $r_c \sim 0.6$Å and $f\rho_H \simeq 1/(1000\text{Å}^2)$.

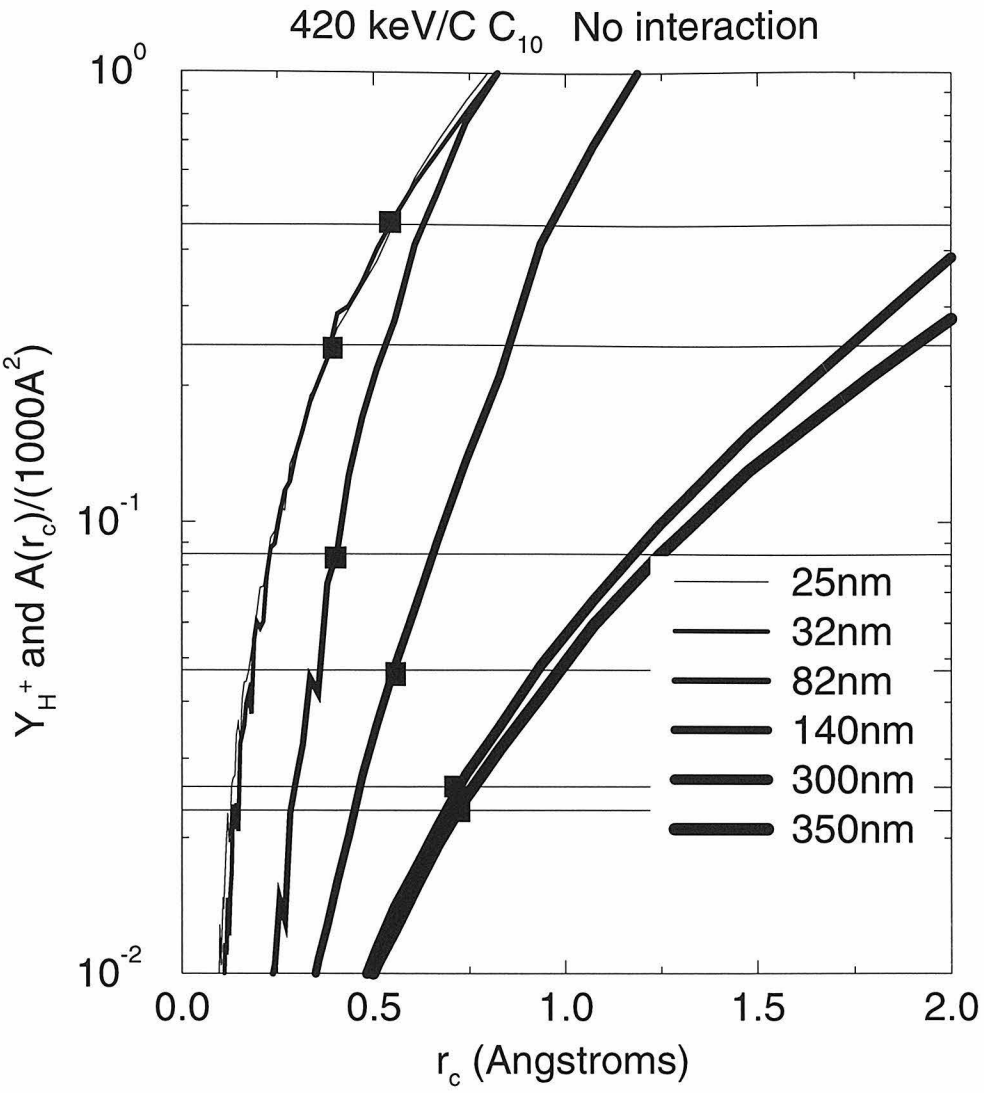

Figure 5.14: Same as figure 5.13 except the intra-cluster interactions have been turned off.

yields do not display q^δ charge dependence (see figure 5.4). As the cluster travels through thicker and thicker targets, the exit velocities of the ions decrease, and hence their effective charges also decrease. A 1MeV/C cluster of 10 carbon atoms exits a 32.5 nm target with almost 993 keV/C, typical models for the effective charge of a carbon atom with this energy in a carbon target predict $q \simeq 2.5$ [40, 1]. After the cluster travels through 900nm of target, the energy drops to about 150 keV/C and the charge to $q \simeq 1.0$. Thus, from the charge drop alone, the yield of desorbed hydrogen should fall by a factor of $\sim (1.0/2.5)^{2.7} \simeq 0.08$. That this charge dependence is not present is evident in both the exit side C_{10} and C_1 H^+ desorption yields. Second, for reflection desorption from q-charged incident Thallium ions, the apparently robust $Y_{H^+} \propto q^\delta$ law fails for $q \leq 2$ (see figure 5.2). This failure of $Y_{H^+} \sim q^\delta$ seems consistent with the lack of strong q dependence in the exit side cluster desorption because the exit charges of the cluster ion are also of order or less than 2.

The lack of q dependence for low charge ions can be explained by assuming that the desorption range for the charge has shrunk to the scale of the ion itself. For a single ion of large charge q, we know $Y_{H^+} \propto q^\delta$ and expect $Y_{H^+} \propto \pi r^2_{desorption}$ where $r_{desorption}$ is the range of the desorption mechanism, thus $r_{desorption} \sim q^{\delta/2}$. With the desorption potential model in mind, we define $\phi(q,r) = \frac{q}{q_0}\frac{1}{r^{2/\delta}}$; then, just as in the case for cluster desorption, if $\phi(q,r) > 1/r_c^{2/\delta}$ at a site r from the charge q, then any hydrogen adsorbed to the site will be desorbed. If r is actually inside the charge radius of the ion, then the effective charge $q_{eff}(r) \in (q, Z)$ (see figure 5.15) seen by the site will be larger than the ion charge. This implies that for all ions, regardless of charge, there will be a minimum desorption area. Scaling of the desorption range for $r_{desorption}$ greater than the charge radius of an ion demands $r_{desorption} \simeq r_0(q/q_0)^{\delta/2}$. With the Thallium data in mind, we note that the scaling fails for $q \simeq 2$ and, because the charge radius of a Thallium ion is about 1Å, can write $r_{desorption} \simeq 1\text{Å}(q/2)^{\delta/2}$. Because the exit charge of the C ions from the $\sim$ MeV/C $C_{10} \rightarrow$ Carbon (amorphous foil) is of order 2 or smaller, this is consistent with our claim that the desorption range required to correlate properly the cluster exit sites is independent of ion charge and is of order $r_c \simeq 0.6$Å. For ions with larger charge, the desorption radius is proportionately larger,

for example, if $q = 10$ then $r_{desorption} \simeq 1\text{Å}(10/2)^{\delta/2} \simeq 9\text{Å}$, which is consistent with previous claims that the desorption process must have a range of $\sim 10\text{Å}$.

To generalize the model for the desorption area to include both charge desorption and the charge radius effect, we should write:

$$A_\infty(q) = \int d^2r\Theta(\sum_{i=1}^{n} \frac{q_{eff}(r - r_i)}{|r - r_i|^{2/\delta}} - \frac{q_0}{r_c^{2/\delta}}), \tag{5.4}$$

where $\frac{q_0}{r_c^{2/\delta}} \sim 3$ and $q_{eff}(r - r_i)$ is as in figure 5.15. We feel that indiscriminate application of this rather crude model should be avoided until a better understanding of the desorption process is acquired. We have only used it to demonstrate that, for clusters of ions of very small charge, the desorption range required for correlations to be important is of order the ionic radii. This lower limit on the desorption range agrees with that required to explain the single ion failure of the q^δ law at small q.

The mechanism of desorption from positions far from an ion exit site is probably different from that which occurs at a site which is within the ion charge radius. However, if one could restrict the application of the above model to clusters of ions each of charge great enough that their desorption radii $r_{desorption} \simeq 0.5\text{Å}q^{\delta/2}$ are larger than their charge radii, then equation 5.4 has a good chance of making accurate predictions of the cluster desorption area.

Two issues are left open in this investigation. First, what is the lifetime of the desorption mechanism? We have assumed that it is long enough that the 'stirring' introduced to the adsorption bond by the foremost ions in the cluster does not decay before the hindmost ions pass. For all clusters and target thicknesses considered, except maybe the 4.2MeV/C C_{10} clusters at 300nm of thickness, the cluster ion exit times are are sufficiently bunched that this assumption is probably justified (see table 5.4). The second issue is that of the strength of the interactions between the co-moving cluster ions. Simulations show that for a 42 MeV C_{10} cluster penetrating an amorphous carbon foil, lattice scattering of the cluster ions dominates even an unshielded Coulomb explosion. Coulomb explosion is apparently more important for the 10 MeV C_{10} clusters, but these ions are moving too slowly to have a large

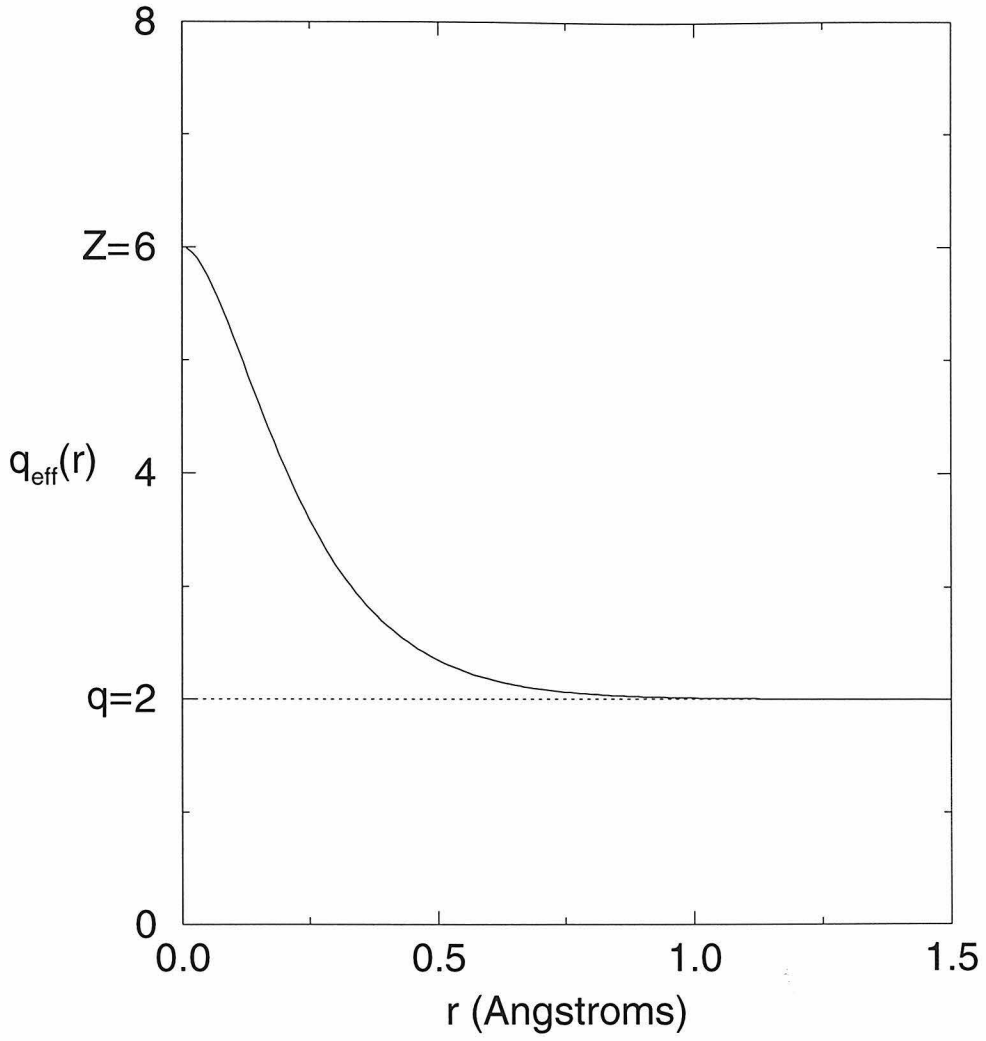

Figure 5.15: Charge contained in a sphere of radius r about an ion with nuclear charge $Z = 6$ and ionic charge $q = 2$. See reference [40] for more details.

	25nm	32nm	82nm	140nm	300nm
420keV/C C_{10}	0.66 fs	1.0 fs	1.46 fs	3.6 fs	11.2 fs
1.0MeV/C C_{10}	0.06	0.08	0.57	1.26	1.59
2.0MeV/C C_5	0.03	0.03	0.10	0.18	3.63

Table 5.1: Standard deviations of exit time distributions for 420 keV/C and 1.0 MeV/C C_{10}, and 2.0 MeV/C C_5 clusters from targets of varying thickness. Spreads about the average exit times are less than a few femtoseconds in all cases except for the 420 keV/C C_{10} clusters leaving the 300nm target.

enough charge that the desorption radius is larger than the charge radius, so that the reliability of the desorption model is uncertain. On the other hand, the exit side distributions of 2.0 MeV/C C_5 clusters show a strong dependence on the strength of their interaction, and their velocity is fast enough that they have a relatively large effective charge (approximately $q \simeq 3$); hence, one could hope that their desorption radii are larger than their charge radii. Given a reliable model relating cluster induced desorption to cluster correlations (we modestly propose equation 5.4), measurements of hydrogen desorption could be used to determine how effectively co-moving ions are shielded from one another as they travel through the target: for thin targets, effective shielding implies good correlation and a larger, more $(nq)^{\delta}$-like H^+ yield; strong Coulomb explosion implies a more $n(q)^{\delta}$-like H^+ yield. That is, measurements of Y_{H^+} imply Δr for the cluster exit positions, and Δr indirectly implies the strength of the Coulomb explosion. Such a determination of Δr from Y_{H^+} can be made by assuming that the cluster explodes in a roughly self-similar manner; then the absolute scale of the exit pattern, Δr, can be factored out of the exit positions of the cluster: $\{r_i \simeq \Delta r \cdot x_i\}_{i=1}^{n}$, where $(\Delta r)^2 \equiv \langle r^2 \rangle - \langle r \rangle^2$ and $\langle x^2 \rangle - \langle x \rangle^2 \simeq 1$. Then, when $r_q > r_{ion}$ equation 5.4 can be scaled to a universal function of $r_q \equiv r_c(q/q_0)^{\delta/2}$ and the cluster spot size Δr:

$$\begin{aligned} A_\infty &= \int d^2r \Theta\Big(\sum_{i=1}^{n} \frac{q}{|r - r_i|^{2/\delta}} - \frac{q_0}{r_c^{2/\delta}}\Big) \\ &\simeq (\Delta r)^2 \int d^2x \Theta\Big(\sum_{i=1}^{n} \frac{1}{|x - x_i|^{2/\delta}} - \Big(\frac{\Delta r}{r_q}\Big)^{2/\delta}\Big) \\ &\equiv \pi r_q^2 a_n(r_q/\Delta r). \end{aligned} \tag{5.5}$$

Scaling of the $n = 5$ exit side desorption areas for target thicknesses 25, 32.5, 82, 140, and 300 nm to the function $a_5(r_q/\Delta r)$ is shown in figure 5.16 and seen to be universal for the thinner targets.

5.5 Conclusions

We have developed an efficient integrator which can calculate the evolution of fast clusters of ions traveling through matter and used it to predict intra-cluster correlation as the cluster travels through up to $\sim$ micron thick targets.

We have developed a crude numerical model to describe ion and cluster induced desorption of hydrogen from target surface. By assuming an additive desorption potential which decays with distance from the exit site of each ion, it provides a unified description of hydrogen desorption caused both by single ions of small and large charge q, and by weakly and strongly correlated clusters of ions. We find that the range of the desorption mechanism is at least the size of the ion and scales roughly as $r_{desorption} \simeq 0.5\mathring{A}q^{\delta/2}$, $\delta \simeq 2.7$, when the ion charge is large.

For fast clusters penetrating thin targets, our simulations demonstrate that if the Coulomb repulsion of the cluster ions is unshielded, it provides the dominant contribution to the spread of cluster ion exit sites. The effectiveness of electronic shielding between these fast co-moving ions is not clear at present. However, because hydrogen desorption from cluster exit-side surface penetration is strongly dependent on the spread of exit sites, and this spread depends on the strength of the Coulomb explosion, it may be possible to probe the strength of the intra-cluster shielding by measurements of the hydrogen desorption yield.

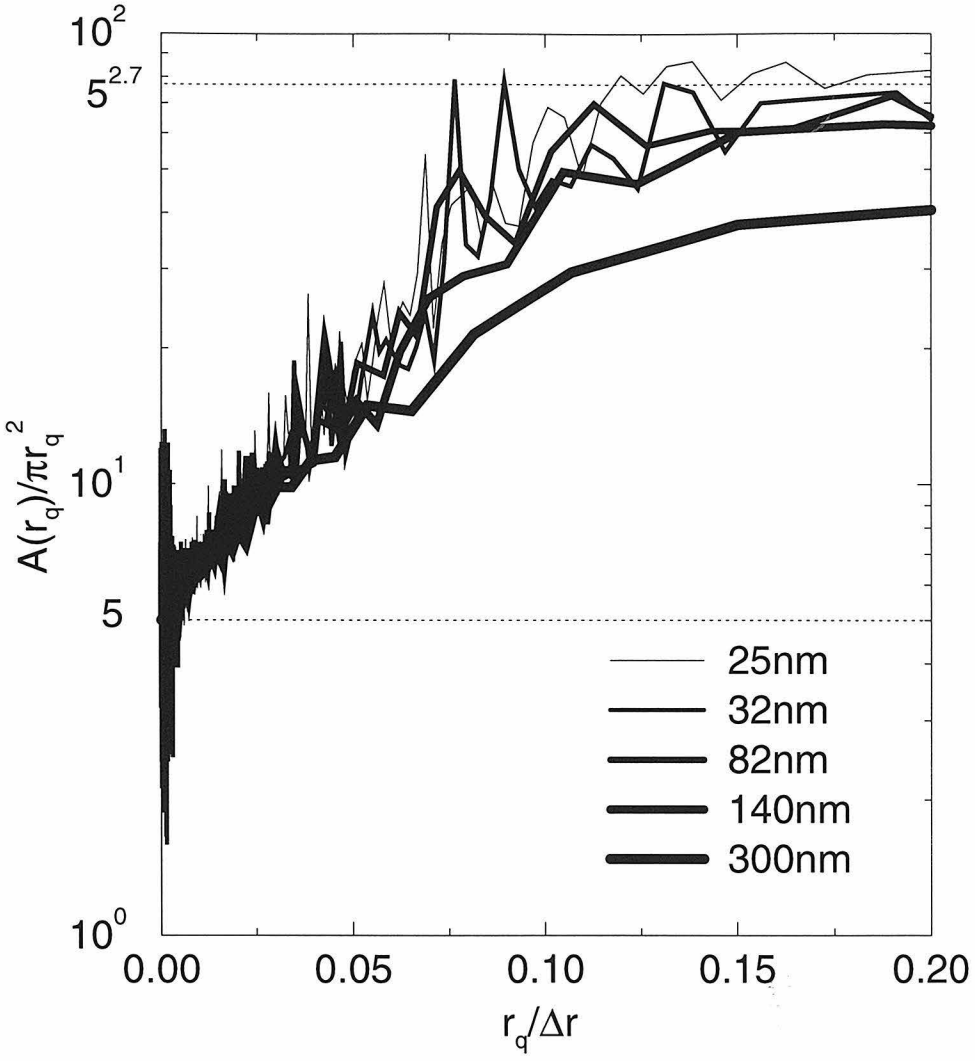

Figure 5.16: Desorption areas for 2MeV/C C_5 clusters demonstrate a universal scaling for small values of $r_q/\Delta r$.

Chapter 6 Summary

The topics presented in this dissertation demonstrate how the use of simulation compliments experimental observations. In each case presented, simulations could make visible quantities either largely or absolutely inaccessible to laboratory techniques.

In Chapter 3, the complementary use of simulations with experimental observations allowed us to test the theoretical understanding of *in situ* production of inner-shell vacancies during hard inter-nuclear collisions. Simple kinematics of binary Li-Al collisions and the experimentally observed spectrum of backscattered $Li^+ \rightarrow Al(100)$ atoms suggested that a fraction of backscattered ions had suffered a discrete inelastic loss of order the energy required to produce a Li 1s vacancy. Simulations demonstrated that the trajectories of the backscattered ions were indeed simple binary bounces off the Al atoms on the surface of the target and that the distributions of distance of closest approach for these collisions were very sharply peaked about an average which was strongly dependent on the incident energy of the Li ion. The theoretical model for production of these vacancies is based on the molecular orbital theory of binary Li-Al collisions and suggests that Fermi repulsion will eject a Li 1s electron when the collision partners pass some critical distance of closest approach [9]. Matching simulation results to experimental observations demonstrated that vacancy production during these collisions is more probabilistic than the theory implies: harder collisions are more likely to produce a vacancy but there is no critical distance of closest approach at which *in situ* vacancy production is certain. A simple explanation for this observation is that because the binary collision takes place in a sea of Fermi electrons, there is a finite probability that one of these electrons will refill the orbital as the collision relaxes.

In Chapter 4, simulations of $Ar^+ \rightarrow$ In-Ga (liquid, In on top) permitted a variety of nano-scopic measurements characterizing the formation of clusters during sputtering which would have been impossible to make in a laboratory experiment. For

instance, simulations demonstrate that while single atoms tend to be sputtered from very near the Ar^+ impact site, clusters are ejected from the edge of the damage area. Further, because simulations study impact events on an event by event basis, they could correlate the production of clusters to the total number of atoms sputtered during a single event, hence demonstrating that violent sputtering events produce a disproportionately greater number of larger clusters. Finally, by determination of the depth of origin of atoms ejected as clusters, simulation could confirm the interpretation that the experimentally observed greater gallium content in larger clusters is indeed due to a greater depth of origin of larger clusters.

In Chapter 5, experimental measurements coupled with simulation predictions were used to imply the length scale of a poorly understood process: the desorption of hydrogen ions from the surface of dirty targets. Experimentally, the yield of desorbed hydrogen ions from a surface when penetrated by an ion of charge q obeys $Y_{H^+} \propto q^{2.7}$, with a failure of the law occurring at small q whence the yield of hydrogen becomes independent of incident ion charge. Simple scaling arguments imply that the range of the desorption mechanism must scale as $q^{2.7/2}$ but cannot set the absolute length scale. In an effort to determine this absolute length scale of the process, measurements of hydrogen ion desorption from the *exit* side of targets penetrated by atomic clusters were made to correlate desorption to inter-ion correlation [35]. Simulations then provide the final piece of the determination by supplying predictions of the exit side correlations of the cluster ions. Despite uncertainty in the interaction potential between fast co-moving ions, simulations demonstrate that to describe the observed decorrelation of the hydrogen yield with target thickness, one must choose a desorption length scale of order the radii of the ions comprising the cluster. Because the exit charges of these cluster ions are in the region of the small q failure of the $Y_{H^+} \propto q^{2.7}$ desorption law, this suggests the origin of the failure: the range of the process can be no smaller than the size of the ion driving desorption; the $Y_{H^+} \propto q^{2.7}$ desorption law fails when the range of the process for a charge q is of order an atomic radii; thus, the absolute range of the desorption process is determined by setting the lower limit of $r \propto q^{2.7/2}$ to be the radius of the ion at the charge at which the

$Y_{H^+} \propto q^{2.7}$ desorption law fails.

Simulation is a powerful tool for the investigation of ion impact processes for the very reason that these systems are generally described by the interaction of relatively few 'trivial' mechanisms. (However, simulation may also help identify situations that are more complex, and hence are not so easily caricatured by simulation.) In all of the simulations presented in this dissertation, at most two fundamental mechanisms were included: effective internuclear potentials to describe the kinematically conservative interactions of the dressed nuclei, and (if necessary) inelastic losses of the nuclear kinetic energy to electronic degrees of freedom. With so few inputs, one can hope to trust predictions of simulations incorporating them and to understand their interplay with new physical mechanisms to be investigated. A requirement of any system to be simulated successfully is that a good portion of its character must remain after a liberal whack with Occam's razor; only then can the simulist hope effectively to exploit the omniscience and omnipotence that simulations provide.

Bibliography

[1] J.F. Ziegler, J.P. Biersack, and U. Littmark, *The Stopping and Range of Ions in Solids* (Pergamon, New York, 1985).

[2] I.M. Torrens, *Interatomic Potentials* (Academic Press Inc., New York, 1972).

[3] P.D. Townsend, J.C. Kelley, and N.E.W. Hartley, *Ion Implantation, Sputtering, and Their Applications*, (Academic Press Inc., New York, 1976).

[4] M. Born and J.R. Oppenheimer, Ann. Physik **84**, 457 (1927). D.R.Hartree, *The Calculation of Atomic Structure*, (Wiley, New York, 1957).

[5] M.S. Daw and M.I. Baskes, Phys. Rev. **B 29**, 6443 (1984).

[6] J. Tersoff, Phys. Rev. Lett. **61**, 2879 (1988).

[7] M.T. Robinson and I.M. Torrens, Phys. Rev. **B 9**, 5008 (1974).

[8] K. Gartner, D. Stock, *et al.*, Nucl. Inst. and Meth. **B 102**, 183 (1995).

[9] U. Fano and W. Lichten, Phys. Rev. Lett. **14**, 627 (1965).

[10] M. Barat and W. Lichten, Phys. Rev. **A 6**, 211 (1971).

[11] Q.C. Kessel and B. Fastrup, Case Studies in Atomic Physics 3, no. 3, 137 (1973).

[12] U. Wille and R. Hippler, Phys. Rep. (Rev. Sect. of Phys. Let.), **132**, No. 3 and 4, 129 (1986).

[13] K.A.H. German, C.B. Weare, and J.A. Yarmoff, Phys. Rev. Lett. **72**, 3899 (1994). K.A.H. German, C.B. Weare, and J.A. Yarmoff, Phys. Rev. **B 50**, 14452 (1994).

[14] C.B. Weare, J.A. Yarmoff, and Z. Sroubek, Nucl. Inst. and Meth., (in press).

[15] C.E. Moore, *Atomic Energy Levels*, Natl. Bur. Stand. U.S. Circ. No. 467 (U.S. GPO, Washington, DC, 1971), Vol 1.

[16] U. Bruch, G. Paul, and J. Andra, Phys. Rev. **A 12**, 1808 (1975).

[17] J.C. Slater, *Quantum Theory of Atomic Structure* (McGraw-Hill, New York, 1960).

[18] N.W. Ashcroft and N.D. Mermin, *Solid State Physics* (Harcourt Brace College Publishers, Fort Worth, 1976).

[19] M.H. Shapiro and T.A. Tombrello, Nucl.Inst.and Meth. **B 102**, 227 (1995).

[20] J. Los and J.J.C. Geerlings, Phys.Rep. **190**, 133 (1990).

[21] C.B. Weare and J.A. Yarmoff, Surf. Sci. **348**, 359 (1996).

[22] P. Sigmund, Phys. Rev. **184**, 383 (1969). M.W. Thompson, Phys. Rep. (Rev. Sec. of Phys. Let.) **69**, No. 4, 335 (1981).

[23] A. Wucher, Nucl. Inst. and Meth. **B 83** (1993) 73. Z. Ma, S.R. Coon, W.F. Callaway, M.J. Pellin, D.M. Gruen and E.I. von Nagy-Felsobuki, J. Vac. Sci. and Tech. **A 12** (4), part 2, 2425 (1994).

[24] W. Husinsky, G. Nicolussi, and G. Betz, Nucl. Inst. and Meth. **B 82**, 323 (1993). S.R. Coon, W.F. Callaway, M.J. Pellin, G.A. Curlee, and J.M. White, Nucl. Inst. and Meth. **B 82**, 329 (1993). A. Wucher, M. Wahl, and H. Oechsner, Nucl. Inst. and Meth. **B 82**, 337 (1993). Z. Ma, W.F. Calaway, M.J. Pellin, E.I. von Nagy-Felsobuki, Nucl. Inst. and Meth. **B 94**, 197 (1994).

[25] W. Eckstein, Nucl. Inst. and Meth. **B 33**, 489 (1988). U. Conrad and H.M. Urbassak, Nucl. Inst. and Meth. **B 48**, 399 (1990).

[26] G.P. Konnen, A. Tip, and A.E. deVries, Radiation Effects **21**, 269 (1974). G.P. Konnen, A. Tip, and A.E. deVries, Radiation Effects **26**, 23 (1975).

[27] W. Gerhard, Z. Phyzik **B 22**, 31 (1975).

[28] T.B. Lill, W.F. Callaway, M.J. Pellin, and D.M. Gruen, Phys. Rev. Lett. **73**, 1719 (1994).

[29] M.F. Dumke, T.A. Tombrello, R.A. Weller, R.M. Housley, E.H. Cirlin, Surf. Sci. **B 124**, 407 (1983).

[30] M.H. Shapiro, K. Bengston,Jr.,and T.A. Tombrello, Nucl. Inst. and Meth. **B 108**, 51 (1996).

[31] G. Betz and W. Husinsky, Nucl. Inst. and Meth. **B 102**, 281 (1995).

[32] T. Lill, W.F. Calaway, Z. Ma, and M.J. Pellin, Surf. Sci. **322**, 361 (1995).

[33] K.M. Hubbard, R.A. Weller, D.L. Weathers, and T.A. Tombrello, Nucl. Inst. and Meth. **B 36**, 395 (1989).

[34] A. Wucher, Nucl. Inst. and Meth. **B 83**, 79 (1993). S.R. Coon, W.F. Callaway, and M.J. Pellin, Nucl. Inst. and Meth. **B 90**, 518 (1994).

[35] Y. Le Beyec, *ELAF 91, Collision Processes of Ion, Positron, Electron and Photon Beams with Matter*, eds A.C.A. Souza, E.F. da Silveira, J.C. Nogueira, M.A.C. Nascimento and D.P. Almeida (World Scientific, Singapore 1992), p.15 ff.

[36] A. Brunelle, S. Della-Negra, J. Depauw, H. Joret, and Y. Le Beyec, Nucl. Inst. and Meth. **B 43**, 586 (1989).

[37] A. Brunelle, S. Della-Negra, J. Depauw, D. Jacquet, M. Pautrat, Y. Le Beyec, C. Schoppmann, IPNO DRE 96-25 (1996).

[38] E.F. da Silveira and M. Matos, Surf. Sci. **326**, 370 (1995). I. Bitensky, E. Parilis, S. Della-Negra and Y. Le Beyec, Nucl. Inst. and Meth. **B 72**, 380 (1992).

[39] R.C. Weast, M.J. Astle, and W.H. Beyer, eds. *CRC Handbook of Chemistry and Physics* (CRC Press, Inc., Boca Raton, Florida, 1984)

[40] Brandt, *Ion screening in solids, atomic collisions in solids*, eds S. Datz, B.R. Appleton, and C.D. Moak (Plenum, New York 1975) vol. 1, p.261 ff.